



HAL
open science

Development of antenna systems for 5G communications

Tran Quang Khai Nguyen

► **To cite this version:**

Tran Quang Khai Nguyen. Development of antenna systems for 5G communications. Electronics. Université Côte d'Azur, 2020. English. NNT : 2020COAZ4100 . tel-03218705

HAL Id: tel-03218705

<https://theses.hal.science/tel-03218705>

Submitted on 5 May 2021

HAL is a multi-disciplinary open access archive for the deposit and dissemination of scientific research documents, whether they are published or not. The documents may come from teaching and research institutions in France or abroad, or from public or private research centers.

L'archive ouverte pluridisciplinaire **HAL**, est destinée au dépôt et à la diffusion de documents scientifiques de niveau recherche, publiés ou non, émanant des établissements d'enseignement et de recherche français ou étrangers, des laboratoires publics ou privés.

THÈSE DE DOCTORAT

Développement de système antennaire pour les communications 5G

Tran Quang Khai NGUYEN

Laboratoire d'Electronique Antennes et Télécommunication (LEAT)

**Présentée en vue de l'obtention
du grade de docteur en Electronique
d'Université Côte d'Azur**

Dirigée par : Fabien FERRERO

Co-encadrée par : Leonardo LIZZI

Soutenue le : 30 Novembre 2020

Devant le jury, composé de :

Lars JONSSON, Professeur, EME, KTH
Royal Institute of Technology

Laurent CIRIO, Professeur, Université Paris-
Est Marne-la-Vallée

Anthony GHIOTTO, Maître de conférences,
IMS Research Center, Bordeaux INP

Philippe RATAJCZAK, Ingénieur, Orange

Fabien FERRERO, Professeur, Université
Côte d'Azur

Leonardo LIZZI, Maître de conférences,
Université Côte d'Azur

Développement de système antenne pour les communications 5G

Président du jury

Lars JONSSON, Professeur, EME, KTH Royal Institute of Technology

Rapporteurs

Laurent CIRIO, Professeur, Université Paris-Est Marne-la-Vallée

Anthony GHIOTTO, Maître de conférences, IMS Research Center, Bordeaux INP

Examineur

Philippe RATAJCZAK, Ingénieur, Orange

Directeur de thèse

Fabien FERRERO, Professeur, LEAT, Université Côte d'Azur

Encadrant

Leonardo LIZZI, Maître de conférences, LEAT, Université Côte d'Azur

Résumé

Développement de système antenne pour les communications 5G

Ce travail de thèse a été financé par le projet FUI Mass-Start (2017-2020). Le projet ambitionne de développer une solution open source 5G pour le MIMO Massif. L'objectif est le développement d'une plateforme Hardware et Software, sur le principe du succès d'OAI en 4G (www.openairinterface.org). Les principaux livrables matériels du projet sont les sous-systèmes radio et de traitement de bande de base compatibles 5G, leur intégration dans un démonstrateur de terminal 5G basé sur OAI et le réseau d'antennes permettant les expérimentations de bout en bout du lien MIMO Massif. L'objectif de la thèse est le développement et la mesure de systèmes antennes qui seront utilisés dans le projet.

Sur la bande 5G FR1, le travail s'est concentré sur le développement d'une méthodologie de conception antenne combinant circuit d'adaptation et optimisation géométrique. Les contraintes en bande passante sont évaluées à partir du facteur de qualité des antennes. Le prototype final démontre qu'un système non-résonnant permet de couvrir la plupart des bandes de téléphonie mobile 5G sous les 6GHz en respectant des contraintes d'intégration très forte.

Sur la bande 5G FR2, et plus précisément sur la bande n258 Européenne, différents types d'architecture d'antennes réseau ont été évalués et mesurés. La thèse s'est particulièrement concentrée sur la co-conception entre les antennes et les modules électroniques sur une technologie PCB.

Les solutions proposées ont été utilisées pour quantifier et modéliser l'effet du corps humain, et plus particulièrement de la main, sur les performances sur réseau antenne. Enfin, une solution basée sur plusieurs réseaux distribués sur un téléphone montre une meilleure robustesse aux effets de blocage du corps humain.

Mots-clés : 5G, conception d'antenne, optimisation de l'antenne, onde millimétrique, effets humains, efficacité de la couverture.

Abstract

Development of antenna systems for 5G communications

The work in this thesis has been funded by the French FUI project MASS-START (2017-2020). The project aims at the integration of 5G compatible baseband and radio subsystems into an Over-Air-Interface-based 5G terminal and gNodeB demonstrator, and the antenna array for end-to-end Multiple Input Multiple Output link experimentation. The scope of the thesis concerns the design and assessment of antenna systems that are to be used in the project.

At 5G Frequency Range 1 band, the work concentrates on the development of a methodology to design antenna with a matching circuit for mobile terminals with limited area. The bandwidth limitation is evaluated using Quality-Factor. A Particle Swarm Optimization algorithm is proposed and examined in different antenna designs for mobile terminals. The final design demonstrates a system with three non-resonating coupling elements covering most of the sub-6GHz bands of 5G.

At 5G Frequency Range 2 band, more precisely band n258 of Europe, different types of array antennas are studied. The work first checks two types of feeding for a patch antenna that can be integrated into Printed Circuit Board to have a low profile antenna and ease the fabrication procedure. The designs are later fabricated and experimentally evaluated.

With a Millimeter-Wave array at hand, we proceed a measurement campaign in which the effects of the user's finger at close proximity of the antenna are evaluated. The losses due to absorption, reflection, diffraction are quantified and compared with numerical estimations in literature. A system of multiple end-fire arrays placed at different locations in a terminal is also studied showing the compromising effectiveness if one array is severely blocked.

Keywords: 5G, antenna design, antenna optimization, millimeter wave, human effects, coverage efficiency.

Acknowledgements

I completed this dissertation during the second lockdown of France, which I found it was the best time to capture all of my work for the 3-year PhD. There are many people whom I have encountered and to whom I owed during my time in LEAT. It has been an eventful journey!

First and foremost, I wish to give my special thanks to Prof. Fabien Ferrero and Prof. Leonardo Lizzi for being my dear supervisors. I am still impressed by your knowledge and experience after those years working together. I am always eager to learn as much as possible from you both!

I would like to thank Mr. Phillippe Ratajczak, Prof. Lars Jonsson, Prof. Laurent Cirio, and Prof. Anthony Ghiotto for reading and commenting on the first version of this dissertation. I guess it would be torturous for you reading my terrible writing. Nevertheless, you helped to finish it and gave so many insightful comments which I used to improve for further completeness.

I also wish to express my sincere gratitude to Prof. Lars Jonsson and Prof. Katsuyuki Haneda in connection with this dissertation as my supervisors and collaborators even for a short period. Albeit short, my visit to Aalto in 2019 was a great experience. I have highly appreciated the warmest welcoming from Katsu's group. Likewise, the visit to KTH was unfortunately missed, still, I would like to thank a lot for the invitation from Prof. Lars Jonsson. He was also a very nice amusing officemate during my internship in 2017.

Thank you, Luca and Maria - my talented teammates. I enjoyed so much working with them and completely believe that they will achieve a lot of success in their career. Thank Laurent, Nassim, Lyes, David, Koffi, and many others in the lab. Having coffees + lunches + footballs + beers with them helps me adapt to the new culture and improve my French. They are very energetic, fun and helpful! For a certain time, I did feel lost in the works and

could not see the future of what I was doing. Thank you, Suzan, the guy who showed up as a real senior and brightened me up. I have been greatly inspired by him.

Finally, I want to dedicate my gratitude to my family and friends, including My Anh, Quoc Anh, Phi Long, Quoc Viet, Van Hieu, Vu Minh, and many others. Although they are not always close, they have been my sources of happiness, relaxation, and support. Being a foreigner is not a pleasant experience at the beginning. Without them, it must be worse. I am grateful to them for being a huge mental relief to me during this journey.

Contents

Abstract	v
Acknowledgements	vii
1 Introduction	1
1.1 Developments of 5G - the context	1
1.2 Outline of the thesis	6
2 Method of Moments for Q-factors boundaries calculation	9
2.1 MoM using RWG-basis function	11
2.2 Q-factor definition and boundaries for a given antenna geom- etry	16
2.2.1 Q-factor in circuits and in antennas	16
2.2.2 Low-bound Q-factor for a given geometry	20
2.3 Examples of antenna evaluation using Q-factor and MoM . . .	22
2.3.1 Bandwidth estimation and optimization for IoT minia- ture antenna	22
2.3.2 Directivity boundary with respect to a certain bandwidth	27
2.4 Evaluating effect of narrow clearance on mobile phone antenna	33
2.4.1 Parametric studies of a mobile terminal	33
2.4.2 2D and 3D geometries	36
2.5 Conclusion	40
3 Multi-band multi-element mobile antenna design	43

3.1	State of the arts on mobile antenna design and genetic antenna optimizations	43
3.1.1	Recent developments on mobile antenna design	43
3.1.2	Particle Swam Optimization and antenna optimization	45
3.2	PSO on mobile antenna design and optimizations	49
3.2.1	PSO methodology for hybrid antenna designs	49
3.2.2	1-element or 2-element design for single wide band?	51
3.2.3	Double bands 2-element antenna design	55
3.2.4	Triple bands 3-element antenna design	59
3.3	Comparison and conclusion	69
4	Antenna designs and measurements at mmWave	73
4.1	Design and measurement concerns	73
4.1.1	Generals	73
4.1.2	Antenna array architectures for 5G mmWave	74
4.2	Broadside antenna designs at mmWave	78
4.2.1	Design properties and choices of feeding networks	79
4.2.2	Via direct feed array design	88
4.2.3	Aperture-coupled patch array design	96
4.3	Experimental evaluations of the designs	100
4.3.1	Via direct feed design	100
4.3.2	Aperture-coupled patch design	101
4.4	An end-fire array antenna at mmWave	104
4.4.1	Array design and integration in mobile phone casing	104
4.4.2	Assessment of beamforming in mmWave	105
4.5	Conclusion	109
5	Human finger's effects on array antenna at mmWave	111
5.1	Human's effect on mmWave radiation and measurement availability	111

5.2	Radiation measurements for 5G NR and figure of merit	113
5.2.1	Far-field and near-field measurements for 5G NR	113
5.2.2	Coverage efficiency - Figure of merit	118
5.3	Human finger's effects on broadside array antenna	122
5.3.1	Antenna, case and human's finger models	122
5.3.2	Effects on matching and realized gains in simulations .	125
5.3.3	Experimental evaluation of the effects on single elements	127
5.3.4	Beamforming and coverage efficiency of the array . . .	129
5.4	Human finger's effects on end-fire array antenna	134
5.5	Conclusion	137
6	Conclusion	139
	Bibliography	145

List of Figures

1.1	Walkie-Talkie device using from WWII (Wikipedia).	2
1.2	Radar diagram of 5G disruptive capabilities [13].	2
1.3	3GPP timeline for Release 16 finalization and Release 17 [14].	4
1.4	General changes in modern mobile phone appearance.	7
2.1	Triangulation of a structure (left); MoM edge element and the dipole interpretation (right).	12
2.2	Simplistic model of a mobile phone single antenna.	14
2.3	Structure segmentation of simplistic model of a mobile phone after stitching.	15
2.4	Surface current from MoM calculation of the simplistic phone model.	16
2.5	A simple series RLC lumped circuit and its return loss.	17
2.6	Reflection coefficient after tuning using one lumped component to cancel the imaginary part.	19
2.7	Controllable (Ω_A) and uncontrollable (Ω_G) in an antenna terminal.	21
2.8	Low-bound Q-factor as function of antenna width (left) and 3 dB potential bandwidth (red) and 6dB potential bandwidth (purple) as function of antenna width (right).	23
2.9	Meandered antenna structure with matching network.	25
2.10	Reflection Coefficients and Q-factor of antenna without matching network as functions of w	25

2.11	Reflection Coefficients of antenna with matching network. . .	26
2.12	Segmentation of a 2D rectangular.	27
2.13	xOz vertical omnidirectional pattern obtained by optimized D/Q.	28
2.14	yOz vertically omnidirectional pattern obtained by optimized D/Q.	28
2.15	xOy horizontal omni-directional pattern obtained by optimized D/Q.	29
2.16	Ox directional pattern obtained by optimized D/Q.	30
2.17	Oy directional pattern obtained by optimized D/Q.	31
2.18	Board zoning: vectors indicating embedded area on the ter- minal, non-vectored means GND (the scales are not the same along Ox and Oy-directions).	32
2.19	Oy directional pattern of embedded antenna obtained by op- timizing D/Q.	32
2.20	Mesh for simplistic model of a mobile phone.	34
2.21	Parametric study of the length of GND. Full parametric scale is on the left and zoomed one is on the right.	35
2.22	Parametric study of the length of the horizontal patch. Full parametric scale is on the left and zoomed one from 27mm to 75mm is on the right.	35
2.23	Parametric study of the width of the clearance's width for two structures width 45mm and 75mm lengths patch.	36
2.24	The 7 study geometries of simplistic mobile phone.	38
2.25	The optimal surface currents on the clearance, the vertical plate and the patch.	40
3.1	Graphic illustration of function $\text{sinc}(x) * \text{sinc}(y)$ in 3D (left) and 2D (right) with global optima (A) and local optima (B). . .	48

3.2	Flow chart of the optimization procedure using PSO.	50
3.3	The iterative procedure for hybrid antenna and MN optimization.	51
3.4	Different cellular bands at subGHz.	51
3.5	Mobile terminal structure and antenna geometry.	53
3.6	The designs of manual-tuning 1-element and auto-generated 2-element antennas.	54
3.7	Matching and isolation for the 2 designs.	54
3.8	The convergences of optimization with 2 LC component MN (top left) and with 2 LC component MN (top right). A comparison of the duo obtained bands with single band efficiencies (bottom).	55
3.9	Optimizing parameters for double bands 2-element design. . .	56
3.10	Corresponding optimize matching networks for the double band antennas.	56
3.11	Impedance matching of the two antennas (with and without the MN).	57
3.12	Isolation between the two feeding ports.	57
3.13	Total Efficiency of the two antenna systems.	58
3.14	Impedance matching of the single port antenna system.	59
3.15	The convergence of total efficient in the best run of the optimization.	62
3.16	Final shape of the terminal with antennas after the best run of the optimization.	62
3.17	Corresponding optimize matching networks for the triple band antenna.	63
3.18	Efficiencies, matching of the elements and isolation between them from Optenni Lab.	63

3.19	The corresponding agents' movement and velocities in the best run of the optimization.	64
3.20	Simulation of triple-band design with matching networks and substrate.	65
3.21	2D radiation patterns of different antennas at different frequencies of their working bands.	66
3.22	3D patterns of the triple antenna system at 0.8 – 1.7 – 2.7 – 3.5GHz.	67
3.23	Surface currents on the ground plane of the terminal at 0.8 – 1.7 – 2.7 – 3.5GHz.	67
3.24	Prototype of the 3-antenna triple-band design. a) Different parts of the prototype before (left) and after (right) soldered together. b) Lumped matching networks and filters soldered. c) side view of the prototype, excitation ports are behind. d) Top view of the prototype with hand.	68
3.25	Experimental scattering parameter of the prototype.	69
3.26	Field measurements with Satimo Starlab and the resulting antenna efficiency. The dash thin line and the solid lines are the results before and after correction, respectively.	70
4.1	Full digital array architecture.	76
4.2	Full analog array architecture.	76
4.3	Fully connected hybrid array architecture (left) and partially connected hybrid array architecture (right).	77
4.4	4-layer PCB stack-up example.	79
4.5	Blind via (A,C) and buried via (B) from Eurocircuits website.	80
4.6	Reflection coefficient of single patch structure for different feeding position	81

4.7	Different excitation types for patch antenna (courtesy of Balanis' book).	83
4.8	Parameters of via feeding design.	84
4.9	Parametric studies for via feeding design.	84
4.10	Parameters of aperture coupled design.	86
4.11	Parametric studies for aperture coupled design.	86
4.12	Reflection coefficients in two designs.	87
4.13	Directivity patterns of two designs in xOz (solid lines) and yOx (dash lines) planes.	87
4.14	Simulated radiation efficiencies and realized gain at $\theta = 0^\circ, \phi = 0^\circ$ in two designs.	88
4.15	Matching and pattern of single design for via-direct feeding type.	89
4.16	H-plane array.	90
4.17	E-plane array.	90
4.18	1-to-8 Wilkinson feeding network.	91
4.19	The effectiveness of vias in PCB, from left to right: with few vias, with additional vias and with additional blind/buried vias.	91
4.20	Blind vias (pink color in the transparent view on the left) at the bottom layer to enhance TM line transmission.	93
4.21	Directivity and Gains for E-plane design with blind vias.	94
4.22	Directivity variation over frequency band, zoom out (left) and zoom in (right).	95
4.23	Top, bottom and cut views of the simulated array design with a substrate wall support.	96
4.24	Minimal differences in radiation pattern between designs with (dash line) and without (solid line) a flexible substrate.	97
4.25	Numerical scattering parameters of the array.	97

4.26	Demonstration of beam synthesizing at main direction.	98
4.27	Array factor of the an 0.7λ array with four elements.	99
4.28	Beam steering by changing input phase step to the array.	99
4.29	Via feeding prototypes before (a) and after (b) adding the stacked patch. The back of the prototypes is in (c).	100
4.30	Impedance matching of the 1×4 via feeding array prototype.	101
4.31	Top and bottom views of the prototype with connectors.	101
4.32	Measured total efficiencies and realized gain at $\theta = 0^\circ, \phi = 0^\circ$ of all array elements over frequency.	102
4.33	Realized gain patterns of all array element in xOz (top) and yOx (bottom) planes at 26 GHz.	103
4.34	Scanning beams from $\theta = -50^\circ$ to $\theta = 50^\circ$ in xOz -plane at 26 GHz.	103
4.35	3D model of the proposed antenna structure	105
4.36	S-Parameters measurements of the 8 elements	105
4.37	View of the prototype during measurements	106
4.38	Total gain measurement of the 4 antennas in xOZ plane	107
4.39	Processing of the maximal Beamforming gain for different phase resolutions	108
4.40	Processing of the minimal Beamforming gain for different phase resolutions	109
5.1	Far-field and near-field regions with respect to AUT's center.	114
5.2	Spherical coverage specifications from 3GPP for different 5G mmWave bands.	116
5.3	Waves in Near-field and Far-field, and phase error consideration in Far-field measurement in quiet zone.	116
5.4	3D spherical scanner in LEAT.	118

5.5	Grid types in pattern measurements, courtesy of Rohde & Schwarz [104].	121
5.6	Constant step size to constant density grid types conversion. .	122
5.7	Single element antenna structure. a) Separated views of different layers of the design. b) Substrate specifications and patch. c) Top view with array element placements. d) Bottom view. .	124
5.8	The simulation of array antenna with casing and finger (top) and the illustration of distances and angular positions of coverage of the finger to array elements (bottom).	124
5.9	Reflection coefficients of single-antenna elements.	125
5.10	Simulated realized gains of single-antenna elements at 26 GHz on azimuth plane.	125
5.11	Simulated coverage efficiencies for two different orientations of the patch array (to study the impact of the finger in two orthogonal polarization cases).	127
5.12	The simplified mobile phone prototype with antenna array and casing.	128
5.13	Left figure: Radiation measurement with real human's hand using spherical scanner. 1-finger (left) and 2-finger (right) configurations are represented in the small figure at the bottom. Right figure: Block-out area in measurements.	128
5.14	Realized gains of each antenna element in the array for three cases of finger intervention. In each sub-figure, θ and ϕ [°] are shown in vertical and horizontal directions, respectively. . . .	130
5.15	Measured gains of single elements in azimuth plane in different cases. Elements' order is from left to right, top to bottom. .	130
5.16	Coverage efficiencies in simulations and measurements. . . .	131
5.17	Replacing block-out area in measurement with simulation data in no-hand case.	132

5.18	Maximum gain across azimuth angles (left) and coverage efficiency (right) of array antenna in different cases.	133
5.19	Studying the effects of changing patch height (left), material (middle) and frequency (right) on coverage efficiency.	134
5.20	Measurement of finger effect on end-fire array	135
5.21	Blockage effect on end-fire array, vertical axe is ϕ and horizontal axe is θ	135
5.22	Coverage efficiency CDF of array 1, array 2 and the combined patterns from the left to the right; the top figures are without user's hand and the bottom ones are with hand.	137
6.1	OOKLA 5G roll-out map of Europe, accessed October 2 nd 2020.	143

List of Tables

2.1	Strengths and weakness of CEM methods as widely implemented for open region problems. (N.O. means Not Optimal)	10
2.2	Strengths and weakness of CEM methods as widely implemented for guided wave problems. (Good > Satisfying > N.O.)	10
2.3	Comparison among MoM, HFSS, CST.	16
2.4	Comparison of different configuration of antenna geometries 2D and 3D.	39
3.1	Components' changes (pF for capacitors and nH for inductors)	58
3.2	Comparison with state of the art designs. Dimensions are in millimeter.	70
4.1	Comparison of different configurations of via direct feeding array antenna.	93
5.1	Conformance test cases that require only 3D positioning for mmWave.	115
5.2	Conformance test cases that require 3D pattern (or scan) for mmWave.	115
5.3	UE spherical coverage for power class 3.	115

List of Abbreviations

1/2/3/4/5/6G	The 1st / 2nd / 3rd / 4th / 5th / 6th Generation of Telecommunications
3GPP	The 3rd Generation Partnership Project
5G NR	5G New Radio
ADC	Analog to Digital Converter
AUT	Antenna Under Test
CDF	Cumulative Distribution Function
CPWG	Coplanar Waveguide with Ground
DAC	Digital to Analog Converter
DUT	Device Under Test
EDGE	Enhanced Data GSM Environment
EFIE	Electric Field Integration Equation
GSM	The Global System for Mobile Communications
FDTD	Finite Difference Time Domain
FEM	Finite Element Method
FR1	Frequency Range 1
FR2	Frequency Range 2
gNB	gNodeB
GPRS	General Packet Radio Service
HPBW	Half Power Beam-Width
IoT	Internet of Things
KPI	Key Performance Indicator
LTE	Long-Term Evolution
MIMO	Multiple Input Multiple Output

mmWave	Millimeter Wave
MoM	Method of Moments
NSA	Non Stand-Alone Mode
NCE	Non-resonance Coupling Element
OAI	Open Air Interface
OTA	Over The Air
PCB	Printed Circuit Board
Q-Factor	Quality Factor
RF	Radio Frequency
RWG	Rao-Wilton-Glisson
SA	Stand-Alone Mode
SMA	Sub-Miniature version A (cable/connector)
TDD	Time Division Duplex
TM line	Transmission line
UE	User Equipment
VNA	Vector Network Analyzer

List of publication

Journal paper

- T. Q. K. Nguyen, M. S. Miah, L. Lizzi, *et al.*, “Experimental Evaluation of User’s Finger Effects on a 5G Terminal Antenna Array at 26 GHz,” *IEEE Antennas and Wireless Propagation Letters*, vol. 19, no. 6, pp. 892–896, 2020.

International conference papers

- T. Q. K. Nguyen, I. Santamaria, L. Lizzi, *et al.*, “Measurement of Finger Effects on Coverage Efficiency for User Equipment Mm-Wave Antenna,” in *2020 IEEE International Symposium on Antennas and Propagation and North American Radio Science Meeting*, IEEE, Montreal, Canada, Jul. 2020, pp. 1–2. [Online]. Available: <https://hal.archives-ouvertes.fr/hal-02511917>.
- K. Nguyen, F. Ferrero, and L. Lizzi, “Feeding Techniques for Multilayer PCB Mmwave Array Antenna for UE,” in *2020 International Workshop on Antenna Technology (iWAT)*, 2020, pp. 1–4.
- I. Santamaria, T. Q. K. Nguyen, L. Lizzi, *et al.*, “2-Port Antenna with Matching Network for Dual-band IoT Terminal,” in *IEEE International Symposium on Antennas and Propagation and USNC-URSI Radio Science Meeting - AP-S/URSI 2019*, IEEE, Ed., Atlanta, Georgia, Jul. 2019. [Online]. Available: <https://hal.archives-ouvertes.fr/hal-02085949>.

- L. Santamaria, T. Q. Khai Nguyen, F. Ferrero, *et al.*, “Flexible reconfigurable antenna robust to folding in wearable applications,” in *2019 IEEE International Symposium on Antennas and Propagation and USNC-URSI Radio Science Meeting*, 2019, pp. 1–2.
- T. Q. K. Nguyen, F. Ferrero, and L. Lizzi, “PSO-based Combined Antenna and Matching Network Optimization for Mobile Terminals,” in *EuCAP 2019, Krakow, Poland, Mar. 2019*. [Online]. Available: <https://hal.archives-ouvertes.fr/hal-01963416>.
- F. Ferrero, P. Ratajkzack, and T. Q. K. Nguyen, “Assessment of beamforming capabilities of a 4-element array in a smartphone at 26 GHz,” in *12th European Conference on Antennas and Propagation (EuCAP 2018)*, 2018, pp. 1–3.
- T. Q. Khai Nguyen, L. Lizzi, and F. Ferrero, “Dual-Matching for Single Resonance Miniaturized Antenna for IoT applications,” in *2018 IEEE International Symposium on Antennas and Propagation USNC/URSI National Radio Science Meeting*, 2018, pp. 793–794.
- L. H. Trinh, V. X. Bui, F. Ferrero, *et al.*, “Signal propagation of LoRa technology using for smart building applications,” in *2017 IEEE Conference on Antenna Measurements Applications (CAMA)*, 2017, pp. 381–384.

National conference paper

- F. Ferrero, T. Q. K. Nguyen, and L. Lizzi, “Co-Optimisation antenne et circuit d’adaptation pour terminaux mobiles de nouvelle génération,” in *JNM 2019 - 21èmes journées Nationales Micro-Ondes, Caen, France, May 2019*, pp. 1,4. [Online]. Available: <https://hal.archives-ouvertes.fr/hal-02070845>.

Chapter 1

Introduction

1.1 Developments of 5G - the context

The history of telecommunication is composed of many steps that have been enabling an exponential increase of communication devices in the last decade. The early stages of electro-magnetism theory can be pointed its origin from the experiments of Faraday in the early XIX century, “A Treatise on Electricity and Magnetism” by Maxwell in 1873, then the first experiment by Hertz in 1885 confirming the existence of electromagnetic field and its behaviors [11]. The first communication across the Atlantic was conducted by the experiment genius Marconi in late 1901. The technology served well during World War II, Walkie-Talkie, for example, although still bulky, was one of the first portable telecommunication devices. In my opinion, the later developments are rather commercial driven when people started calling *nG*, yet it continues drawing big attention from academic research worldwide, nevertheless.

When the First Generation of the cellular network – 1G came in the 1980s, its whole purpose was for voice calling only. Then came 2G with technologies that enabled data transferring on voice calls but at limitedly 10kbps. There were also some later upgrades of 2G including GSM, GPRS (2.5G), and EDGE (2.75G) with higher data rates. Not until 3G that people could see a big advancement in terms of data rate up to 500kbps thanks to the fulfillment of IMT-2000 specifications. Only then there were services that had never been

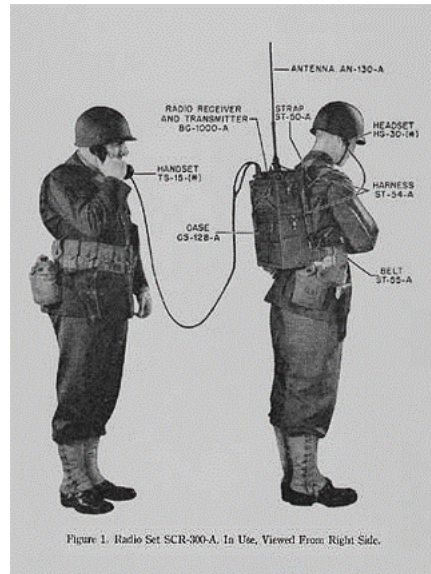


FIGURE 1.1: Walkie-Talkie device using from WWII (Wikipedia).

seen before like video calls, mobile TV. 4G Long Term Evolution (LTE) made a big leap forward from 3G by integrating IP based network system. Thanks to the superior performances, 4G is gradually replacing former cellular systems. At the end of 2019, the French government announced a 4G coverage of 99% in their territory, showing their significant commitment to providing cellular services to inhabitants [12].

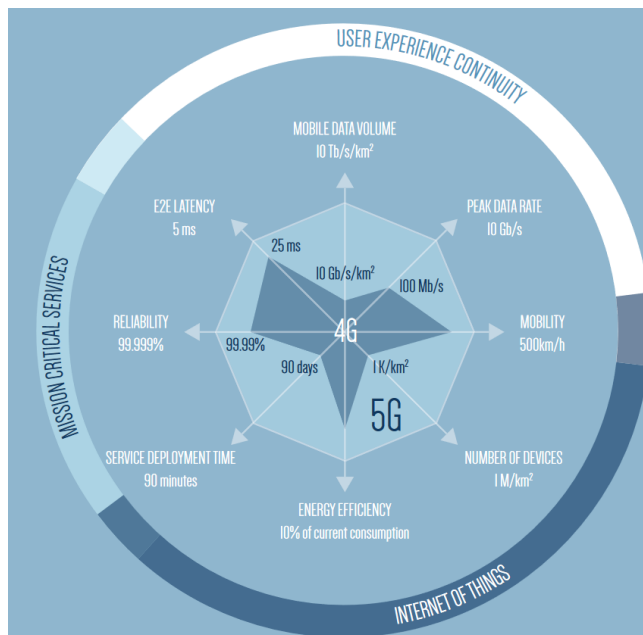


FIGURE 1.2: Radar diagram of 5G disruptive capabilities [13].

5G improves and extends the current 4G to a certain level. Figure 1.2 illustrates the expected improvements from 5G in comparison with 4G. With this, 5G will provide a seamless user experience by ensuring a peak data rate of around 10 Gbps and mobility up to 500km/h. Massive connections, especially for future IoT systems, will be closer to reality thanks to the promise of up to 1 trillion devices connection per kilometer. In addition, 5G provides mission-critical services with a data rate and reliability of 99.999% [13]. It's a big update to the current state of the communication system. Although 5G New Radio (5G NR) is a new ground-up air interface developed for 5G, there is part of the system integrated upon the available 4G infrastructure, i.e. Non-Stand Alone (NSA) mode. In addition, there is also a Stand-Alone mode (SA), where the 5G system is configured differently. NSA was deployed from the very early of 2018 as a result of the supports from 4G system infrastructure. SA mode comes later at the beginning of 2020. China is expected to go first in implementing SA thanks to its hardware development capability.

The developments of 5G have resulted from the activities of the 3rd Generation Partnership Project (3GPP) group. 3GPP's member delegates include Nokia, Huawei, Ericsson, and other companies in telecommunications who want to make a profit from standardization and going ahead. The year 2014 marks a milestone for 5G as 3GPP started the exploration phase for 5G. It then started standardizing from Release 15. Precisely, this Release defines the good 5G KPIs, including data rate, spectral efficiency, and latency, etc. It focuses on both NSA and SA architectures. NSA was finalized early at the end of 2017 while SA was later in the middle of 2018.

It provides new services to the table for users and stakeholders. Especially, Release 16 (phase 2) and Release 17 from 3GPP are rather application-wise, supporting different industry segments [14]. There are multiple features covered by those documents, including Ultra-Reliable Low-Latency Communications (URLLC), Time-Sensitive Communication (TSC), NR-Light

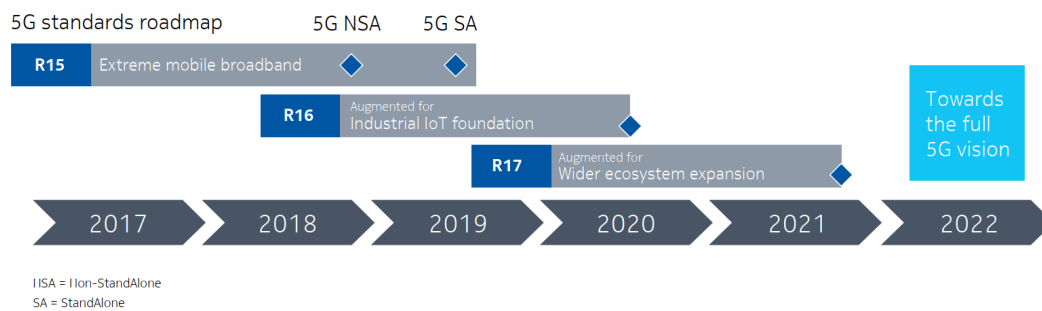


FIGURE 1.3: 3GPP timeline for Release 16 finalization and Release 17 [14].

for Industrial IoT. It provides extra features for other verticals as well, like V2X and critical communications/public safety, multicast communication, non-terrestrial networks, and railway communications.

The above-mentioned super performances are the promises of 5G. To realize these, the key features of 5G are:

Millimeter wave: signals are to be transmitted at Millimeter Wave (mmWave - Frequency Range 2), which is in range of millimeters in terms of wavelength. It should be noted that most countries in Europe plan to use band n258, 24.25 – 27.5 GHz of Frequency Range 2 (FR2). Therefore, the mmWave studies in this thesis apply this FR2 band. Some measurements, though, have been done at 28 GHz for band n257, 24.25 – 27.5 GHz for the collaborations with Aalto University.

Small cells: to overcome the path loss at mmWave, the cells are to be built smaller and denser, especially in urban zones. As early as 2012, Prof. Rappaport *et al.* have studied the characteristics of mmWave at 28 GHz and 38 GHz in the most urban environments of New York, Austin, and Texas. They have shown that with a distance within 200 m, mmWave can ensure a good connection [15].

Massive MIMO & Beamforming: also, to address the path loss from high frequency and improve throughput, more antennas, on the order of 64/128 elements or more, will be packed inside any 5G Base Station (BST/gNb).

Consequently, beamforming comes as the direct result of Massive MIMO deployment, hence the use of more antennas allows redirecting radiation beams.

Full duplex: the communication technology that allows both uplink and downlink directions to work simultaneously. The system utilizes the time-division duplex (TDD) operation and provides the uplink-downlink channel reciprocity.

Each feature comes with its own pros and cons. In general, the leading key here is the use of mmWave in cellular communications. The presence of mmWave in telecommunications is however not unprecedented. For example, radar systems have been used for a long time, military and weather forecast applications have also their own mmWave architectures. Even in the cellular system, the use of mmWave for backhaul communication is also available. However, 5G mmWave will be used for front-end communications. It has quite different and more complicated properties compare to other systems. For example, the path loss through air propagation and thermal losses in RF front end circuits are more severe. The reflective property of radiations will also be more significant in comparison to systems at lower frequencies. In addition, wave penetration is weaker, which can be useful for outdoor-to-indoor isolation. There are other challenges related to the adjacent frequency bands, especially the band 24.5 GHz for the weather forecast. Also, the absorption caused by oxygen is severe at around 60 GHz.

Concerning the developments of Massive MIMO, an interesting thought was shared in [16] about its realization. Reasonably, the author argues that Massive MIMO is already a reality and that the basics are well understood and noncontroversial. Fully digital Massive MIMO transceivers will be the mainstream in the market in a few years at both sub-6Ghz and mmWave. For the sack of 10 years of circle continuity, there are different research groups

who have recently started their works on the researches for the Sixth Generation (6G) of Telecommunications. Broadband properties will surely be enhanced by some means. But at first, let us try to address those existing issues in the 5G system.

1.2 Outline of the thesis

This work is in the scope of French 5G project MASS-START, funded by Région PACA, BPI, and other institutions. Engaged in the project are also Eurecom, TCL, SDRF, Orange, and Syrtem. We aim to develop an open-source 5G solution for the Massive MIMO, including the development of a hardware and software platform, based on the principle of OAI's success with 4G (www.open-airinterface.org).

The main hardware deliverables for the project are the integration of 5G compatible baseband and radio subsystems into an OAI-based 5G terminal and gNodeB demonstrator, and the antenna array for end-to-end MIMO link experimentation. The main software deliverables of the project are:

- Digital Massive MIMO Signal Processing algorithms for 5G, implemented on the chosen hardware target and
- A 5G NR protocol stack for terminals (UE) and base station (eNodeB) to perform experiments in a realistic environment in real time.

This thesis proposes solutions for two problems from the antenna perspective for a 5G system. The first one is the design process for a full-screen mobile phone. An effective methodology using non-resonance coupling elements and matching networks. Nowadays, antenna design for a mobile terminal is a really challenging topic. Compared with old generations' mobile phone, like in 2G or 3G, some new constraints came up. Typically, mobile phones get bigger and bigger over each new generation. However, space



FIGURE 1.4: General changes in modern mobile phone appearance.

for an antenna is not increasing proportionally. It is due to the presence of numerous circuitry for different features and different communication standards. Especially, the screen ratio gradually grows to nearly cover the full surface. The screen can even alienly go beyond the top face of the terminal, such as the futuristic form of Mi Mix Alpha from Xiaomi in Figure 1.4 (last). Moreover, the introduction of mmWave to the next generations of mobile terminals will further limit the number of locations and volumes dedicated to antennas. Finally, antenna designers and engineers have to spend more time and effort to produce a high-performance design.

Chapter 2 analyzes the limitation on the bandwidth when the clearance is reduced by adopting MoM calculations of the stored energy. Chapter 3 then proposes a methodology to design antenna with non-resonance coupling elements and matching circuits. To realize the methodology, we integrate a hybrid Particle Swarm Optimization with EM simulator and circuit optimizer.

At mmWave, the design of a more-integrated antenna draws particular attention because of the loss at a much higher order. Printed Circuit Board (PCB) is one of the advanced technologies that allows antennas to be integrated high-frequency circuits. We study two broadside designs in Chapter 4 in terms of scattering, radiation losses, etc. when designed using an industrial low-cost PCB stack-up.

The effects of the human body on mmWave mobile antennas are also of

importance at mmWave. In literature, there are detailed analyses of blockage effect when humans holding the terminal though the blockage is from the whole body [17], [18]. The finger (when users hold the phone) is exceptionally in the near-field of the mobile antenna, thus it affects the radiation differently in comparison with most other body parts. The numerical characterization of the loss from the fingers is demonstrated in [19]. We take advantage of the available mmWave antennas and the NSI setup in LEAT to quantify the effects experimentally. This will be shown in Chapter 5.

This is a thesis on antenna developments for 5G. The works will be focusing on the choices of antenna architectures, designs, techniques to improve performances, and analysis of numerical and experimental results. Normally, antennas can be defined as the first or last component of any wireless communication system. It is the transition between the air medium and the conductive/substrate one. In other words, it transforms 377Ω of air impedance to $50/75 \Omega$ impedance, or vice versa. Though every wireless system necessitates at least one antenna, the role of the antenna seems to be downplayed at many current systems because the specifications don't require much performance and the antenna design process is normally simple. 5G is providing a promising playground for antenna designers and engineers.

Chapter 2

Method of Moments for Q-factors boundaries calculation

This chapter revisits some of the old and new concepts on antenna modeling using the Method of Moments (MoM) and antenna boundary evaluations using Quality-factor (Q-factor). Not focusing on 5G application, this chapter revises some of the most fundamental aspects of antenna design, including some limitations and thus providing the reasoning for the next Chapter that relates to methodologies and real applications of antennas on 5G mobile phones.

In the last decades, EM numerical modeling has become an important part of the antenna design process. To develop a high-performance antenna, any designer should have a deep understanding of the numerical method used to solve the EM problem. It is (amusingly) analogous to a warrior understanding how to use well his/her weapon. Nevertheless, commercial simulation tools nowadays, like ANSYS HFSS, CST, FEKO, etc., are very well packaged and user-friendly. They simplify significantly the design process. For a simple case, designers need only to define the antenna system by choosing antenna configuration, size of antenna, feeding method, etc., that are expected to achieve minimum specification level on various criteria, e.i. bandwidth, directivity. The designer then builds the design using a 3D CAD tool.

User-friendly software can then proceed automatically on the next steps, including boundaries, meshing, calculating, plotting, etc.

However, each numerical method has its own advantages and disadvantages, thus strong know-how is always useful if the designer aims for optimal antennas and a rapid process. The two Tables 2.1 and 2.2 illustrate the strengths and weaknesses of the three most well-known full-wave computational electromagnetics (CEM) methods: Method of Moments (MoM, as in FEKO), Finite Element Method (FEM, as in HFSS), and Finite Difference Time Domain (FDTD as in CST). The first table is for open region problems while the latter is for guided-wave problems. The performances are reported in [20], these might be subject to changes, and performance differences might be reduced as CEM methods evolve and computer strength is improved over times.

TABLE 2.1: Strengths and weakness of CEM methods as widely implemented for open region problems. (N.O. means Not Optimal)

CEM	Equation type	Domain	Rad. condition	PEC only	Homo. penetrable	Inhomo. penetrable
MoM	Integral	Frequency	Yes	Good	Good	N.O.
FEM	Differential	Frequency	No	N.O.	Good	Good
FDTD	Differential	Time	No	N.O.	Good	Good

TABLE 2.2: Strengths and weakness of CEM methods as widely implemented for guided wave problems. (Good > Satisfying > N.O.)

CEM	Equation type	Domain	Wideband	PEC only	Homo. penetrable	Inhomo. penetrable
MoM	Integral	Frequency	Satisfying	Good	Good	N.O.
FEM	Differential	Frequency	Satisfying	Good	Good	Good
FDTD	Differential	Time	Good	Good	Good	Good

It is noted that MoM uses integral equations, while others use differential types. It is more efficient for models having mainly conductive materials and

is less efficient for models with inhomogeneous dielectric materials. FDTD, e.i. used in CST or Empire, is a time-domain method well-known for wide-band simulations in waveguiding problems. Frequency domain methods can also handle wide-band simulations, though not optimally.

Most of the simulations in this thesis are done using the Finite Element Method from HFSS which is a frequency-domain solver. Ansys HFSS is very well finalized with numerous useful features. The study of the antenna Q-factor in this section is nevertheless done using an MoM simulator thanks to its flexibility and easiness to be modified to calculate stored energies. The MoM codes are based on Makarov's Matlab program [21]. His codes, though optimized for calculation time, has a first-order precision of MoM. The development of the Q-factor code is based on the instructions from the European School of Antenna course ARIA in Nice, 2019 [22]. To ensure accountability, the developed codes in this work are sometimes compared with a better-implemented MoM solver from KTH University.

2.1 MoM using RWG-basis function

In MoM, the geometry of scattering or radiation object is replaced by equivalent surface currents. Volumetric currents can be used for 3D structures, but it is computational expensive and has been rarely implemented. In meshing process, the simulated structure is segmented into 2D wires or 3D patches. Each segment has influences on every other segments. All the influences are quantified in a square matrix equation.

Makarov's code implements triangular segmentation and Rao - Wilton-Glisson's (RWG) basis function [21]. The structure is discretized into small triangular units, as shown in Figure 2.1. Each pair of neighbor triangles T^+ and T^- have a common edge of length l_n . The basis function ψ_n are defined as follow.

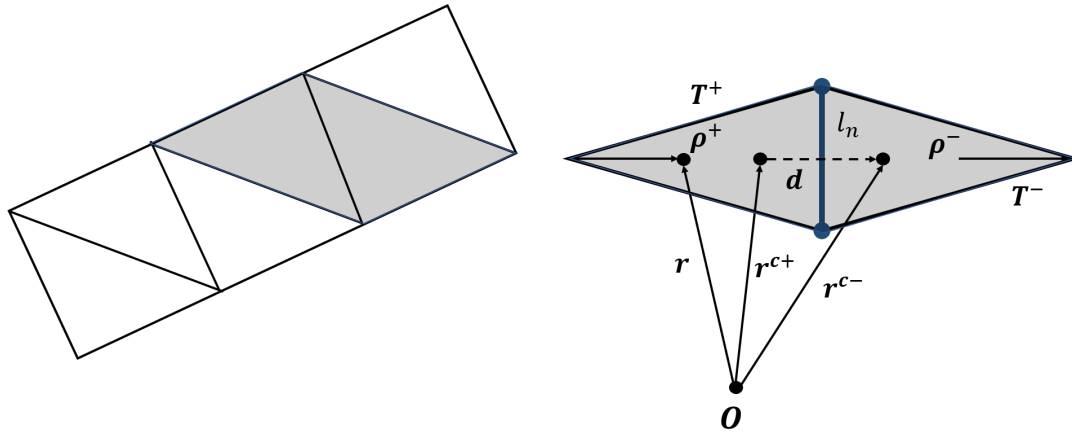


FIGURE 2.1: Triangulation of a structure (left); MoM edge element and the dipole interpretation (right).

$$\psi_n(\mathbf{r}) = \begin{cases} \frac{l_n}{2A_n^+} & \text{if } \mathbf{r} \in T_n^+ \\ \frac{l_n}{2A_n^-} & \text{if } \mathbf{r} \in T_n^- \\ 0 & \text{otherwise} \end{cases} \quad (2.1)$$

where $2A_n^+$ and $2A_n^-$ are the area of the corresponding triangles.

The current density of the structure's surface is calculated as

$$\mathbf{J} \approx \sum_{n=1}^N I_n \psi_n(\mathbf{r}) \quad (2.2)$$

By applying RWG as test and basis to Electric Field Integration Equation (EFIE) [23], [24]. We obtain the MoM (square matrix) equation

$$\mathbf{V} = \mathbf{Z} \cdot \mathbf{I} \quad (2.3)$$

where (\cdot) is dot product, $\mathbf{I} = \{I_n\}$ and $\mathbf{V} = \{V_n\}$ are $N \times 1$ vectors coefficients of \mathbf{J} and tangential electric field E_{tan} . Elemental current I_n corresponds to RWG element n of the structure. Green function used is the free-space Green function.

The elemental currents are given by solving the MoM equation with respect to boundaries. From the surface currents, the scattering parameters and

the radiation of the structure can be derived. The $N \times N$ impedance matrix of the EFIE has components Z_{mn} , which describes the contribution of dipole n to the electric current of dipole m as follows.

$$Z_{mn} = l_m \left[j\omega \left(A_{mn}^+ \cdot \frac{\rho_m^{c+}}{2} + A_{mn}^- \cdot \frac{\rho_m^{c-}}{2} \right) + \Phi_{mn}^- - \Phi_{mn}^+ \right] \quad (2.4)$$

where l_m is the length of the edge element m . $\rho_m^{c\pm}$ are vector between the vertex point and the centroid point ($\mathbf{r}_m^{c\pm}$) of the two triangles connecting to edge m , illustrated in Figure 2.1. The magnetic potential vector A and the scalar potential Φ are in Lorentz gauge that satisfy $(\nabla^2 + k^2) \phi(\mathbf{r}) = -\rho(\mathbf{r})/\epsilon_0$ and $(\nabla^2 + k^2) \mathbf{A}(\mathbf{r}) = -\epsilon_0 \mathbf{J}(\mathbf{r})$.

If an incident wave E^{inc} comes to the structure, the voltage excitation is derived as

$$V_m = l_m \left(E_m^+ \cdot \frac{\rho_m^{c+}}{2} + E_m^- \cdot \frac{\rho_m^{c-}}{2} \right) \quad (2.5)$$

where $E_m^\pm = E^{inc}(\mathbf{r}_m^{c\pm})$. The transmission radiation with ports can be done reversely by putting an oscillating voltage at the excitation edges to introduce the currents to the structure and hence, the magnetic and electric fields are as follow.

$$\mathbf{H}(\mathbf{r}) = \frac{jk}{4\pi} (\mathbf{m} \times \mathbf{r}) C e^{-jkr}; = \frac{1}{r^2} \left[1 + \frac{1}{jkr} \right] \quad (2.6)$$

$$\mathbf{E}(\mathbf{r}) = \frac{\eta}{4\pi} \left(\mathbf{M} - \mathbf{m} \left[\frac{jk}{r} + C \right] + 2\mathbf{M}C \right) e^{-jkr}; \mathbf{M} = \frac{(\mathbf{r} \cdot \mathbf{m}) \mathbf{r}}{r^2} \quad (2.7)$$

where

$$\mathbf{m} = \int_{T_m^+ + T_m^-} I_m \psi_m(\mathbf{r}) dS = l_m I_m (\mathbf{r}_m^{c-} - \mathbf{r}_m^{c+}) \quad (2.8)$$

is the dipole moment of edge element m , $\eta = \sqrt{\mu/\epsilon}$ is the free space impedance and $r = |\mathbf{r}|$.

The input impedance at the excitation of an antenna, on the other hand, is simply

$$Z_A = \frac{V}{I_{n'}} = \frac{V_{n'}}{I_{n'}^2} \quad (2.9)$$

where n' denotes index of excitation edges.

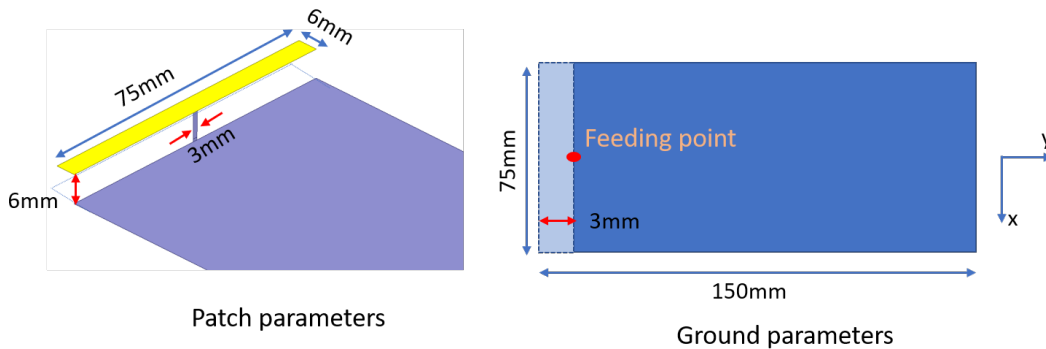


FIGURE 2.2: Simplistic model of a mobile phone single antenna.

A comparison with other simulation tools and higher accurate MoM code from Prof. Lars Jonsson has been done. Visually in Figure 2.2, a simplified mobile terminal is comprised of a $147 \times 75 \text{ mm}^2$ ground plane (representing the screen), a $6 \times 75 \text{ mm}^2$ horizontal patch, and a $3 \times 6 \text{ mm}^2$ vertical line. An open area at the top of the ground ($-Oy$ -direction) represents the clearance that most modern mobile phones still have to enhance the antenna radiation. There is a general trend of reduction of this clearance on phones due to the enlargement of screen ratio. This poses an interesting scientific problem of how much loss one should expect for the integrated antenna system for such a small ground-free area. In addition, it is also an engineering problem of how so design antenna can still radiate well. This will be evaluated later in this Chapter and is addressed in the next Chapter.

Initially, the meshing process is done separately for each part and then they are stitched together. Meshing code is provided by KTH University based on Delaunay triangulation.

<i>Ground (pgnd, tgnd)</i>	<i>Patch (ppatch, tpatch)</i>	<i>Ver. strip (pline, tline)</i>
• 1300 points	• 78 points	• 6 points
• 2450 triangles	• 100 triangles	• 4 triangles

Stitching is the process that merges two separate meshes. The overlapping points (endpoints of green edges), for example between the ground and the vertical line (Figure 2.3-Top view) or between the vertical line and the patch (Figure 2.3-Bottom view), are detected and the order of the edge list is updated coherently. After stitching all, the whole terminal (p,t) has

- 1384 points
- 2554 triangles
- 3729 edges

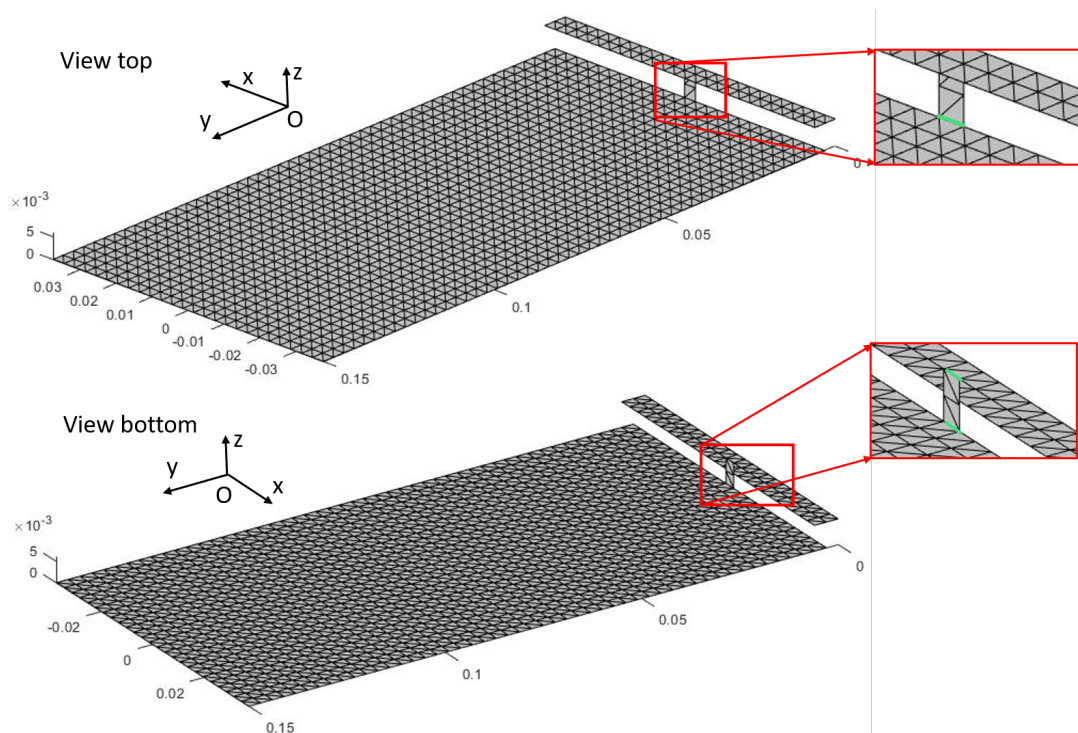


FIGURE 2.3: Structure segmentation of simplistic model of a mobile phone after stitching.

From Table 2.3, there are good agreements among the simulators over the frequencies. The MoM simulation gives real (R) and imagine (X) values that are within 8% variation of values given by CST or HFSS, knowing the commercial tools should be more accurate. The impedance at 900MHz is compared with MoM code from the KTH University too (MoM2). Their code

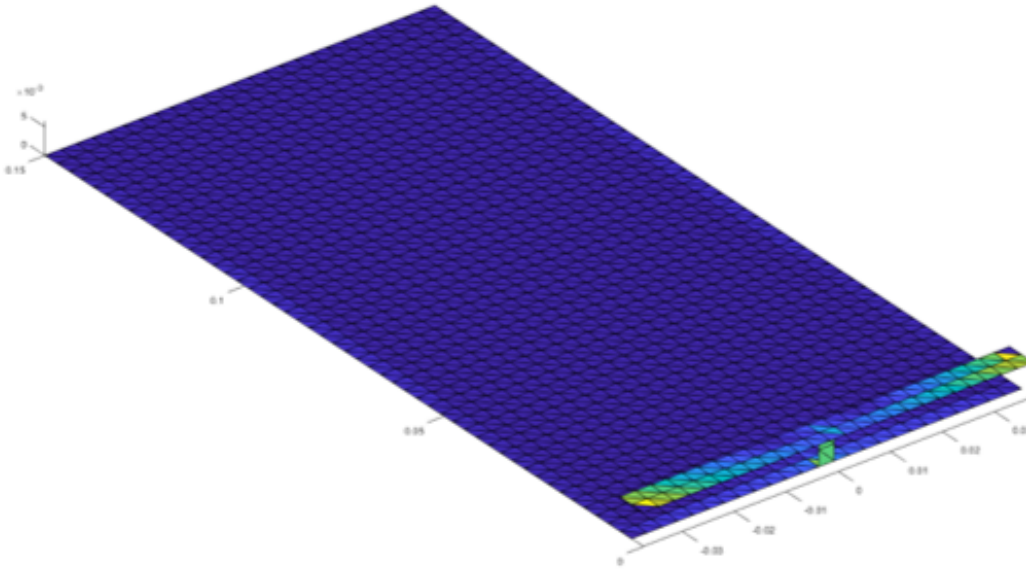


FIGURE 2.4: Surface current from MoM calculation of the simplistic phone model.

TABLE 2.3: Comparison among MoM, HFSS, CST.

	890 MHz		900 MHz		910 MHz	
	R	X	R	X	R	X
HFSS	9.83	-61.09	9.46	-60.01	9.09	-58.91
CST	9.53	-61.11	9.16	-59.89	8.79	-58.65
MoM	10.22	-64.58	9.83	-63.31	9.44	-62.01
MoM2			9.13	-63.44		

implements a higher degree of MoM. The imaginary values are close while the real values are 8% off. It should be highlighted the importance of refining the mesh whenever the computer's memory allows.

2.2 Q-factor definition and boundaries for a given antenna geometry

2.2.1 Q-factor in circuits and in antennas

By definition, the Q-factor of a circuit indicates the losses factor in that circuit. The higher the Q-factor, the lower the loss, thus narrower bandwidth, and vice versa. In a resonant lumped component circuit like in Figure 2.5 on the

left, the impedance is calculated as

$$Z_{in} = Z_C + Z_L + R = \frac{1}{j\omega C} + j\omega L + R = R + j\left(\omega L - \frac{1}{\omega C}\right) = R + jX \quad (2.10)$$

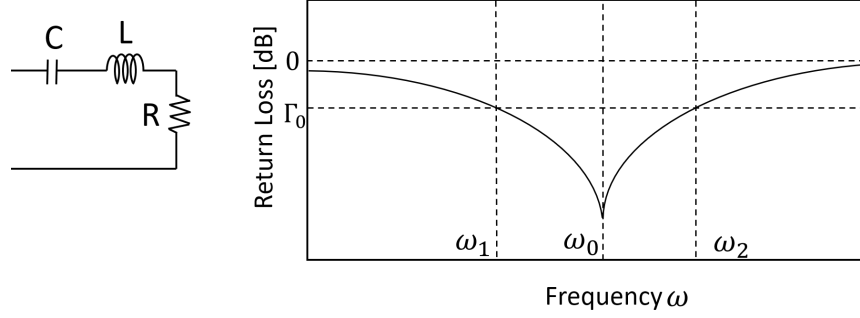


FIGURE 2.5: A simple series RLC lumped circuit and its return loss.

Resonance is defined where (in frequency) the imaginary of the impedance equals zero, thus

$$\omega_0 L - \frac{1}{\omega_0 C} = 0 \Leftrightarrow \omega_0 = \frac{1}{\sqrt{LC}} \quad (2.11)$$

Figure 2.5 on the right shows a common-seen return loss in dB as a function of the impedance with a resonance at ω_0 . The bandwidth is corresponding to the reflection coefficient threshold Γ_0 is also illustrated. This bandwidth is reversely proportional to the Q-factor. The approximate relation between bandwidth and Q-factor is given below.

$$B = \frac{\omega_2 - \omega_1}{\omega_0} \approx \frac{2}{Q} \frac{\Gamma_0}{\sqrt{1 - \Gamma_0^2}} \quad (2.12)$$

A half-power bandwidth, or 3 dB loss, corresponds to $\Gamma_0 = 1/\sqrt{2}$. This simplifies the expression into $B = 2/Q$. Equivalently, the frequency f in Hz can replace the angular frequency ω . An antenna has its own reflection coefficient that varies with its shape. An equivalent lumped circuit can be derived from the reflection coefficient, for instance, using Brune's synthesis [25]. The

impedance of antenna based on Galerkin method [26] can be presented as

$$Z_{in} = \frac{2P_{in} + 4j\omega(W_m - W_e)}{|I_{in}|^2} = R + j(X_m - X_e) \quad (2.13)$$

with magnetic and electric stored energy W_m , W_e [27], [28], formulated as follow.

$$W_m = \frac{1}{8} \mathbf{I}^H \left(\frac{\partial X}{\partial \omega} + \frac{X}{\omega} \right) \mathbf{I} = \frac{1}{4\omega} \mathbf{I}^H X_m \mathbf{I} \quad (2.14)$$

$$W_e = \frac{1}{8} \mathbf{I}^H \left(\frac{\partial X}{\partial \omega} - \frac{X}{\omega} \right) \mathbf{I} = \frac{1}{4\omega} \mathbf{I}^H X_e \mathbf{I} \quad (2.15)$$

where \mathbf{I} is the coefficients vector from MoM as aforementioned and $X = X_m - X_e$.

Therefore, analogous to the lump-components circuits, Q-factor in antenna radiation is also reversely proportional to the bandwidth. It can be determined as the ratio of the time-average stored energy and the dissipated energy [29]. The Q-factor given a surface current \mathbf{I} is given by

$$Q_I = \frac{\text{Stored Energy}}{\text{Radiated Energy}} = \frac{2\omega \max\{W_e, W_m\}}{P_{rad}} = \max\{Q_e, Q_m\} \quad (2.16)$$

where

$$Q_{e/m} = \frac{2\omega W_{e/m}}{P_{rad}}$$

An additional method for calculating the Q-factor is also well-known, proposed by Yaghjian and Best [30]. The Q-factor can be estimated by differentiating the input impedance as follow.

$$Q_z \approx \frac{\omega |Z'|}{2R} = \frac{\sqrt{(\omega R')^2 + (\omega X' + |X|)^2}}{2R} \quad (2.17)$$

The estimation is proved accurate for many antennas. However, it is shown

that the method should be used only for narrow single resonance antenna with $Q > 10$ due to the first order of accuracy. Multiple of resonances will likely underestimate the Q-factor as discussed in [31] and can be illustrated below. In the same paper, the authors suggest another method of estimation Q_B from the transformed Z_B by zeroing the imaginary part using ideal lossless LC components. hence $Z_B = Z + jX_B$ with $X_B = -im(Z)$. The later obtained bandwidth is to derive the Q-factor from equation 2.12.

Let's take the antenna in Figure 2.2 for example, the calculation of Q_z is done using Matlab resulting in **8.54** @900 Mhz. On the other hand, the Q_b is calculated based on the antenna's impedance as follows. At 900 MHz, $X_B = -im(Z) = 60.01$ so we need to match it with an inductor value $L = X_B / \omega = 10.62\text{nH}$. We obtained the reflection coefficient as in Figure 2.6.

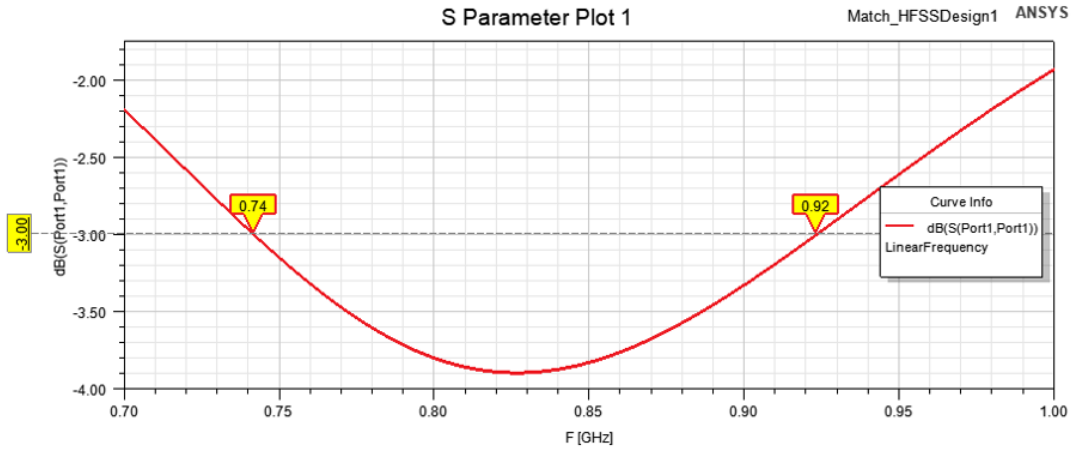


FIGURE 2.6: Reflection coefficient after tuning using one lumped component to cancel the imaginary part.

At -3 dB matching, the S_{11} covers from 740 MHz to 920 MHz. We can see that 900 MHz is slightly off the center. Nevertheless, $Q_B = \frac{2}{B} = 9.3$. In addition to these estimations of Q-factor, a calculation of the stored energy based on MoM gives a $Q_I \approx 11$.

The obtained Q-factors from different calculations are close to each other. However, the difference among them highlights the reported problem for many antennas that have Q-factor below 10. As stated above, the estimations

are less accurate and more likely to underestimate the real Q-factor. The work in [32] studies extensively this problem.

2.2.2 Low-bound Q-factor for a given geometry

For electrically small antennas, it is well-known that the bandwidth is limited. The question of how limited is especially interesting for antenna designers. As illustrated above, the Q-factor is reversely proportional to the potential bandwidth of the associated antenna. Therefore a lower-bound in Q-factor corresponds to the upper limit of any antenna.

Chu [33] introduced his limitation on the Q-factor of a spherical antenna with radius a by assuming $ka \ll 1$, where k is the wavenumber. He explicitly calculates it using the mode expansion and subtracting the power flow, giving

$$Q_{Chu} = \frac{1}{(ka)^3} + \frac{1}{ka} \quad (2.18)$$

However, spherical antennas tend to overestimate most real-life applications. Thal [34] generalized the problem with an electric current sheet, obtaining

$$Q_{Thal} = \frac{3}{2(ka)^3} \quad (2.19)$$

In [35], the author cleverly argued that there exists a low-bound Q-factor Q_{lb} and it has to be bounded as follow

$$\max\{Q_m, Q_e\} \geq Q_{lb} \geq (tQ_e + (1-t)Q_m) \quad (2.20)$$

They showed that because the far-left and far-right of the equation can have equality. Therefore, the zero-duality gap leads to

$$Q_{lb} = \max_t (tQ_e + (1-t)Q_m) \quad (2.21)$$

The dual form of the optimization problem is formulated with the stored energy matrices as

$$Q_{lb} = \max_t \min_I 2\omega W_t \quad (2.22)$$

subject to $P_{rad} = 1$

where $0 \leq t \leq 1$ and $W_t = tW_e + (1-t)W_m$. This results minimization problem can be solved by finding the minimum solution to a generalized eigenvalue of two $N \times N$ -matrices X_t and R , e.g. the current density that solve $\max_t \min \text{eig}(X_t, R)$ are the current density that corresponds to Q_{lb} .

Normally, modern communication devices are constituted by an antenna region and a ground. For example, the previous simple mobile phone model has the two regions as shown in Figure 2.7. The yellow embedded antenna region (Ω_A) is where currents \mathbf{I}_A are controllable and the currents \mathbf{I}_G on the grey ground (Ω_G) are induced by the active currents from Ω_A . A discretized EFIE can be derived as

$$\begin{bmatrix} Z_{AA} & Z_{AG} \\ Z_{GA} & Z_{GG} \end{bmatrix} \begin{bmatrix} \mathbf{I}_A \\ \mathbf{I}_G \end{bmatrix} = \begin{bmatrix} \mathbf{V} \\ \mathbf{0} \end{bmatrix} \quad (2.23)$$

Therefore, the calculations or optimization of Q-factor can be done only using \mathbf{I}_A , which are less complex.

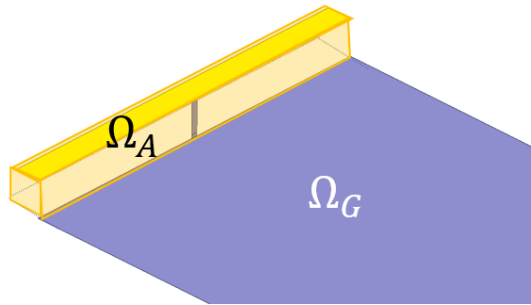


FIGURE 2.7: Controllable (Ω_A) and uncontrollable (Ω_G) in an antenna terminal.

The significance of the Q-factor is not only with bandwidth, it is proved

related also to polarizability for small antennas by the limitation of D/Q quotient. The authors in [36] solved the problem on optimal current for either maximum D/Q quotient (or G/Q) or super-directivity designs by adding constraints to form the convex problem on the limitation of Q-factor for given directivity. In optimizing D/Q quotient, a far-field F vector is defined as projection of radiation toward direction $\hat{\mathbf{r}}$ on a polarization $\hat{\mathbf{k}}$, it is a $N \times 1$ matrix:

$$\hat{\mathbf{k}}^* \cdot \mathbf{F}(\hat{\mathbf{r}}) = \frac{-jk\eta_0}{4\pi} \int_{\Omega} \hat{\mathbf{k}}^* \cdot \mathbf{J}(r_1) e^{jk\hat{\mathbf{r}} \cdot \mathbf{r}_1} dV_1 \quad (2.24)$$

$$\text{and } \lim_{r \rightarrow \infty} r \mathbf{E}(\mathbf{r}) e^{-jkr} = \mathbf{F}(\hat{\mathbf{r}}).$$

The optimization of D/Q quotient is formulated as the following convex problem.

$$\begin{aligned} & \underset{I \in \mathbb{C}^N}{\text{minimize}} \max(\langle I, \mathbf{w}_e I \rangle, \langle I, \mathbf{w}_m I \rangle) \\ & \text{subject to } \langle f(\hat{\mathbf{k}}, \hat{\mathbf{r}}), I \rangle = -j \end{aligned} \quad (2.25)$$

where D_p is partial directivity and \mathbf{w}_e and \mathbf{w}_m are $N \times N$ -matrices acting upon current density coefficient vector I that satisfy $2\omega W_{e/m} \approx \langle I, \mathbf{w}_{e/m} I \rangle$. The problem can be solved using *cvx* optimization on Matlab [37]. In addition, one can utilize the discretized EFIE in 2.23 to calculate the optimal quotient for embedded antennas.

2.3 Examples of antenna evaluation using Q-factor and MoM

2.3.1 Bandwidth estimation and optimization for IoT miniature antenna

Long-range and low power communications, such as LoRa, are being deployed worldwide, resulting in the rocketing development of the Internet of

Things (IoT) in recent years. The ultra narrow band, the chirp spread spectrum or FSK modulations allow in fact elevate sensitivity and communication range in a trade-off with bandwidth [38]. Nevertheless, the main concerns for the antenna design procedure are the miniaturization trend for IoT devices and the differences in frequency bands of different world regions. Europe has adopted the 863 – 870 MHz band, Asia uses the 920 – 925 MHz band, Australia’s is within 916 – 918 MHz, while America has chosen the band 903 – 928 MHz. A wide-band antenna covering 863 – 928 MHz would be optimal, yet hard to perform for a single antenna. This work tries to develop a method to tackle both of these problems.

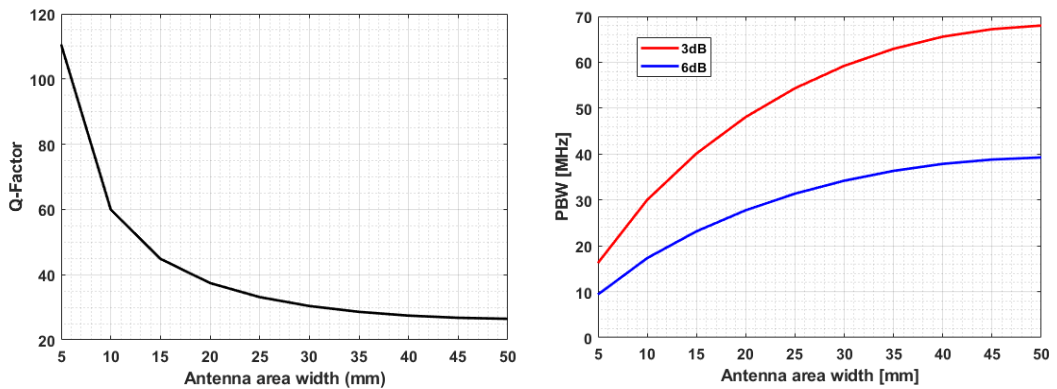


FIGURE 2.8: Low-bound Q-factor as function of antenna width (left) and 3 dB potential bandwidth (red) and 6dB potential bandwidth (purple) as function of antenna width (right).

The main goal of this work is to design a miniature antenna that can perform in both European and Australian LoRa band (which includes Asian band). In other words, the antenna is to be designed covering 863 – 870 MHz as a lower band and 915 – 928 MHz as a higher band, with a -6 dB criteria. This is a pragmatic solution for the industrial mass intercontinental production scale.

To evaluate the potential bandwidth, the same meshing procedure for MoM is done for a 30×50 mm² terminal. The terminal has $ka \approx 0.53$,

which is considered as miniature. As supposed by Chu, miniature antennas normally have a single narrow bandwidth due to high Q-factor [33]. The Q-factor is hence studied as a function of the antenna occupation volume. From Figure 2.8-left, the metric falls rapidly with the clearance width increases. This leads to a reverse trend in bandwidth as shown in Figure 2.8-right. The -3 dB potential bandwidth increases from 18 MHz to 68 MHz while -6 dB potential bandwidth rises from 10 MHz to 40 MHz. In general, Q-factor illustrated the matching capability of a single resonance. Therefore, an antenna on the described terminal is hard to cover the bands required let alone the fact that its volume is around 5 mm to 20 mm leaving place for other components.

To address the narrow band problem, several works exploit matching circuits to enlarge the bandwidth [39], to suppress undesired harmonics, and to obtain a multi-band behavior. Matching networks with lumped components, even of higher orders, are highly suitable for miniature antenna designs thanks to their flexibility and small occupied volume. However, the total efficiency should be carefully taken into account because of the additional loss from lumped components.

The antenna design is presented in Figure 2.9 and is modeled using ANSYS HFSS software. The geometry is a meandered Inverted-F Antenna (IFA). The meandering feature helps to reduce significantly antenna's size. It occupies small free-ground area of $13 \times 30 \text{ mm}^2$ with 1.05 mm strip-line width (w). The antenna is matched using the short circuit placed at 5 mm from the feeding port. The overall area of antenna and ground is $50 \times 30 \text{ mm}^2$, and a 0.8 mm thick FR4-epoxy substrate is used.

To evaluate potential bandwidth, Q_z is adopted as a comparison metric. Antenna's Q-factor is calculated by equation (2.17) from [27], including the loss from the copper conductor and dielectric substrate. The width of the IFA trace w , which is the most influential antenna parameter, is tuned. The

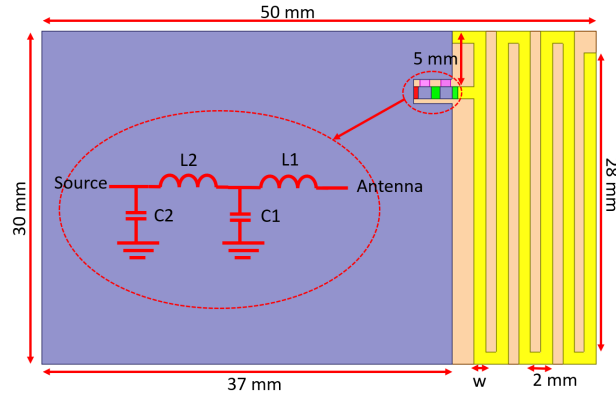


FIGURE 2.9: Meandered antenna structure with matching network.

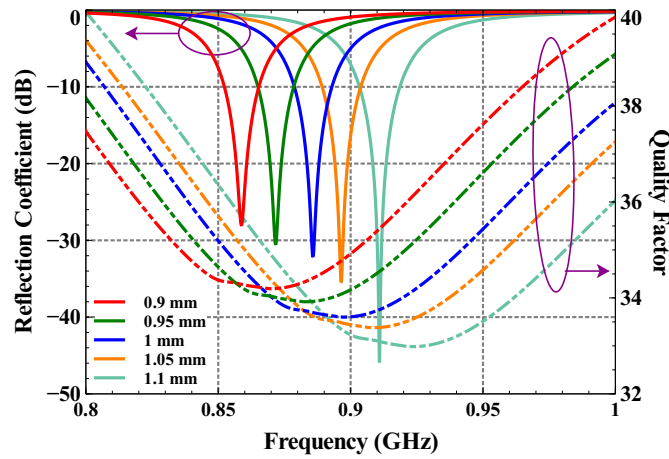


FIGURE 2.10: Reflection Coefficients and Q-factor of antenna without matching network as functions of w .

antenna's return loss and Q_z are presented in Figure 2.8-left within 860 – 915 MHz. Apparently, a small change in the value of w results in a large shift in resonance. It is also clear that Q_z around 34 which is much lower than 48 for the same volume in the perfect case of Figure 2.8-left. In [40], the authors explain the difference by employing the ohmic loss in the surface and $Q_{lossy} = eQ_{lossless}$, where e is efficiency.

In this work, the two required bands are essentially located close to each other. A double band design strategy is illustrated as follows. At first, the value $w = 1.05$ mm was used as its resonance to cover the low frequency of high resonance. Then, the method presented in [39] is applied to find

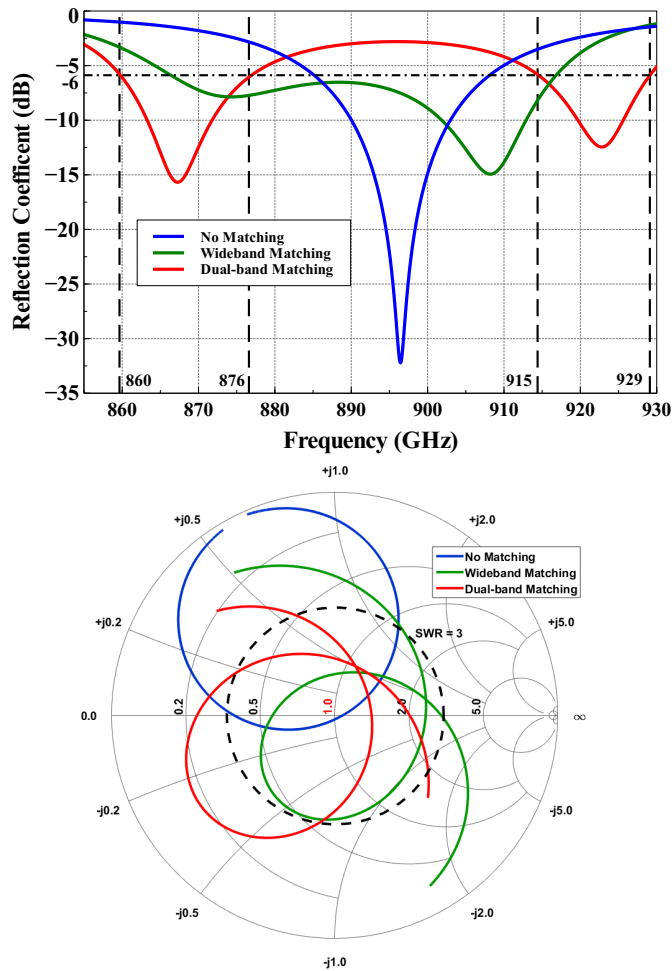


FIGURE 2.11: Reflection Coefficients of antenna with matching network.

an optimal broadband matching network. With values of L_1 , L_2 , C_1 , and C_2 are set to 39.9nH, 27.8nH, 1.8pF, and 6.5pF, respectively, the bandwidth is doubled compared with the raw antenna. A wideband -6 dB matching ranging from 866 MHz to 917 MHz is obtained, which is not sufficient to fulfill the specification.

In the second step, a new matching network is designed to separate the single band into two separate bands. This modification is achieved by moving the crossing point of the loop in the Smith chart to the center as shown in Figure 2.11. Finally, the matching network are updated its values to 27.2nH, 24.8nH, 2.1pF and 8.4pF so that the antenna can cover 860 – 876 MHz and 915 – 929 MHz bands.

2.3.2 Directivity boundary with respect to a certain bandwidth

Optimization of antenna directivity is certainly interesting for many applications. For small radiators, a high directivity is hard to obtain due to the excitation of different characteristic modes [27], [41]. A full antenna board (without ground) is used as an example. The board is $30 \times 50 \text{ mm}^2$ ($x \times y$) size. Delaunay triangulation, illustrated in Figure 2.12, gives:

- 735 points
- 1360 triangles
- 1986 edges

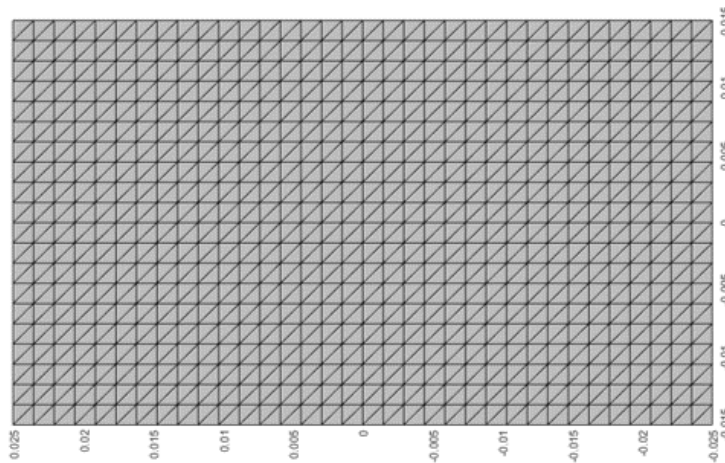


FIGURE 2.12: Segmentation of a 2D rectangular.

The currents on the board are optimized for different polarization and directions. The center optimized frequency is 868 MHz. The results for optimized D/Q are shown below.

Vertical omnidirectional pattern in xOz and yOz plane:

The currents on the board are first optimized to achieve a minimum D/Q quotient at $+Oz$ -direction with polarization \hat{k} along Ox and Oy . Interestingly, Figures 2.13 and 2.14 show that vertically omnidirectional patterns are

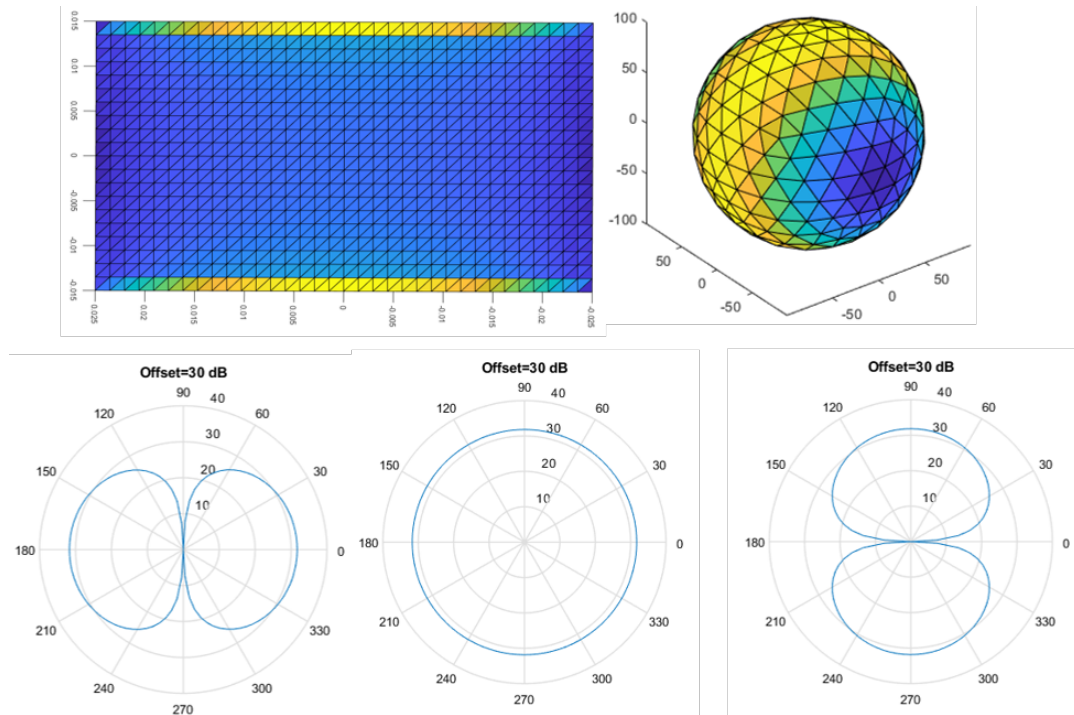


FIGURE 2.13: xOz vertical omnidirectional pattern obtained by optimized D/Q.

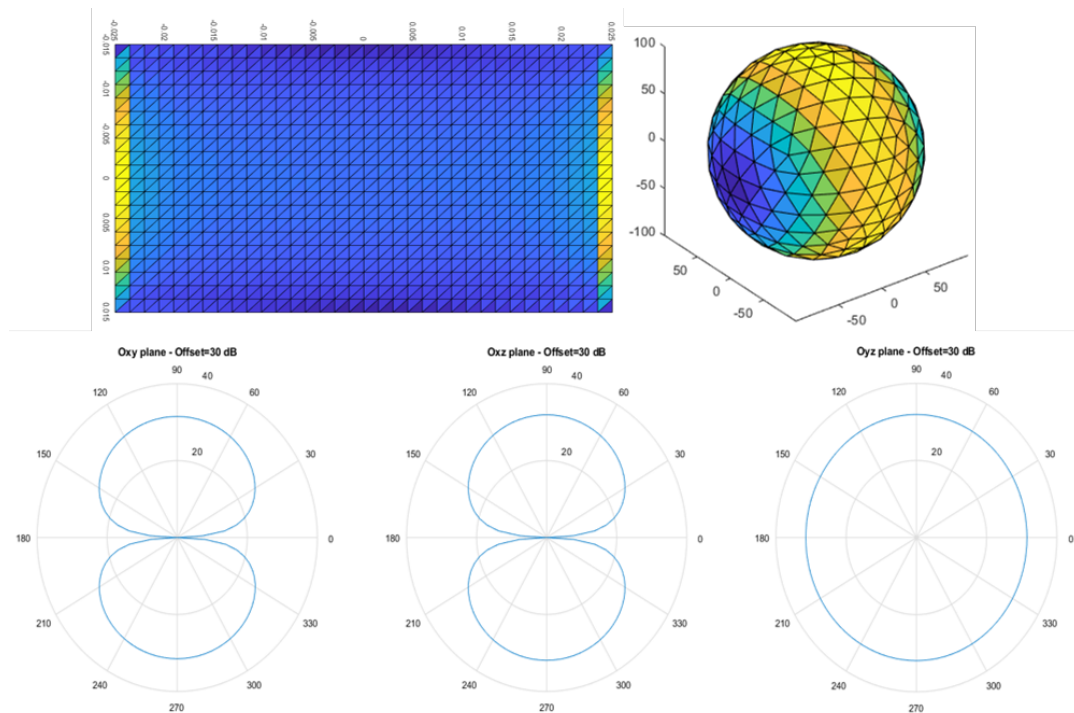


FIGURE 2.14: yOz vertically omnidirectional pattern obtained by optimized D/Q.

obtained instead of directional ones. The vertically omnidirectional patterns are achievable thanks to the currents at the edges of the board. Concretely,

for the xOz pattern, the currents are concentrated at long edges and the yOz pattern has them concentrated on the short edges. The radiation pattern corresponds to these currents and the 3 principal cuts xOy , xOz , and yOz of the given pattern. The direction of maximum gain is in $+Oz$ -direction with $D = 1.85$ dBi and $D = 1.92$ dBi for xOz pattern and yOz pattern, respectively.

Horizontally omnidirectional pattern in xOy plane:

Also with polarization \hat{k} along Ox and Oy , but the currents optimized for either $+Ox$ -direction or $+Oy$ -direction gives also a horizontally omnidirectional pattern. A currents configuration that manifests a horizontally omnidirectional pattern, nevertheless, is harder to comprehend. It is shown in Figure 2.15 that the current density is densest at all edges' centers and gradually diminishes to the center of the board. A realization of this kind of current must be complex as there is not any obvious way in reality to obtain this configuration. The maximum directivity is 1.83 dBi.

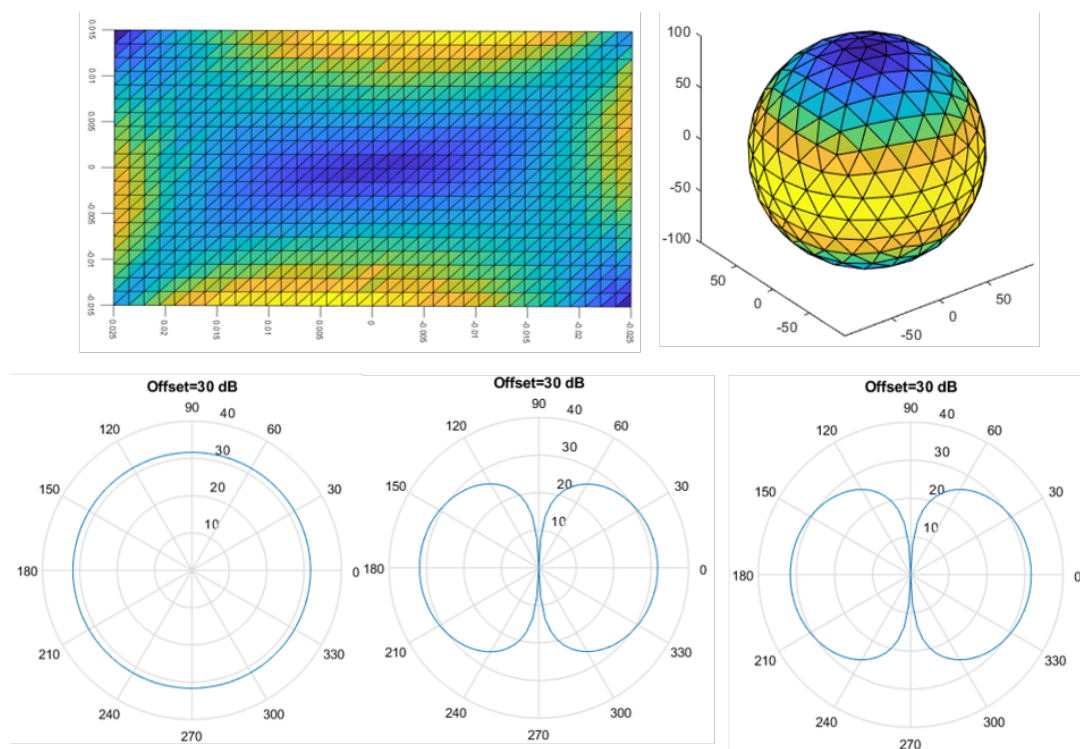


FIGURE 2.15: xOy horizontal omni-directional pattern obtained by optimized D/Q .

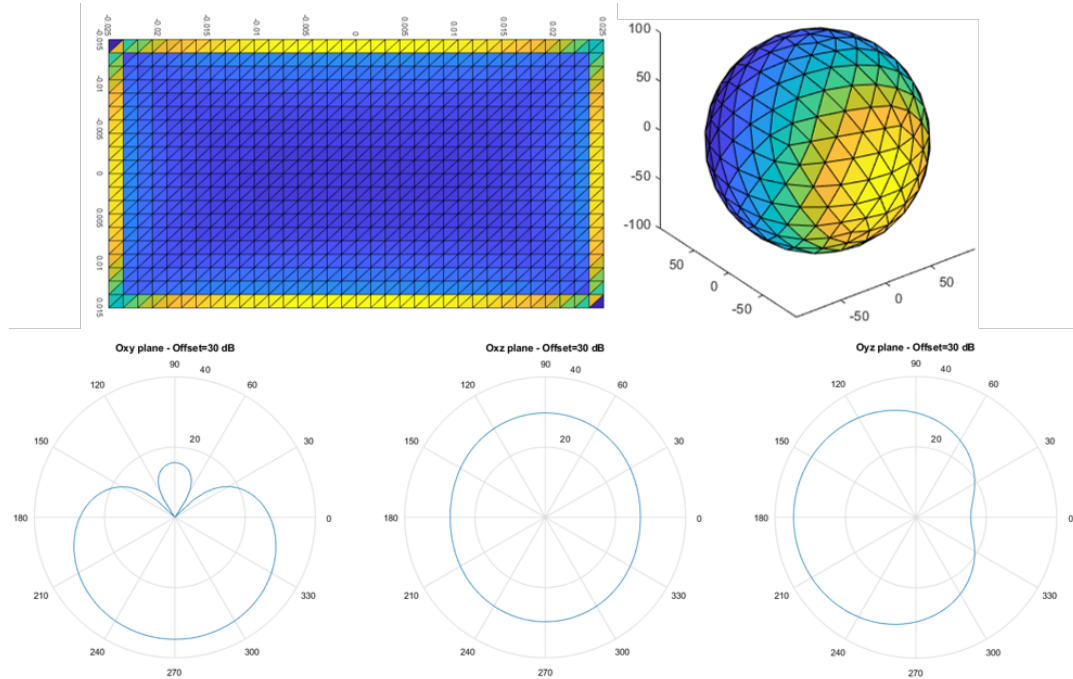
Directive pattern towards $+Ox$ -direction and $+Oy$ -direction:

FIGURE 2.16: Ox directional pattern obtained by optimized D/Q.

Similarly and more importantly for directivity optimization, the currents are also optimized for directive patterns toward $+Ox$ -direction and $+Oy$ -direction for a polarization \hat{k} along Oz . The directivity is 4.34 dBi for $+Ox$ -direction pattern and 4.73 dBi for $+Oy$ -direction, respectively. It should be reminded that an optimization for $+Oz$ -direction gives the vertically omnidirectional patterns, as mentioned, instead of directive ones. It might be the currents configuration that manifests an omnidirectional pattern that gives a better bandwidth.

Optimizing an embedded antenna for a $-Oy$ -direction:

The antenna board is $66\text{mm} \times 22\text{mm}$ ($x \times y$) of size. Delaunay triangulating the board with $dx = 2\text{mm}$ gives:

- 408 points

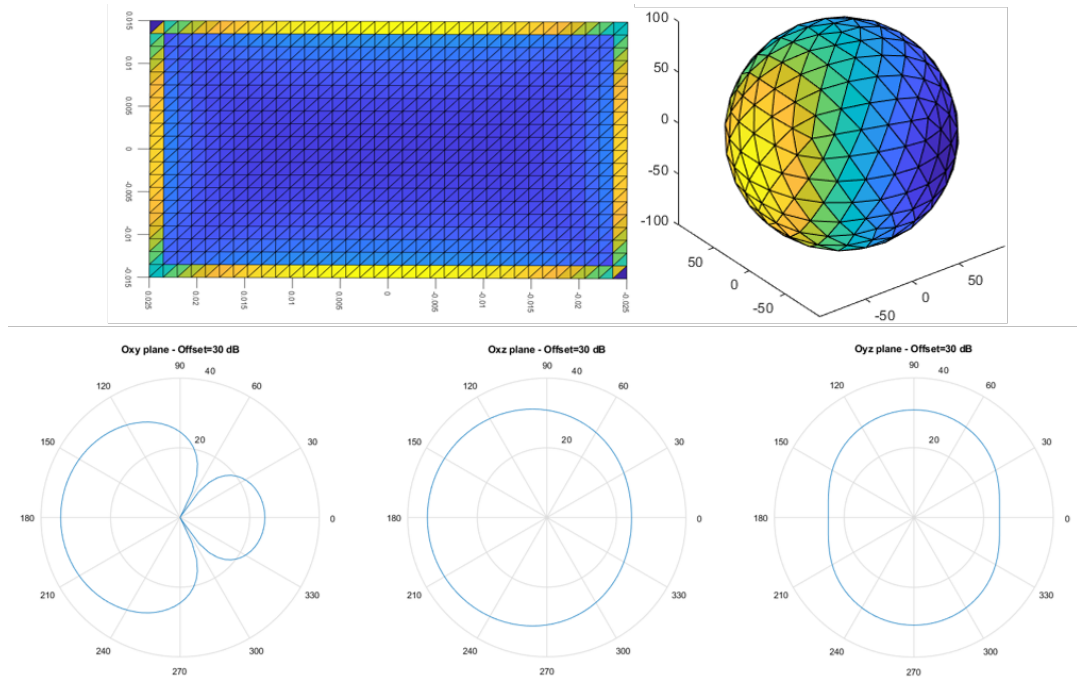


FIGURE 2.17: Oxy directional pattern obtained by optimized D/Q.

- 726 triangles
- 1045 edges

The antenna is integrated at the $-Ox$ -direction occupying an area of $22 \times 22 \text{ mm}^2$ ($x \times y$). The rest is a ground plane where currents are induced, its area is $44 \times 22 \text{ mm}^2$ ($x \times y$). The antenna and the ground are marked separately as in Figure 2.18 with vector and non-vector areas. The center optimized frequency is 868 MHz again.

The given optimized D/Q has $D \approx 3.53 \text{ dBi}$ toward $+Oy$ -direction and $Q \approx 33$. The radiation pattern is given below. The currents that give optimized D/Q are illustrated In Figure 2.19.

The currents illustrated in those above-figures sparks a clever idea for antenna design. If one is to design an antenna with certain criteria in terms of bandwidth and directivity, he/she can optimize it using the described method and then try to design the physical structure that can manifest the

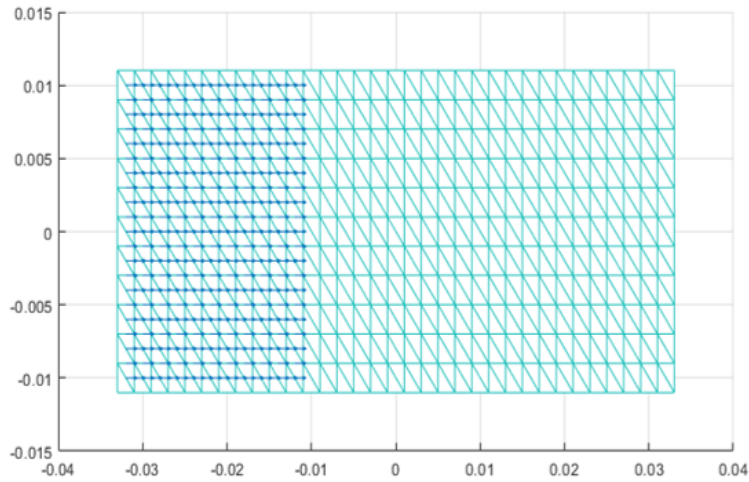


FIGURE 2.18: Board zoning: vectors indicating embedded area on the terminal, non-vectorred means GND (the scales are not the same along Ox and Oy -directions).

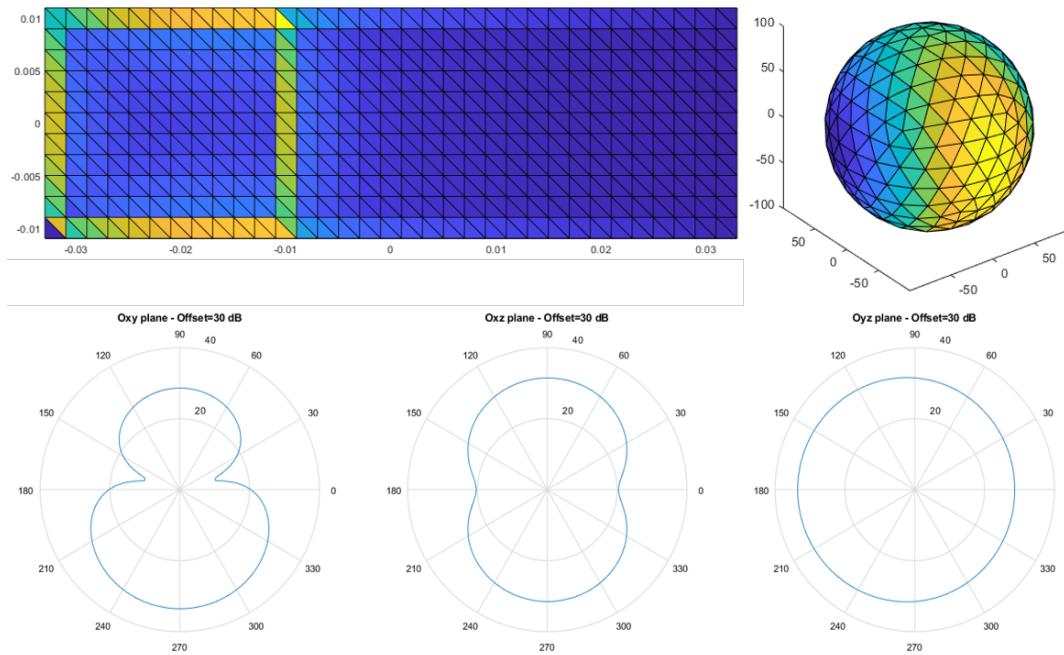


FIGURE 2.19: Oy directional pattern of embedded antenna obtained by optimizing D/Q .

currents as given. This idea is tested in the work [42] showing that the currents on the antenna are close to the outputs of the optimization hence give a relatively similar bandwidth.

2.4 Evaluating effect of narrow clearance on mobile phone antenna

2.4.1 Parametric studies of a mobile terminal

Taking the simplistic model of the mobile antenna in Figure 2.2, we study the main geometrical parameters, including the length of the ground, the length of the patch, and the width of the ground clearance. The antenna is dedicated for sub-GHz band of cellular systems around 900 MHz. It should be noted that although the antenna is small, the big ground plane can excite different modes (view characteristic modes analysis for coupling element antennas) hence the overall bandwidth potential is high. It can be explained with ka is approximately 3.2 where a is the diameter of the circumscribing the whole structure. A structure with $ka > 1$ can excite different modes and the estimation of Q-factor might underestimate the real Q-factor. Nevertheless, the current density is still much higher on the antenna than on the ground plane, hence the bandwidth is expected to be narrow.

In this part of the work, Q_e , Q_m and Q_Z are determined from the currents obtained from exciting the antenna at the feeding point at 900 MHz in Figure 2.2 on the right. The calculations are done using the MoM implementation code on Matlab by Makarov [21]. There are some additional calculations of the stored energies, which resemble the realized EFIE in the original code. It is noted that Q_I is $\max(Q_e, Q_m)$. The correctness of these calculations is assured by running it for an increasing density mesh until the outputs become converged. The density of the mesh is not necessarily homogeneous on the structure. For example, it is found that a 4236-edge mesh, shown in Figure 2.20, with a denser mesh grid at the top of the ground and the antenna is sufficient for accurate Q-factors.

From Figure 2.21, the length of the ground's longer edge is varied from

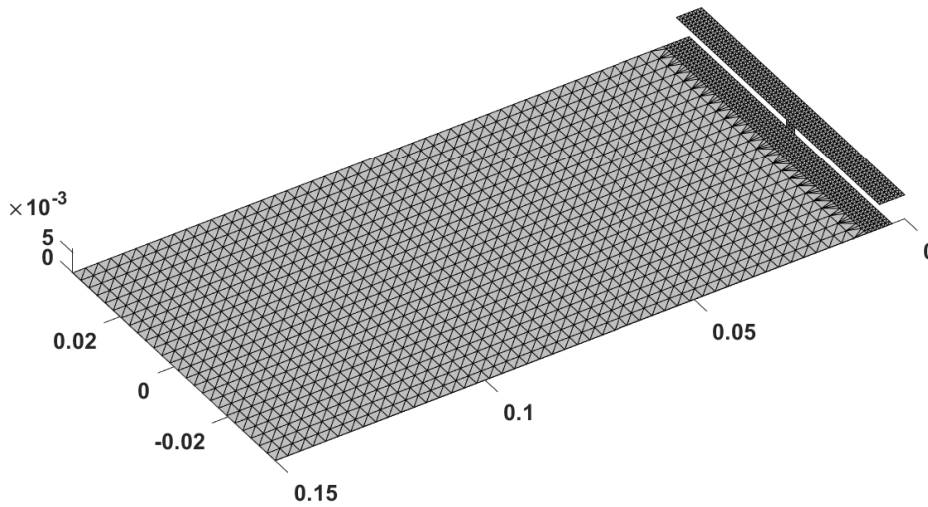


FIGURE 2.20: Mesh for simplistic model of a mobile phone.

12 mm to 147 mm. Also with a clearance of 3 mm width, the whole terminal has length varied from 15 mm to 150 mm. This is translated into varying ka from 1.4 to 3.2. As can be seen from Figure 2.21, the Q -factor from the given excited antenna decreases exponentially from 265 to 11 with the lengthening of the long edge. The minimum of Q -factors is around 120 mm or $ka \approx 2.8$. The Q -factors then raise a bit at the end of the graph, indicating that the optimal mode is passed.

In the comparison of Q_I and Q_Z , we note that they start to separate from 75 mm of edge length or $ka \approx 2.8$. The biggest difference is near the minimum of Q -factors. From 105 mm upward, increasing the length of the ground does not seem to improve the Q -factor much. Finally, the full model (length = 150 mm) has $Q_I \approx 11$ and $Q_Z \approx 9.5$, as stated in the example above.

In Figure 2.22, the patch's length, varied from 3 mm to 75 mm, has similar effect. The Q -factor decreases significantly with the lengthening of the patch. Q_I and Q_Z start to deviate from 9 mm patch length. A constant difference of around 2 between Q_I and Q_Z from 27 mm patch length upward is also apparent.

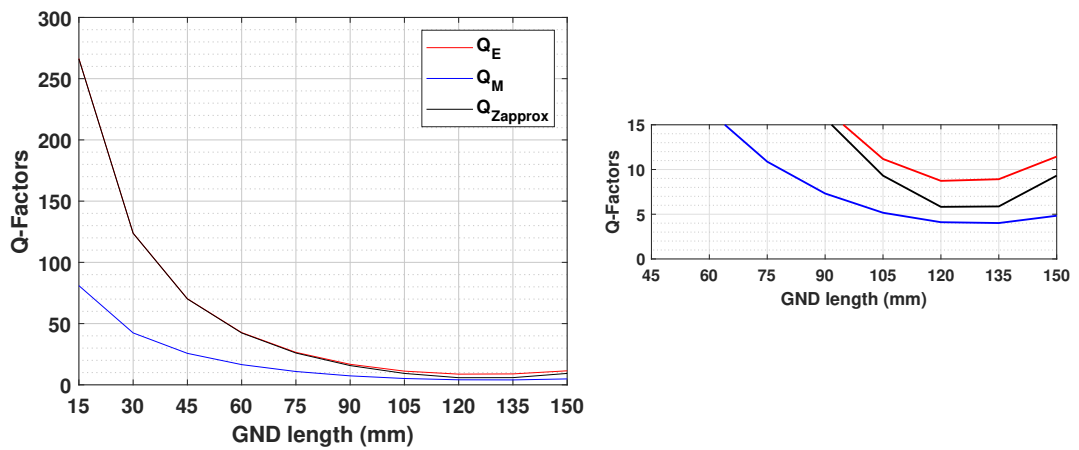


FIGURE 2.21: Parametric study of the length of GND. Full parametric scale is on the left and zoomed one is on the right.

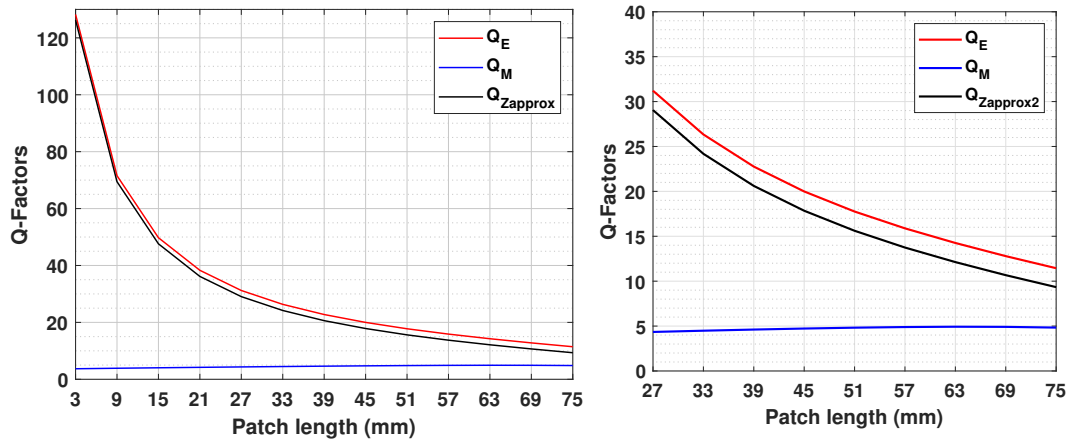


FIGURE 2.22: Parametric study of the length of the horizontal patch. Full parametric scale is on the left and zoomed one from 27mm to 75mm is on the right.

Interestingly, enlarging the ground clearance area can linearly improve the Q-factors. There are two designs with patch lengths 45 mm and 75 mm, respectively. A constant difference around 2 between Q_I and Q_z are seen for both structures regardless of clearance size. This can be seen from the parametric study of the patch's length. When the patch is full size, Q_I decreases from 28 to 14 if we enlarge the clearance from 0 mm to 6 mm width. Similarly for a 45 mm patch, Q_I decreases from 15.5 to 8.9. It is clear and important evidence that if we are to reduce the clearance's width from 6 mm

(still exists in many mobile phones nowadays) to 0 mm (the objective of mobile phone manufacturers in the future), half of the bandwidth are expected to be reduced, at most.

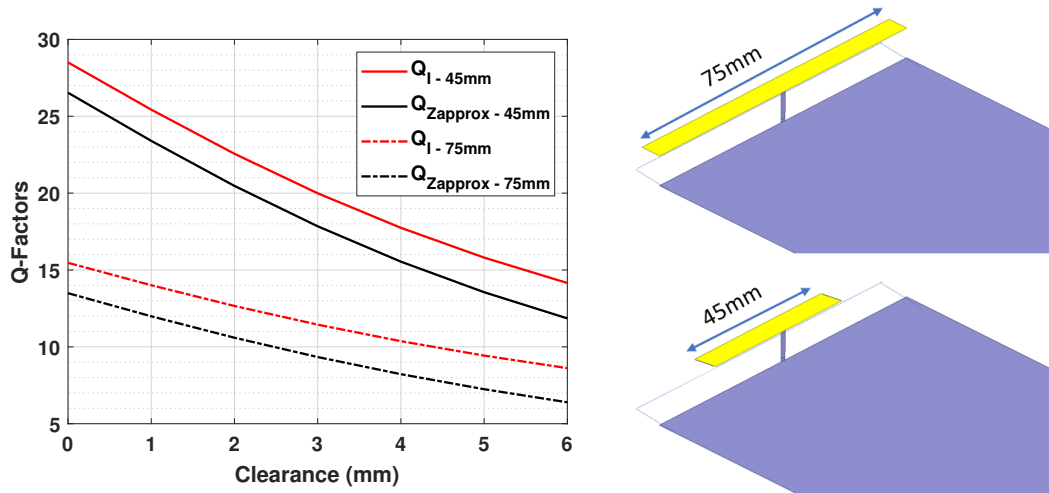


FIGURE 2.23: Parametric study of the width of the clearance's width for two structures width 45mm and 75mm lengths patch.

2.4.2 2D and 3D geometries

Many good designs in the literature require only a planar structure. However, when the free-ground area is becoming limited, an additional dimension might be helpful to achieve a certain bandwidth. This work studies the importance of ground clearance by analyzing the low-bound Q-factor. Also, this studies the bandwidth considering adding dimension to a planar structure.

The structure in Figure 2.2 is studied. The vertical line is changed to a vertical plate because the position of it is not definitive. Together with the patch and the ground clearance, the vertical plate contains the active currents. This part is the embedded part where the active currents are free to change as long as they respect Maxwell's equations. It bases on the fact that designers can alter their antenna designs. Nevertheless, the optimal currents might still not be easily realizable by etching or cutting the parts.

At the top edge of the ground plane and the antenna part, the current density is seen higher than the bottom part. Therefore, these areas are created by having a higher density mesh. It can be done by separating the ground into two segments that the top has denser mesh than the bottom. Between the two segments is a transition line where the point distribution is the same, for the sake of stitching two parts.

The seven structures are illustrated in Figure 2.24 and described as follow:

1. 2D structure with $75 \times 150 \text{ mm}^2$ size. Structure 1 in Figure 2.24.
2. 3D structure composes the 2D structure and a full-length vertical plate embedded, e.g. a vertical $75 \times 6 \text{ mm}^2$ plate. Structure 2 in Figure 2.24.
3. 3D structure composes the 2D structure and a 60%-length vertical plate (middle) embedded, e.g. $45 \times 6 \text{ mm}^2$ plate placed in the middle. Structure 3 in Figure 2.24.
4. 3D structure composes the 2D structure and a 60%-length vertical plate (corner) embedded, e.g. $45 \times 6 \text{ mm}^2$ plate placed in the corner. Structure 4 in Figure 2.24.
5. 3D structure composes Structure 2 and a full-length horizontal patch embedded, e.g. a horizontal $75 \times 6 \text{ mm}^2$ patch. Structure 5 in Figure 2.24.
6. 3D structure composes Structure 3 and a 60%-length vertical plate (middle) and patch embedded, e.g. a horizontal $45 \times 6 \text{ mm}^2$ patch placed in the middle. Structure 6 in Figure 2.24.
7. 3D structure composes Structure 4 and a 60%-length vertical plate (corner) and patch embedded, e.g. a horizontal $45 \times 6 \text{ mm}^2$ patch placed in the corner. Structure 7 in Figure 2.24.

Table 2.4 shows the performance in terms of the Q-factor at 900 MHz of the defined structures. The structures are repeated with 2% and 4% of clearance widths with respect to the full length of the terminal, e.g. 3 mm and 6 mm wide. The structures in the same group are compared to the planar 2D structure also in that group to show the relative bandwidth in percentages.

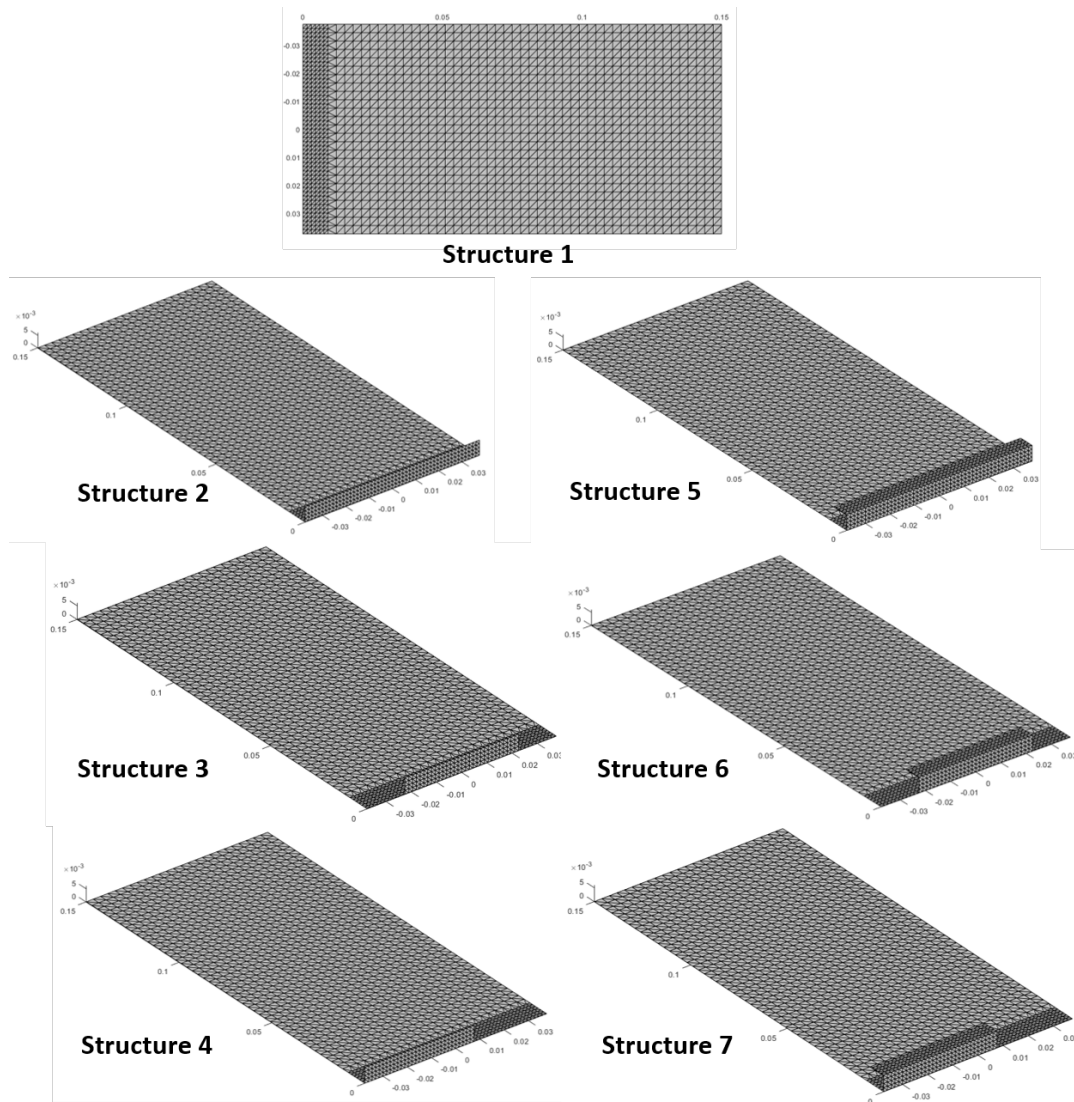


FIGURE 2.24: The 7 study geometries of simplistic mobile phone.

Apparently, reducing from 4% to 2% clearance width makes a big difference in maximum potential bandwidth. An estimated 46% loss of bandwidth is expected due to the increase from 9.1 to 16.9 in optimal Q-factor. The difference, however, is smaller for full-length vertical and horizontal plates in

TABLE 2.4: Comparison of different configuration of antenna geometries 2D and 3D.

Index	Descriptions	Clearance	Q-factor	Max PBW improvement
1	Structure (1)	2%	16.9	ref. case
2	Structure (2)	2%	8.8	190.9%
3	Structure (3)	2%	11.3	149.3%
4	Structure (4)	2%	10.4	162.4%
5	Structure (5)	2%	7.8	216.2%
6	Structure (6)	2%	10.3	163.3%
7	Structure (7)	2%	9.3	182.0%
8	Structure (1)	4%	9.1	ref. case
9	Structure (2)	4%	6.5	140.6%
10	Structure (3)	4%	7.5	121.6%
11	Structure (4)	4%	7.2	127.2%
12	Structure (5)	4%	6.0	152.1%
13	Structure (6)	4%	7.1	127.9%
14	Structure (7)	4%	6.7	135.9%

comparison with the 60%-length plates. For instance, structure (2) reduces Q-factor from 8.8 to 6.5 when clearance's width rises, while structure (3) does from 11.3 to 7.5. In other words, there will be more improvements by using 3D volume in terms of bandwidth when only 2% of ground is spared for clearance, in comparison with 4% case.

A horizontal patch is helpful to gain max PBW, however, not significantly. Around 20% additional PBW can be achieved by using it for a 2% clearance case. For a 2% case, a full-length vertical structure added to a planar antenna can improve up to nearly 191%, likewise, a 60%-length structure helps gain 62% if one can positioning smartly. Meanwhile, only 40.6% and 27% improvements are seen in the 4% clearance case for full-length and 60%-length vertical structures, respectively.

Interestingly, an additional 10% PBW can be achieved if the 3D part of the antenna place at the corner instead of in the middle. This might be related to the characteristic mode of the structure. The improvement in the corner cases compared to the middle can be explained visually from Figure 2.25. It is clear that the *optimized currents* on the vertical plate are concentrated at one

vertical edge.

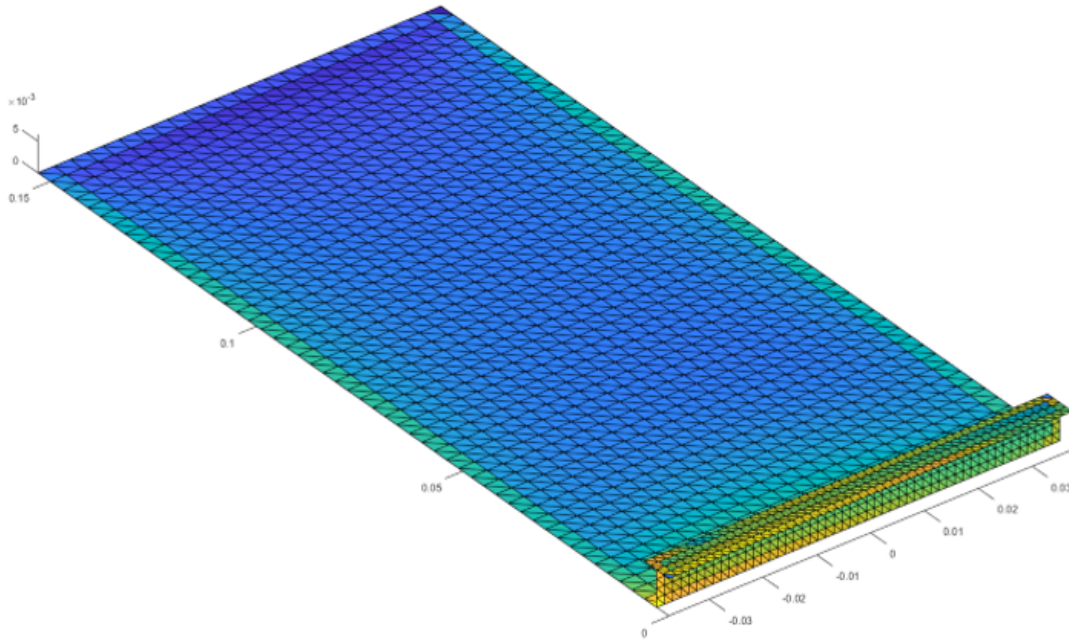


FIGURE 2.25: The optimal surface currents on the clearance, the vertical plate and the patch.

2.5 Conclusion

This Chapter confirms the trade-off between size-related parameters for a phone is here investigated with respect to their optimal available bandwidth impact using the Q-factor. For all the considered structures, the factor is calculated by extracting the stored energies. MoM is used due to the close resemblance of the EFIE to the calculations of stored energies.

The analysis of the Q-factor in a miniaturized antenna is extremely useful to estimate its potential bandwidth. Thus maximum bandwidth can be derived with a sufficient size of the antenna and a design strategy, like using a matching circuit. Additionally, Q-factor gives information on the optimal bandwidth for a directivity limit. This is certainly interesting if the designer wants to consider a directivity-bandwidth trade-off for small antenna design.

Also from the analysis, it is clear that the reduction in ground clearance in mobile phone terminals deteriorates the bandwidth of the embedded sub-GHz antennas. The small ground clearance can reduce the available bandwidth to half of the original one. It is also demonstrated that the use of the 3D region at the edges of the phone is necessary to compromise the bandwidth in case the ground's planes becomes bigger and limits the area for antennas. Therefore, this work paves the way for further studies that directly address the small clearance.

Chapter 3

Multi-band multi-element mobile antenna design

3.1 State of the arts on mobile antenna design and genetic antenna optimizations

3.1.1 Recent developments on mobile antenna design

The reduction of the "bezels" in nowadays mobile phones clearly gives it a modern look and improves user experience. However, this trend has an imminent impact on the design of antennas: the potential bandwidth is linearly reduced with the antenna volume allowance, as studied in the previous Chapter. It is worth noted that an antenna can lose up to half of its potential bandwidth if a 6-mm clearance, such as Samsung (fourth model) in Figure 1.4), is to be given up. It is also shown that the use of a second or third plane is necessary to compromise the bandwidth in case the ground's planes becomes bigger and limits the area for antennas.

From the literature, the bandwidth limitation as a function of antenna size has been a mainstream scientific research for long [30], [33], [34], [40]. The effect of minimizing mobile clearance is equivalent to the bandwidth limitation of patch antenna or miniature ones. This problem for mobile phone

bandwidth is recently revisited in the works [43], [44]. In [44], the authors illustrate the effect of the narrow bandwidth for a small antenna by using the unloaded Q-Factor. The authors of [43] again confirm that the ground clearances along the short and long edges of a mobile phone terminal clearly have effects on the bandwidth potential. The work concludes also that the clearance cannot be arbitrary small for any mobile phone.

Conventionally, an antenna can achieve multi-band or wide-band using complex designs, like multi-radiating arms integration. For example, the authors in [45] successfully design their antenna cover octa-band covering 700 – 960 MHz and 1.7 – 2.7 GHz with an $8 \times 70 \text{ mm}^2$ clearance. The use of metal frame (rim) is even more popular in modern mobile phone designs especially to render users a solid feeling of the terminal. However, this serves as an electrical blockage and might introduce undesired coupling effects, hence diminishing radiation efficiency. Nevertheless, many works cleverly modify this metal frame to make high-performance antennas, like in [46]–[48]. The trick seems to be cutting the metal frame into smaller pieces, then using short circuits to manipulate the currents to create either radiating or coupling elements.

Another way to overcome the problem of narrow bandwidth is to use reconfigurability mechanisms [49]–[51]. This method allows the antenna to be simple and flexible to changing environments. In [50], the authors introduced a reconfigurable PIFA based on nested slots. The four integrated PIN-diodes allow the antenna switch to a wide range of frequency bands from 700MHz to 3.55GHz. In [51], an excellent efficiency above 90% for 1.7 – 2.7 GHz, 3.3 – 4.5 GHz, and 5.475 – 6.425 GHz frequency bands is achieved by using a mobile antenna cluster. Unfortunately, the authors did not address the sub-GHz bands where it is most challenging.

While the above-mentioned methods using self-resonance design works well, antenna designers should note that a large portion of energy radiates

out of the solid chassis in a mobile terminal, instead of the radiator. Therefore, the non-resonance coupling element (NCE)-based technique has been systematically studied in [44] and successfully reduces mobile antenna volume. It analyzes the characteristic modes on the mobile phone chassis (GND) which helps enhance the induced currents and hence optimizes bandwidth, especially at sub-GHz bands. Apparently, to overcome the shortage of clearance on mobile phone antenna designs, the method becomes a favorite for commercial products. It is noted that the NCEs in the work is matched by a matching circuit. This is convenient to save volume and achieve up to a bandwidth giving by the equation 3.1 by Bode-Fano limitation [52], [53]. Arguably, this technique heavily relies on the choice of matching the network's components since the overall performance includes losses from them.

$$B \approx \frac{27}{Q\Gamma_{0(dB)}} \quad (3.1)$$

where $\Gamma_{0(dB)} = 20 \log(\Gamma_0)$ is the reflection coefficient given in dB .

3.1.2 Particle Swam Optimization and antenna optimization

Particle swarm optimization is part of the Swam Intelligent (SI) class of Evolutionary Computation (EC). The EC is in turn a subclass of Computational Intelligent (CI) which is a new modern class in Artificial Intelligent (AI) [54]. PSO is one of the most popular SIs, together with the Genetic Algorithm (GA) and Ant Colony Optimization (ACO). As the name suggested, Swam Intelligent algorithms are inspired by the nature optimization processes. For example, ACO is based on the behaviors of an ant colony. Likewise, PSO mimics bird flocking or a swarm of bees looking for food in a large area.

There are 5 principles that any SI algorithm must follow [55]:

- Proximity principle in which the swarm should be able to do simple space and time computations.

- Quality principle in which the swarm should be able to respond to quality factors in the environment.
- Diverse response principle in which the swarm should not commit its activities along excessively narrow channels.
- Stability principle in which the swarm should not change its mode of behavior every time the environment changes
- Adaptability principle in which the swarm should be able to change its behavior mode when it is worth the computational price.

Problems that need to be solved using SI algorithms are normally not convex which means there are *local* and *global* optima. Therefore, conventional well-established methods like *gradient decent* for convex problems are technically inapplicable. Hopefully, the randomness of SI algorithms can tackle this if it is well configured.

SI in general and PSO in particular have iterative procedures. A common PSO algorithm is presented in Algorithm 1. It consists of a population of agents moving in a searching space and interacting with each other to find an optimal location. The behaviors of each agent contain a certain degree of randomness, while the global interaction of the “swam” underlines some intelligence. Although each generation gets the agents to new positions by adding their current positions with their new velocity. In each iteration, the velocities are updated with a random parameter W , known as “inertia” or the momentum from the previous velocity. These velocities are also dictated by a “cognitive” parameter $C1$ and a “cooperation” parameter $C2$. This is quantified in equation 3.2. While moving across the searching space, each agent prefers moving around its best-found position. However, it also keeps hearing other agents’ productivity and update its location coherently. Therefore, the swarm gets to find the best solution through communication and collaboration.

Algorithm 1 : General PSO algorithm.

Initialize: for each agent

- Initialize the particle's position with a uniformly distribution as $P_i(0) \sim U(LB, UB)$, where LB and UB represent the lower and upper bounds of the search space
- Initialize $pbest$ to its initial position: $pbest(i, 0) = P_i(0)$
- Initialize $gbest$ to the minimal value of the swam: $gbest(0) = \operatorname{argmin}_f[P_i(0)]$
- Initialize velocity: $V_i \sim U(-|UB - LB|, |UB - LB|)$
- Set $\kappa = 1$, $stopFlag = \text{false}$, $\text{threshold} = \Gamma$.

repeat

1. Pick up random numbers: $r_1, r_2 \sim U(0, 1)$.

2. Update particle's velocity by

$$V_i(\kappa + 1) = WV_i(\kappa) + C_1r_1(pbest(i, \kappa) - P_i(\kappa)) + C_2r_2(gbest(i, \kappa) - P_i(\kappa)) \quad (3.2)$$

3. Update particle's position by

$$P_i(\kappa + 1) = P_i(\kappa) + V_i(\kappa + 1) \quad (3.3)$$

4. Update $pbest$, $gbest$ and consider terminating condition

if $f|P_i(\kappa)| < f|pbest(\kappa)|$ **then**

Update the best-known position of particle i : $pbest(i, \kappa) = P_i(\kappa)$.

if $f|P_i(\kappa)| < f|gbest(\kappa)|$ **then**

Update the swarm's best-known position: $gbest(i, \kappa) = P_i(\kappa)$.

if $f|gbest(\kappa)| < \Gamma$ **then**

$stopFlag = \text{true}$

else

$\kappa = \kappa + 1$

end if

end if

end if

until $stopFlag = \text{true}$

Output: $gbest(t)$ that holds the optimal solution.

The problem of *local* and *global* optima can be visualized in an example following. Figure 3.1 illustrates the function $\operatorname{sinc}(x) * \operatorname{sinc}(y)$ with x, y have range $[-2\pi, 2\pi]$. In this example, we want to find the maximum point within the 2D searching space. The *local* and *global* optima are in this case where the second derivative of the function equals 0 and the first derivative is positive. The *global* optimum of the function is point **A** at the center. However, there

are several other points like point **B** have also the same mentioned properties, though they are *local* optima. Therefore, if the cooperation $C2$ is not strong enough, the swam will not converge and the agents tend to stay around for very long. If it is too strong and the agents do not have enough degree of freedom, which is governed by $C1$, to move around the searching space, they might fall into a *local* optimum converge rapidly at this point. The trade-off between rapid calculation and reliability solution leads to many studies to upgrade PSO. A thorough analysis of these parameters can be found in [54].

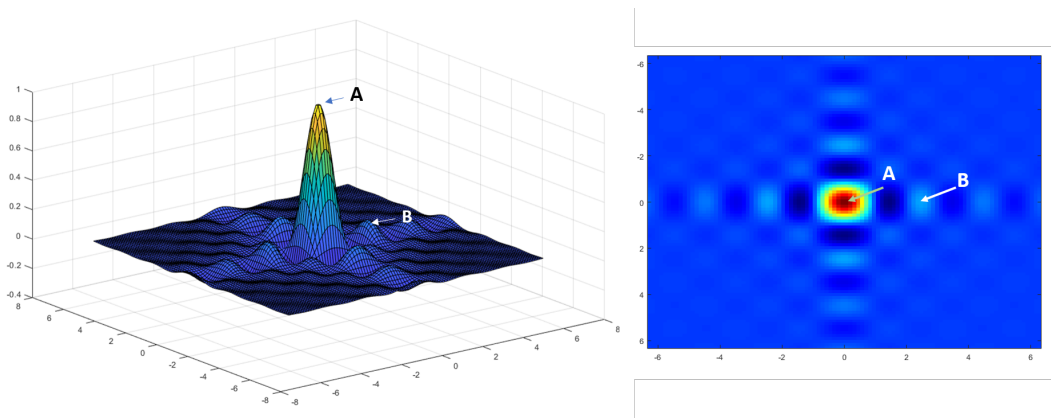


FIGURE 3.1: Graphic illustration of function $\text{sinc}(x) * \text{sinc}(y)$ in 3D (left) and 2D (right) with global optima (A) and local optima (B).

PSO algorithm finds many applications in antenna design and optimization. The main interest is to tackle bandwidth, directivity, or efficiency using the automation process. The algorithm generally gives a result that is not very intuitive to humans. The common application is to calculate magnitude and phase inputs to an array antenna to produce a pattern that is maximized and nullified in a certain direction to gain high throughput [56], [57]. In addition, the algorithm can also be used for an antenna-parasitic element system where it optimizes the applied impedance to each parasitic port for directivity optimization [58]. In [59], the author optimizes a 'spline-shaped' antenna using PSO for duplex communications. Interestingly, the optimization is on different points' coordination. These points in turn dictate the shape of the

antenna and hence can enhance antenna bandwidth. Similar work on an E-shape patch antenna can also be found in [60]. Nevertheless, optimization on the mobile antenna design with matching circuits to solve the problem of very small clearance above has not been seen.

3.2 PSO on mobile antenna design and optimizations

3.2.1 PSO methodology for hybrid antenna designs

Inspired by the work in [59], a hybrid optimization for antenna shape and associated matching networks is derived. The flowchart in Figure 3.2 illustrates the procedure. The calculation of *fitness* value, shown on the right of the figure, includes simulating a generated geometry, exporting the scattering parameters, and calculating the total efficiency after matching with best-matching circuits. The complication of the calculation is also illustrated in Figure 3.3 where it involves utility of HFSS full-wave simulation and Optenni Lab for circuit optimization [61]. Matlab is the main controller in charge of generating new parameters, launching that adherence software, and checking the *fitness* value.

The main terminating criterion in the optimization, *Requirement fulfilling* in Figure 3.3, is a threshold Γ on the total efficiency of the design. However, for many of the designs, we usually put this value to be unachievably high so that the maximum value can be reached. Therefore, a second employed terminating term is *Convergence ϵ* of velocities. For example, the sum of the velocity's square can have a low bound like in 3.4. The convergence of local best is also terminated. The final criterion is a time limit. Many times, the agents need to be free enough so that it scans better the searching space,

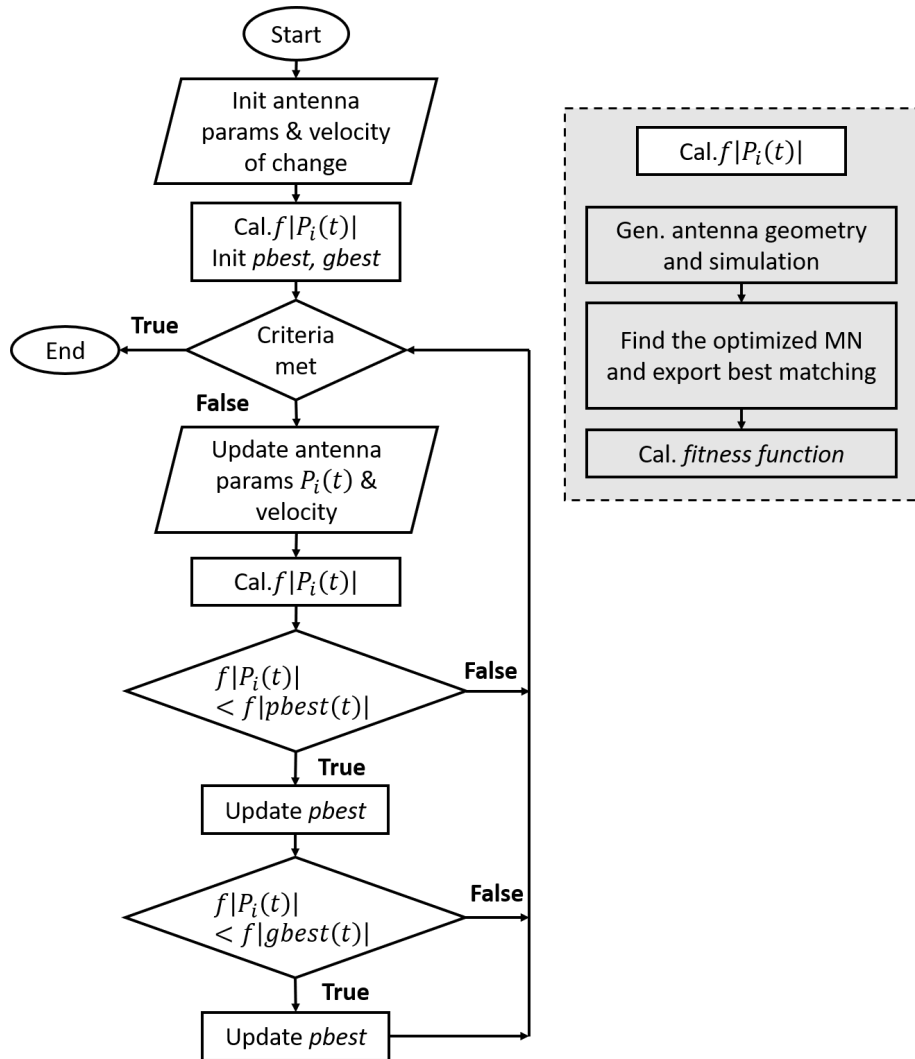


FIGURE 3.2: Flow chart of the optimization procedure using PSO.

e.g. W is sufficiently high. This may cause a huge time-consuming problem, especially for complex structures. Therefore, running time is limited by a maximum of iterations which depends on structures. This condition is namely *Out of iteration* in the same figure. It is worth noting also that this PSO uses a reflective boundary, which was proven effective for convergence.

$$\epsilon = \sqrt{\frac{\sum_{i=0}^N (x_i - \bar{x})^2}{N - 1}} \quad (3.4)$$

With the devised methodology for antenna optimization with a lumped

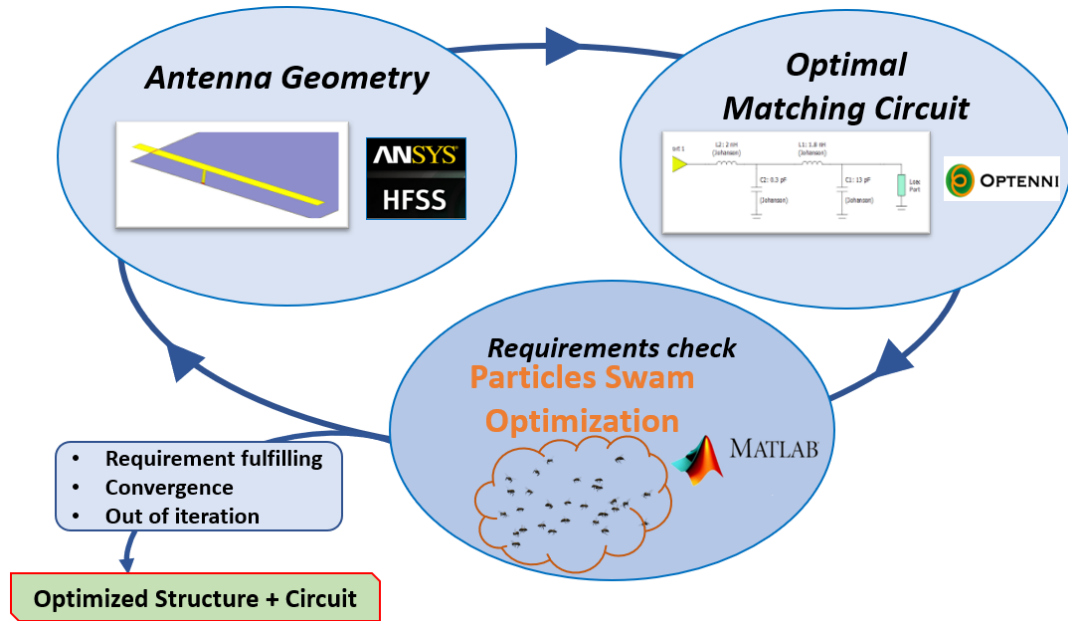


FIGURE 3.3: The iterative procedure for hybrid antenna and MN optimization.

matching network, several tests have been conducted. Some of the earliest ones are for a meandered miniaturized antenna in [8]. The methodology proves advantageous in helping avoid the tedious task of manually tuning antenna parameters. The next sub-sections will utilize this optimization methodology to design different mobile antennas.

3.2.2 1-element or 2-element design for single wide band?

The optimization is put to test in designing a mobile phone antenna that has zero clearance. The design is intended to cover band LTE 12/13/14, GSM850/LTE5, and GSM900 as in Figure 3.4. Therefore the overall-band is 698 – 960 MHz. Such antenna can similarly cover band n5/8/12/14/18/20 of 5G.

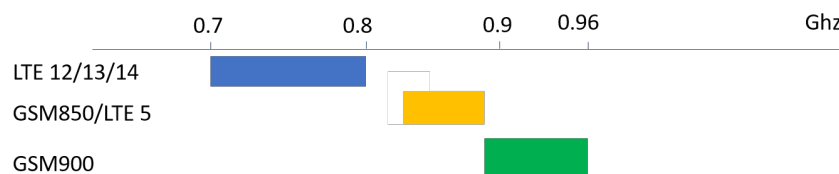


FIGURE 3.4: Different cellular bands at subGHz.

In this work and later ones in this Chapter, the mobile terminal structure is simplified for the sake of reducing optimization time. Fullscreen is made as a large copper plate the size of $(140 \times 73\text{mm}^2)$, a typical size of a large-screen mobile phone (Figure 3.5). It plays the role of a large conductive ground. The yellow horizontal $6 \times 73\text{mm}^2$ patch ($w = 6\text{mm}$) above one end of the ground represents the area for the antenna. Antennas are modeled as simple horizontal patches excited from vertical strips connected to the ground. It is expected that this simplification of antennas structures will improve radiation efficiency. The distance between the patch and the ground is $h = 6\text{mm}$. The vertical strip is 1mm-width.

With such a simple configuration, the design should yield very high radiation efficiency, usually above 90%, regardless of the PSO parameters or the segmentation of the antenna. So, the optimization of the total efficiency is moved to the circuitry part, which can be calculated by Optenni Lab.

In the previous chapter, we learn that the effect of zero-width clearance is detrimental for the bandwidth. The mentioned structure with zero clearance has a Q-Factor of 16 as shown in Figure 2.23. Using the equation 2.12 we estimate bandwidth of around 65MHz for a single element antenna @900 MHz with $\Gamma = -6$ dB. This is certainly not enough to cover the triple-band in Figure 3.4 which are usually used for cellular communications. With the matching network, the Bode-Fano's equation 3.1 is applied giving around 253 MHz @ $\Gamma_0 = -6\text{dB}$ @900 MHz. This is hence barely sufficient for the intended bands, the insignificant loss from copper and dielectric loss can likely help with the matching property.

One-element antenna is indeed designed covering the triple bands with a matching circuit comprised of six lumped components. The vertical strip is placed at the center of the short edge. In Figure 3.7, the antenna can cover the intended 698 – 960 MHz @ $\Gamma_0 = -4$ dB. The minimum total efficiency of this design is -2 dB as illustrated in Figure 3.8.

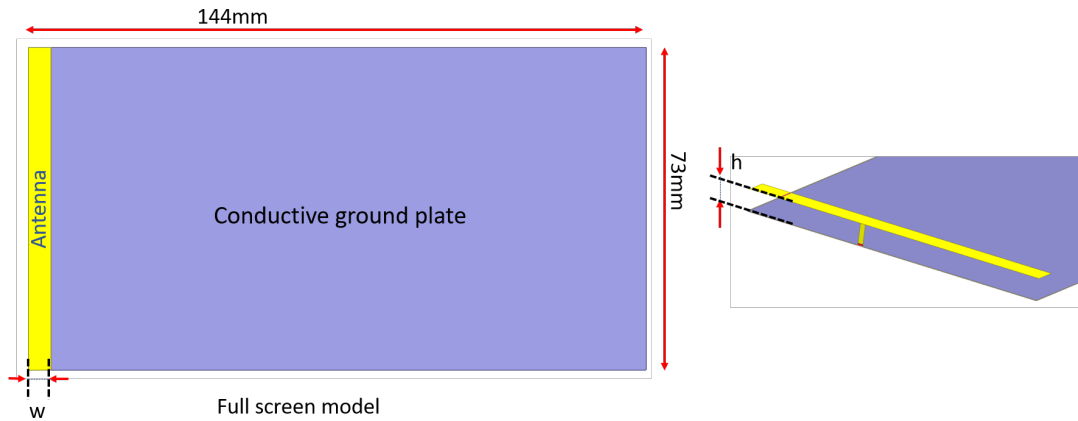


FIGURE 3.5: Mobile terminal structure and antenna geometry.

The main interest of using PSO in this work is to separate cellular sub-GHz bands. One can argue that an antenna system with separate elements, one for band LTE 12/13/14 and another for GSM850/LTE5 and GSM900, is beneficial from the filtering effect.

The PSO algorithm is run with 4 variables:

- Gap (between 2 elements) position
- Gap's width
- First port's position
- Second port's position

The working bands and matching network configuration for the ports are defined in Optenni Lab. Two configurations of matching networks are studied. In the first configuration, the networks are comprised of 2 elements while they are of 4 elements for the second configuration. Not surprisingly, the second configuration has a quicker convergence in under 20 iterations as illustrated in Figure 3.8. In contrast, the first configuration takes more than 60 iterations to finish the optimization. More interestingly, the latter also converges to a higher level of total efficiency, 56%, in comparison with 41% of the prior. This can be explained by one additional degree of matching thanks

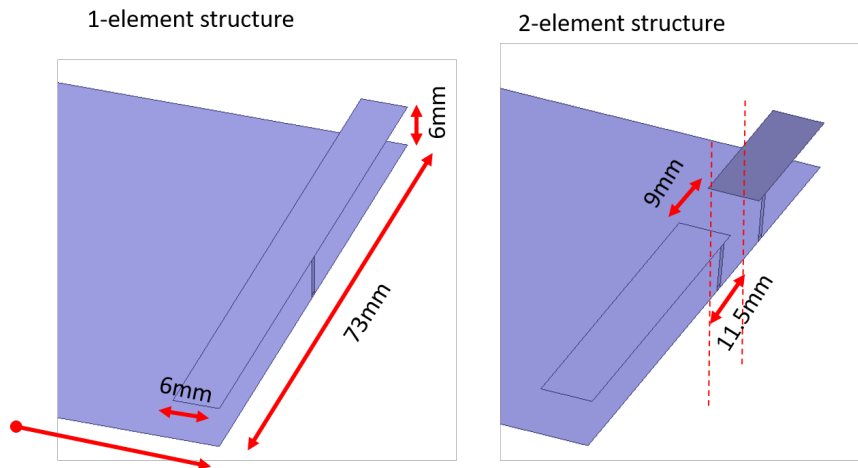


FIGURE 3.6: The designs of manual-tuning 1-element and auto-generated 2-element antennas.

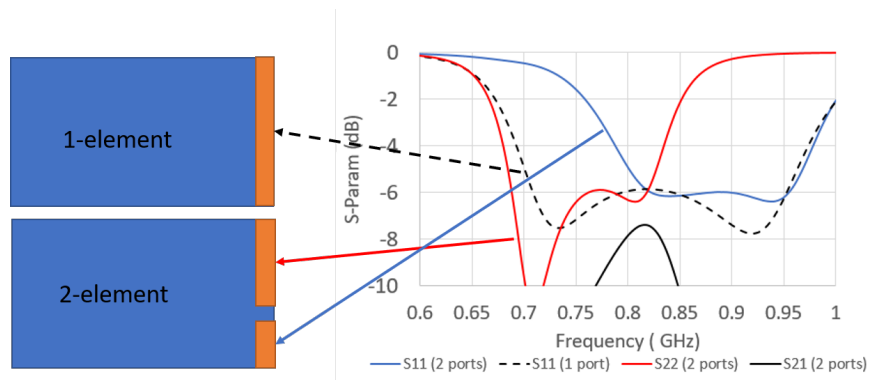


FIGURE 3.7: Matching and isolation for the 2 designs.

to 2 more components of the second configuration. It should be pointed out also that the minimum isolation between the two elements is around 7.5 dB at the intersection of the 2 sub-bands, around 800 MHz. This can be worked around by isolation enhancement techniques [62]–[64] though it is hard to implement in the PSO code.

The design parameters of manual-tuning 1-element and auto-generated 2-element antennas are shown in Figure 3.6. The later though take the same volume has a big gap of 9 mm between 2 elements. Apparently, such a gap can be useful to place other components, such as a headphone jack, a USB port, or a speaker. The combined total efficiency of the two elements is also comparable to a single antenna. Its minimum is around -3 dB. This provides

an interesting solution for the sub-GHz mobile antenna design strategy.

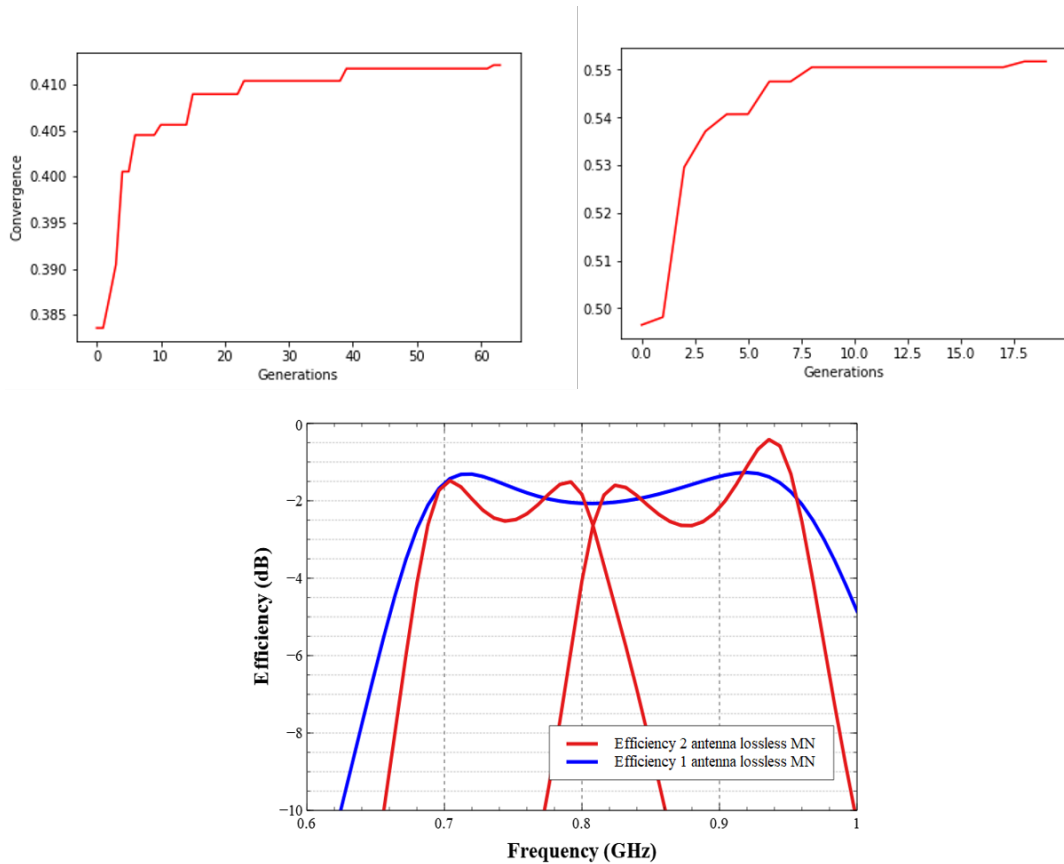


FIGURE 3.8: The convergences of optimization with 2 LC component MN (top left) and with 2 LC component MN (top right). A comparison of the duo obtained bands with single band efficiencies (bottom).

3.2.3 Double bands 2-element antenna design

Push the constrain a little further, we aim for a system of two antennas to cover the 700-960 MHz low band and the 1690 – 2700 MHz high band, which include the mentioned sub-GHz bands and LTE2500 band. This is more challenging for the proposed approach since the volume of the antennas is kept almost the same.

Refer again to Figure 3.5, the sizes of the ground plane are the same as the previous work. The two antennas are placed at the top of the terminal, $w = 5$ mm above the ground plane, and occupy a 5×73 mm² area, ($h =$

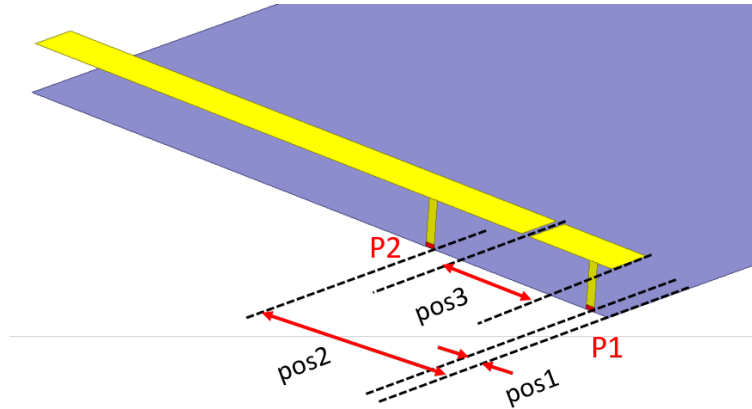


FIGURE 3.9: Optimizing parameters for double bands 2-element design.

5 mm). The gap between the two radiators in this design is however fixed 1 mm not only to take advantage of the whole volume and but also to reduce PSO tuning variables. The vertical strips are still 1 mm width. The three parameters that are mainly responsible for the system performance are

- The two excitation positions ($pos1, pos2$)
- The 1mm-gap position ($pos3$).

as shown in Figure 3.9.

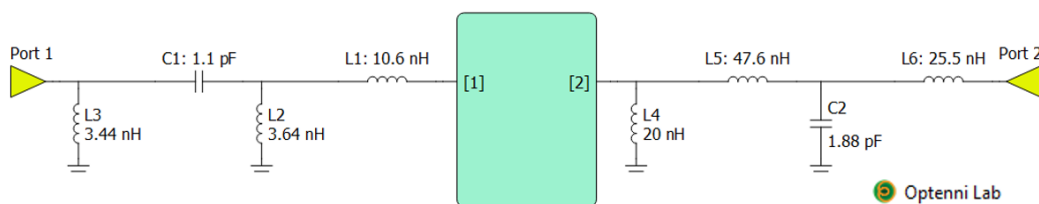


FIGURE 3.10: Corresponding optimize matching networks for the double band antennas.

In this work, two circuits comprised of 4 lumped components each are integrated into the Optenni Lab configuration to match the two ports. After the optimization, the antenna system results to be characterized by $(pos1, pos2, pos3) = (1.95 \text{ mm}, 38.20 \text{ mm}, 5.09 \text{ mm})$ and by the matching networks shown in Figure 3.10. Figure 3.11 shows the impedance matching of the two

antennas including the MN (solid lines). For the sake of comparison, the matching for the same antenna geometries without MN is reported in dashed lines. As it can be noticed, the matching is mainly due to the MN, which allows $S_{11} < -3$ dB in the bands 700 – 960 MHz and $S_{11} < -4$ dB in 1690 – 2700 MHz. As for the isolation between the two antennas, $|S_{21}|$ is lower than -39 dB all over the requested bands (Figure 3.12).

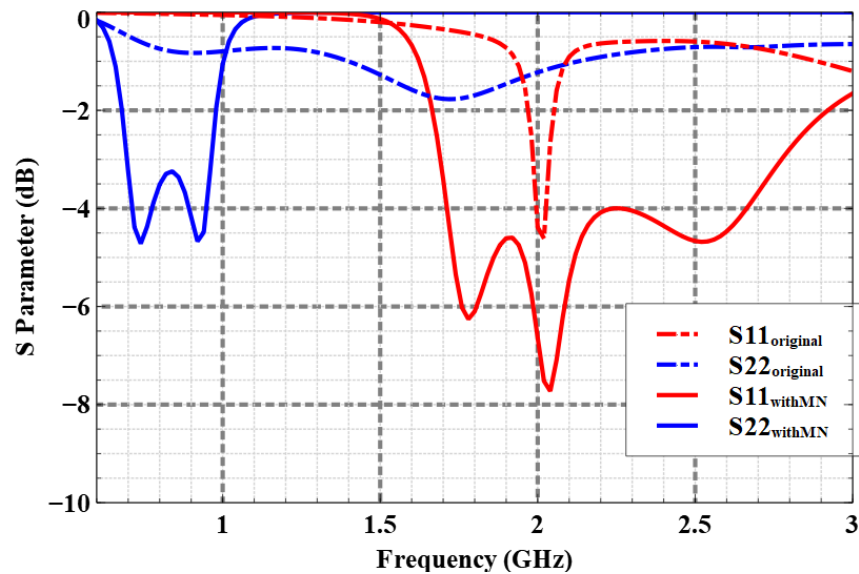


FIGURE 3.11: Impedance matching of the two antennas (with and without the MN).

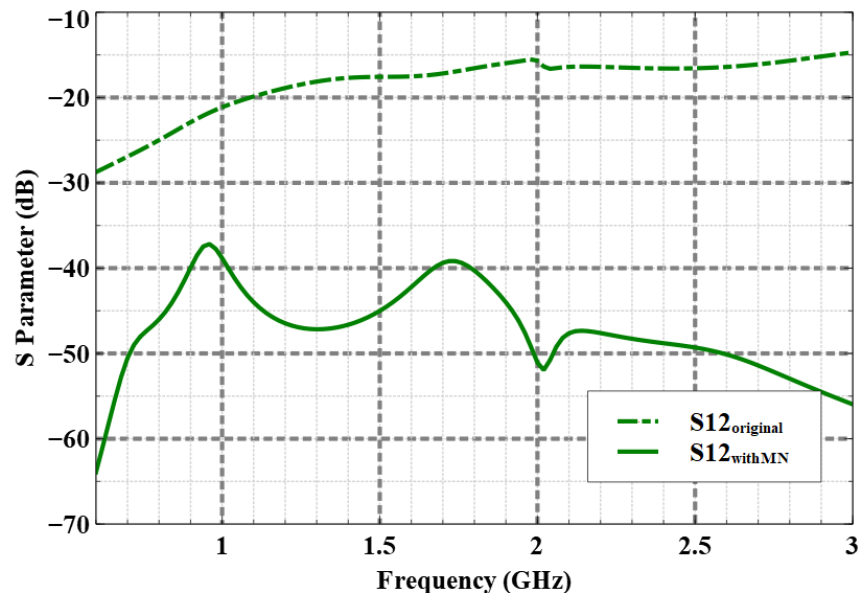


FIGURE 3.12: Isolation between the two feeding ports.

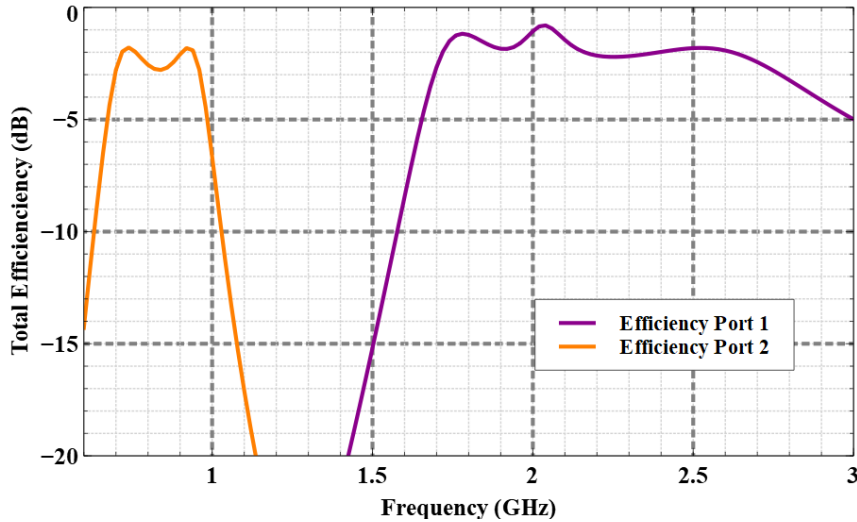


FIGURE 3.13: Total Efficiency of the two antenna systems.

The total efficiency of the two antenna systems is shown in Figure 3.13. As it can be noticed, a minimum efficiency of -2.8 dB (corresponding to 52.5%) and -2.7 dB (corresponding to 53.7%) are obtained in the lower and the higher bands, respectively.

Mobile antenna designs have to follow the specifications of the manufacturer. Usually, the number of RF ports has to be reduced as much as possible to simplify the mobile phone assembly. The two ports at the input of the two matching networks are consequently merged at the same point. In Figure 3.14, the green curve shows the impedance matching obtained in this configuration. Thanks to the high isolation level between the original ports, the $|S_{11}|$ behavior is basically a combination of the matching of the separated antenna systems. The 5 resonances as in the 2-ports model are still visible, however, the higher $|S_{11}|$ values between the resonances do not allow operation all over the requested bands.

TABLE 3.1: Components' changes (pF for capacitors and nH for inductors)

Config.	C1	C2	L1	L2	L3	L4	L5	L6
2 Ports	1.1	1.88	10.6	3.64	3.44	20	47.6	25.5
1 Port	1.1	3.16	10.5	3.66	7	21	36.4	8.8

To solve such a problem, a slight tuning of the MN components' values

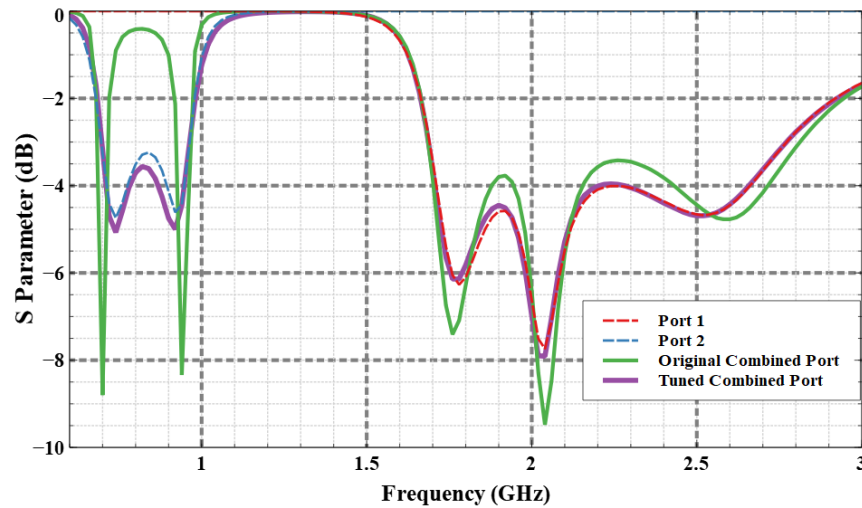


FIGURE 3.14: Impedance matching of the single port antenna system.

is therefore performed. Table 3.1 indicates the variations. As expected, the components near ports outputs (e.g., C1, L3, and L6) are the ones requiring the largest modifications. The final purple curve (Figure 3.14) totally matches the original $|S_{11}|$ in lower band and $|S_{22}|$ in higher band.

3.2.4 Triple bands 3-element antenna design

In the final work, the terminal is kept simple as before (Figure 3.5) but the antenna consists of 3 non-resonance coupling elements (NCEs). The terminal models a typical 6-inch modern mobile phone with a $73 \times 140 \times 5 \text{ mm}^3$ volume. The 3 mm wide ground clearance in one short edge is the restriction to the performance. NCEs are constructed as patches 5 mm over the ground clearance with 5 mm width and their lengths are to be optimized. The distance between every two neighbor NCE is 1 mm. Each patch is fed by a vertical strip-line of 1 mm. Again, the parameters to be optimized in this design are

- The three excitation positions (*feature1*, *feature2*, *feature3*),
- The two 1mm-gap positions (*feature4*, *feature5*).

The objective frequency bands are 690 – 960 MHz (low-band), 1.7 – 2.7 GHz (middle-band), and 3.3 – 3.8 GHz (high-band). The fitness is the output total efficiency from the MN optimizer since this reflects the effect of both impedance matching and radiation efficiency. An additional note is that the radiation efficiency for the non-resonance coupling element is very good and it can even be neglected for the sake of simple calculations.

A similar process using the PSO algorithm is integrated to automatically generate a triple band 3-coupling-element antenna. The difference is, however, it takes many more computer resources for the calculations if the 3 bands reach the same achieved matching as the double band design. Hence, the design of matching networks is simplified to a lower number of components to reduce the number of input variables feeding to Optenni Lab. The configurations of the optimization are listed as follows.

For 5 iterative parameters for PSO, 2 slot's positions to segment the patch into 3 elements, and the 3 port positions. Because the placement of the 2 slots is totally arbitrary, the 3 elements have arbitrary size. In other words, the element linked to low-band can still have the smallest area, and vice versa. The port positions are even more random, hence there are cases that multiple ports are connected to the same element. Again, the optimization stops by either total efficiency reach a threshold or a convergence of agents' movements (velocities approach zero) or reaching a maximum of 200 iterations.

For the quantity of lumped components, 3 components are used for low-band matching network, 2 components for middle-band, and 2 components for high-band, respectively. The components are selected from low-loss component families: Ceramic Johanson capacitor series R07S and Coilcraft inductor series 0402CS. It's worth note that the inductors introduce more losses than capacitors.

To event further, facilitate the optimization process, there are three filters applied to the three ports. It enhances the isolation between ports hence

simplify the task of the matching networks. In fact, this is a normal practice applied for designing most multi-band mobile antennas in the market. These additional filters can be configured in Optenni Lab. The scattering parameter of them are chosen from the Johanson Technology filters pool.

- Low-band filter that contains only low-band: 0868LP15A020E
- Low-band filter that contains middle-band and low-band: 2450LP14A100T
- Band-pass filter for high-band: 3600BP14M0600T

The optimization is run several times to assure the accountability of the optimization. The convergence of total efficiency in the best run is shown in Figure 3.15. The total efficiency escalates rapidly from 0 to 0.32 in the first ten iterations. It later tends to minimally rise around a certain level for several iterations and have a big jump. For example, the efficiency stays at around 0.37 from iteration 30th to 99th then gains 3% when reaching 100th iteration. This pattern in the convergence indicates a newfound better local best or a global best at the end. This can be seen also in the locations of the agents, like in Figure 3.19. To be precise, the 3rd parameter has an update at 100th iteration, changing from around 0.65 to around 0.4. The reset of the personal best causes the same agent's velocity, which has been more stable, varies significantly. Finally, the demonstrated optimization ends at 40% of total efficiency where positions of gaps and feeding points are shown in Figure 3.16.

After being optimized, the structure has the 3 elements arranged from high-band to middle-band to low-band along +Ox-direction. More interesting is the positions of the feeding vertical lines. It is found that the high-band element port tends to locate in the middle of the patch. The middle-band element port is necessarily being placed exactly at the edge close to the high-band element. It is possible to enhance the isolation between the middle-band and the low-band, which is the most problematic. Nevertheless, the low-band element port is rather close to the other ports, they are

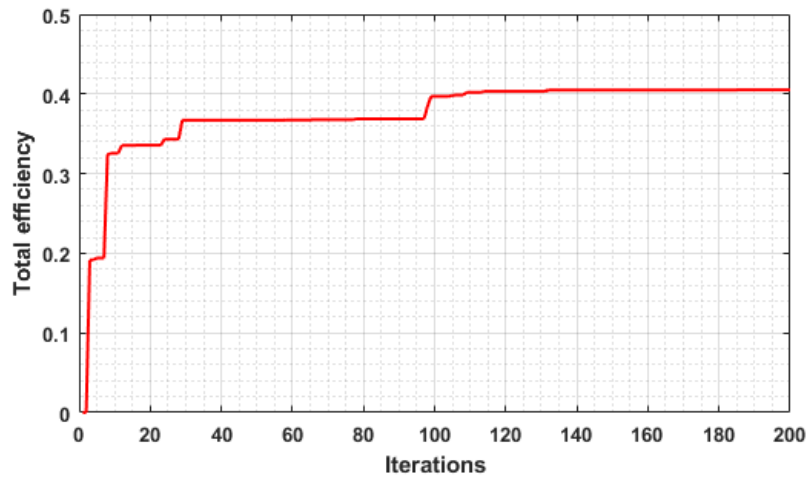


FIGURE 3.15: The convergence of total efficient in the best run of the optimization.

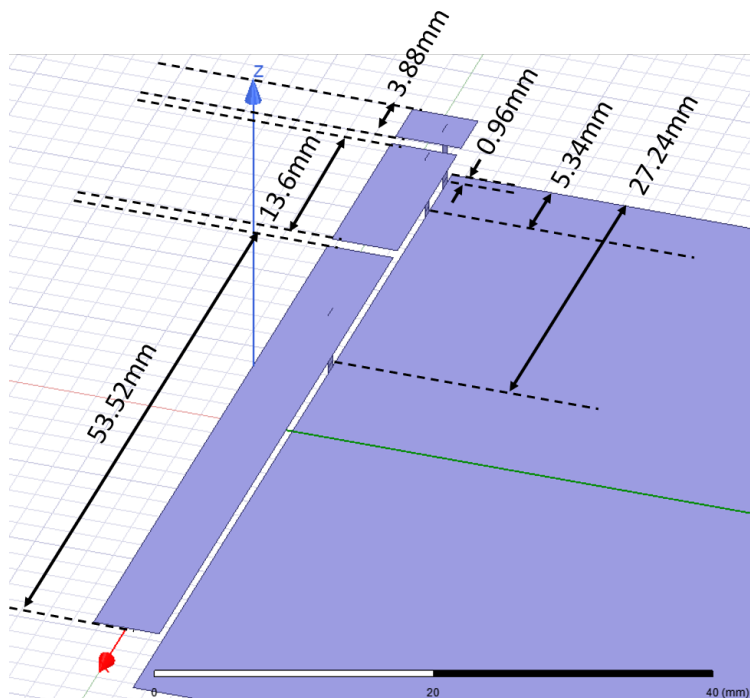


FIGURE 3.16: Final shape of the terminal with antennas after the best run of the optimization.

in the same half of the GND is equally cut along the Oy -axis. This is rather counter-intuitive to enhance isolation.

The 3 elements are matched by the 3 matching networks in Figure 3.17. The values of the components are general, except the shunt capacitor for port

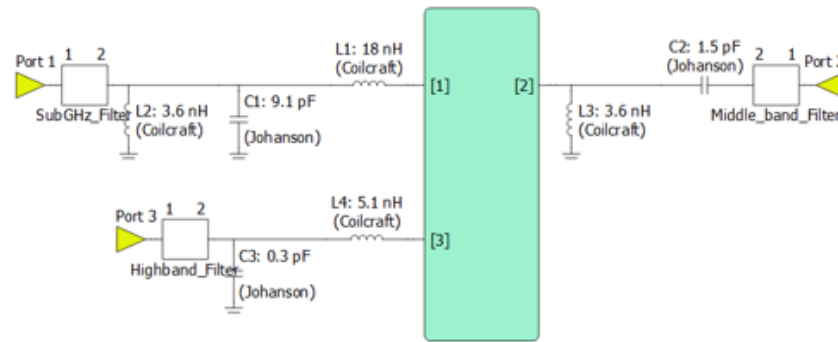


FIGURE 3.17: Corresponding optimize matching networks for the triple band antenna.

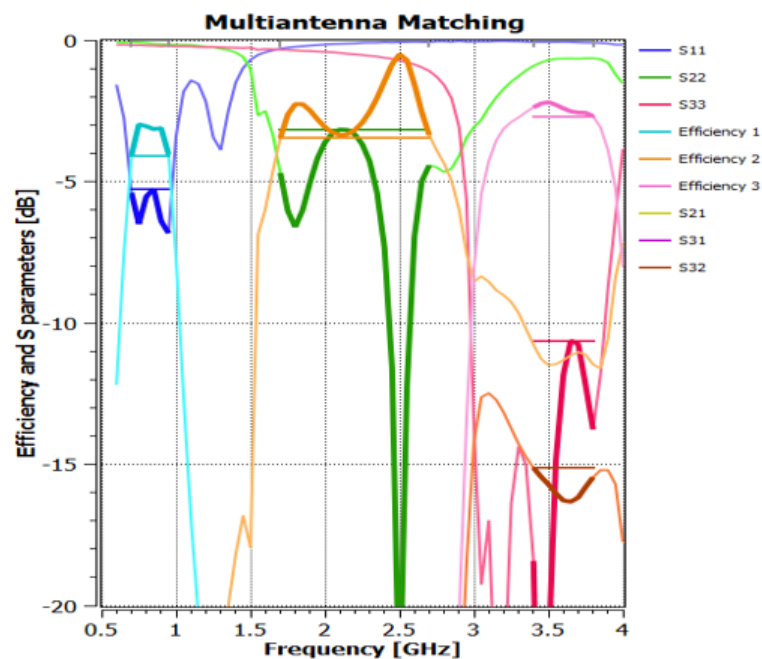


FIGURE 3.18: Efficiencies, matching of the elements and isolation between them from Optenni Lab.

3 at 0.3pF. Practically, the lower value causes higher sensibility. The placement of the filters is before the corresponding matching networks. Thank this, the isolation among the element is high. The lowest one is S_{23} which is around 15 dB. This can be explained by the proximity of the two ports.

Apparently from Figure 3.18, the total efficiencies of the triple-band are high. The minimum value is, not surprisingly, at low-band around -3.8 dB. This is the maximizing value in 3.16. Port 2 has better efficiency than port 1 even though the matching is not as good around 2 GHz. High-band is also

easy to match and has good efficiency though suffers coupling loss with port 2.

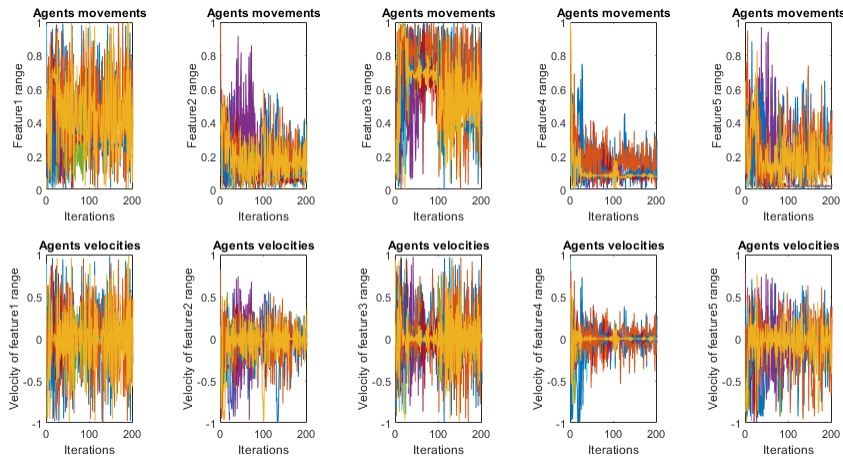


FIGURE 3.19: The corresponding agents' movement and velocities in the best run of the optimization.

Additionally, Figure 3.19 is useful to show the influences of each parameter on the final result. It seems that the more influential a parameter, the quicker it converges. In this case, parameter (feature) 1, corresponds to the position 1st gap, fluctuates the most in both location and velocity. Meanwhile, the 4th parameter, corresponds to the position of the second patch feeding strip, is easily decided in some of the first iterations, and converged quickly. The decisive position of the middle-band element port is confirmed again. In the mentioned run, the optimum is attained without a convergence for most parameters and agents. Generally, this optimization is checked not going to improve much after 100th iteration. After all, the convergence of velocities (W, C_1, C_2 in 3.2) is defined free enough so that it can check better the searching space.

Prototyping and measurements

As the output of the optimization confirms the favorable performances, the design proceeds to fabrication. However, the original design is with copper and no substrate, which is hard to realize, especially for feeding networks.

Therefore, the ground plane is changed to a PCB of 0.8 mm height with duo copper layers. The two layers are connected by numerous stitching vias. The clearance is where the copper at both sides of the PCB is removed, as in Figure 3.20. The lumped components' placements are also illustrated (with different colors) in the figure. The realization of the additional substrate and matching networks are verified in HFSS simulations. The implementation of the 3 filters is done using the HFSS Circuit feature, it provides "s2p boxes" as illustrated in the top right of the figure. At the bottom right, the matching properties are shown demonstrating a closeness to Figure 3.18.

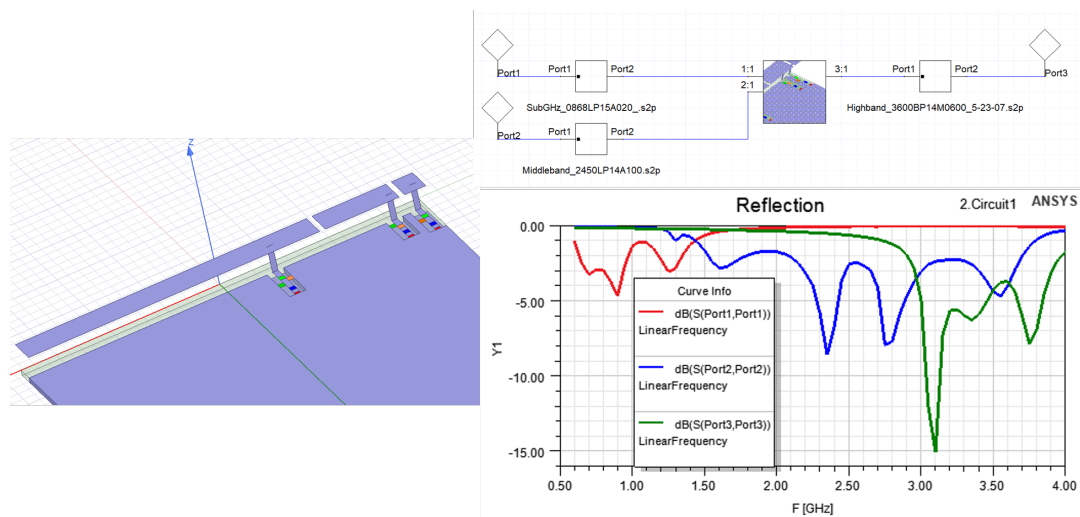


FIGURE 3.20: Simulation of triple-band design with matching networks and substrate.

The PSO algorithm is dedicated to the maximization of the total efficiency which composes the return loss and radiation efficiency. Therefore, the radiation properties of the antennas with good total efficiency should be good as well. However, it does not provide information about the radiation pattern. The patterns of the antennas are shown in Figure 3.21 in 2D and Figure 3.22 in 3D. It is clear that the pattern of the low-band and high-band antennas are almost constant over their bands. The bandwidths are narrow enough so that the antennas excite single modes on the GND. The low-band antenna has a vertical omnidirectional pattern which is the first-order mode of the

surface current on the ground. As can be seen in Figure 3.23 top left, This mode is excited along the length of the long side of the GND which is approximately $\lambda_{800MHz}/2 \approx 188$ mm, where λ is the wavelength of free-space. In contrast, the high-band antenna @3.5 GHz has a directional pattern toward $+Ox$ -direction. A high mode is seen with multiple peaks and valley in the GND. On the other hand, the middle-band antenna has very distinguishable patterns over its wide-band. The pattern is one of a second-order mode of surface currents on the GND @1.7 GHz. The currents of this mode are excited along the diagonal of the GND where its length (167 mm) is closer to $\lambda_{1.7GHz} \approx 176$ mm. Interestingly, this can be the main reason why port 2 needs to be as close to the corner as possible. The current mode gradually changes to a higher one that manifests a pattern rather directive toward $+Oy$ -direction @2.7 GHz.

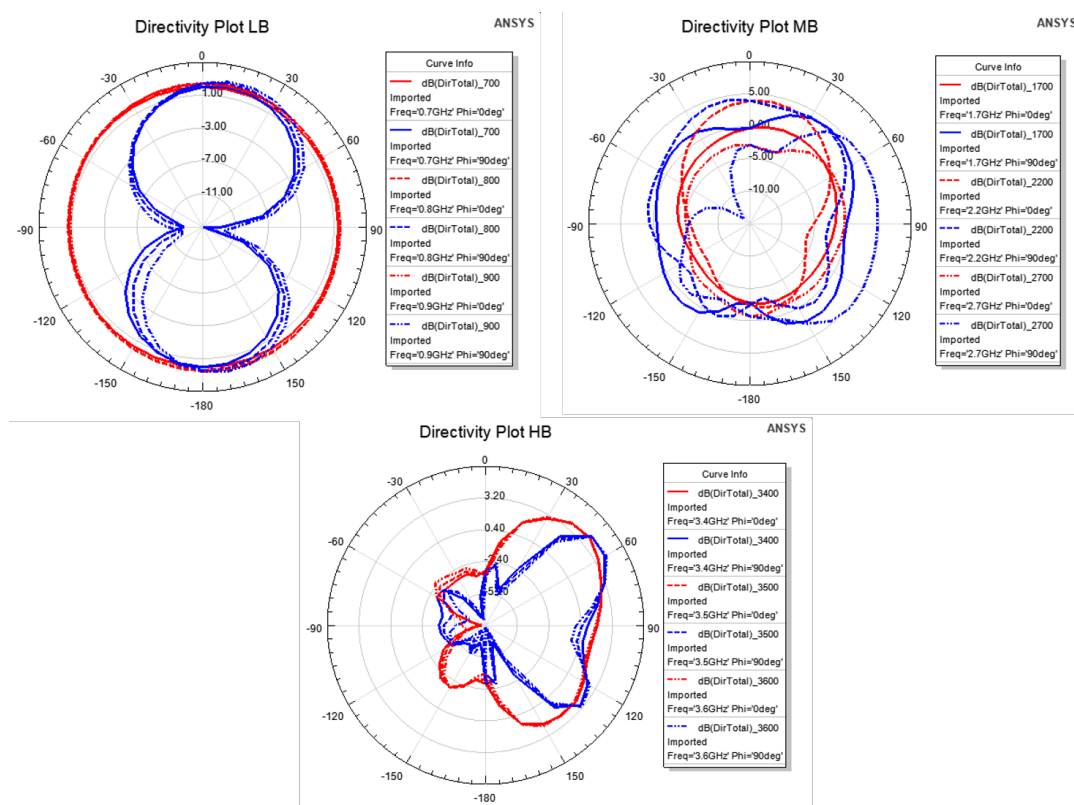


FIGURE 3.21: 2D radiation patterns of different antennas at different frequencies of their working bands.

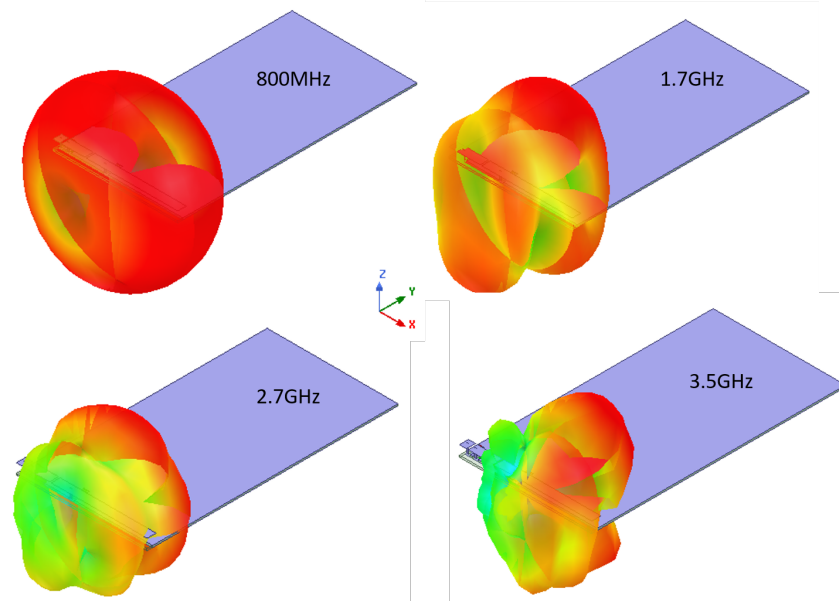


FIGURE 3.22: 3D patterns of the triple antenna system at 0.8 – 1.7 – 2.7 – 3.5GHz.

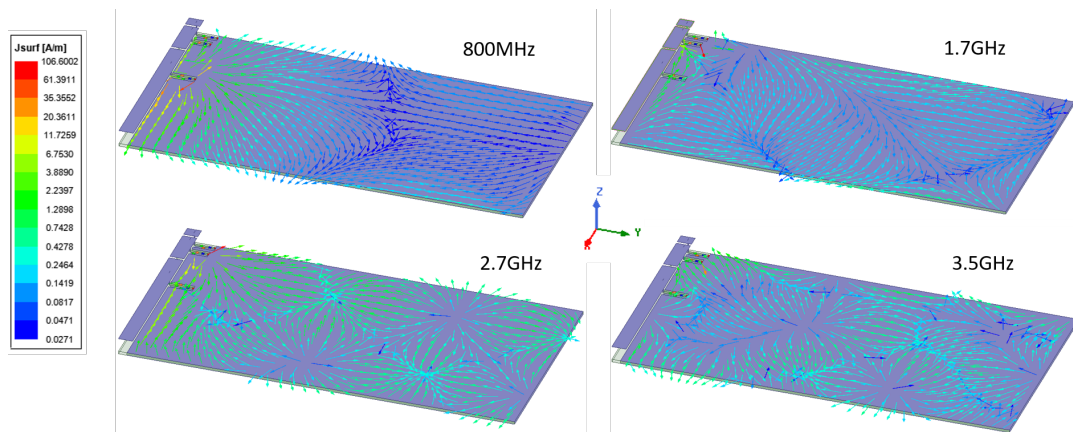


FIGURE 3.23: Surface currents on the ground plane of the terminal at 0.8 – 1.7 – 2.7 – 3.5GHz.

Finally, there are 3 coplanar waveguides (CPWGs) are tailored to feed the 3 antennas, placing themselves before the matching networks. Although the triple bands spread widely, the CPWG's width and gaps are almost unchanged over frequencies. Three other CPWGs are also placed at the unused bottom area of the GND for calibration, including an open line, a shorted (to GND) line, and a 50Ω matched line. The other sides of these three CPWGs are connected to SMA connectors. The effects of the CPWGs are expected to be removed in measurement if calibrated correctly. The final prototype is

shown in Figure 3.24.

The 3 vertical 1mm-strips and the patches are also etched on 0.4mm-thin single face substrates as in Figure 3.24 a). The vertical thin substrate is also intended to support the placement of the horizontal substrate, making sure it stays parallel with the GND. The difference in the color of the two substrates is because the patch substrate is masked leaving only three small opens to ease the soldering process.

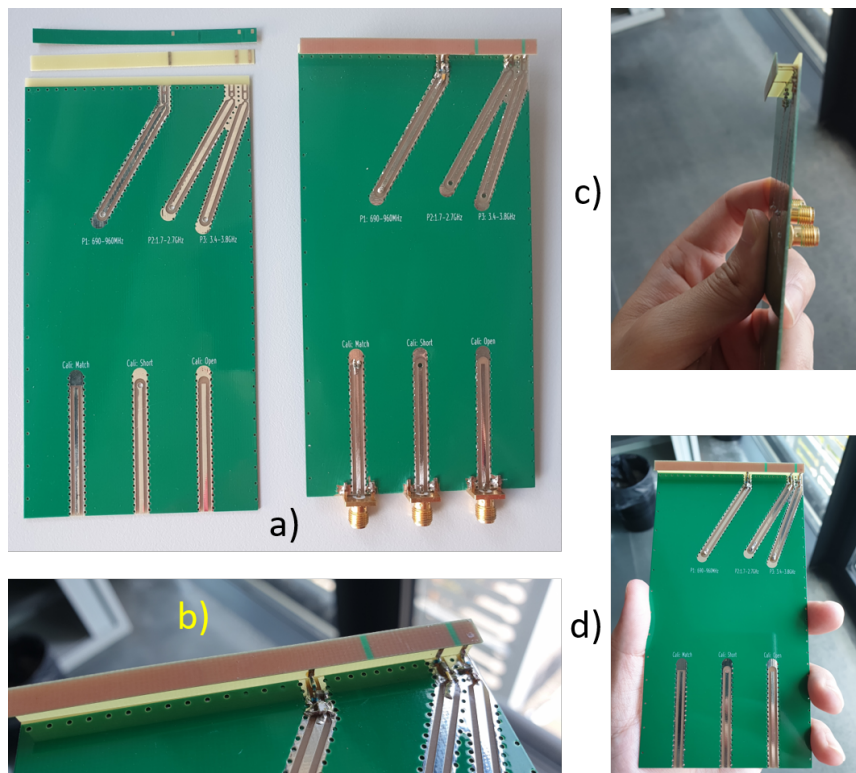


FIGURE 3.24: Prototype of the 3-antenna triple-band design. a) Different parts of the prototype before (left) and after (right) soldered together. b) Lumped matching networks and filters soldered. c) side view of the prototype, excitation ports are behind. d) Top view of the prototype with hand.

Measurements with VNA show a good agreement with the simulation in Figure 3.20. The number of experimental resonances in each band is found equally to simulations, also the level of matching. The middle band suffers high return loss from 1.7 – 2.1GHz which differs from the PSO result in Figure 3.18. Nevertheless, the coupling between antennas seems not as good as

in simulations. This might be from an imperfect manual soldering task. The isolation rises to a minimum of 11 dB.

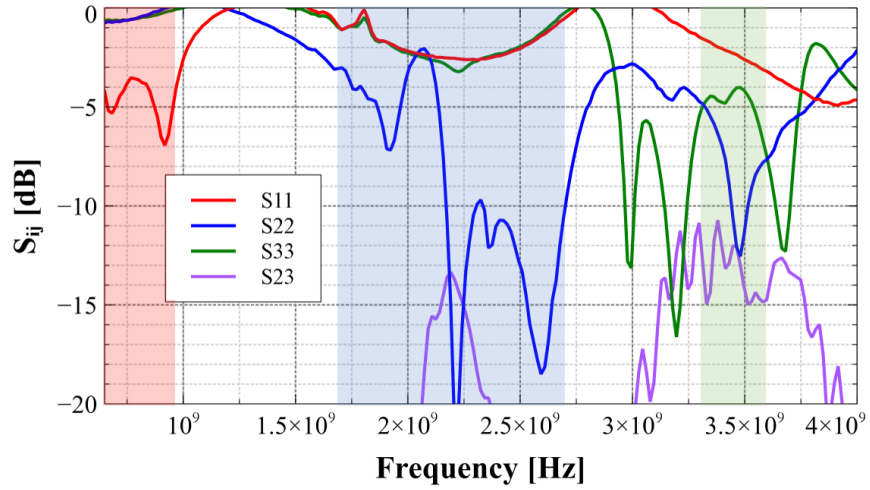


FIGURE 3.25: Experimental scattering parameter of the prototype.

The field measurements are also been done using Satimo Starlab from Orange Lab in Sophia Antipolis. Figure 3.26 shows the experimental total efficiency of different elements with different bands. The directly measured results are in thin dash lines while the solid lines show processed results without loss from the CPWGs. Apparently, the low-band antenna radiates efficiently, even though being the biggest concern from the beginning. Its total efficiency is higher than -5 dB. The middle band antenna has a considerable fall at around 2.1 GHz. This is partly because of the high reflection level mentioned. Nevertheless, the efficiency is also higher than -4 dB for a large portion of the band. Although the high band antenna has a flat efficiency level of around -6.5 dB over the band, it is 4 dB lower than expected.

3.3 Comparison and conclusion

In literature, it is still uncommon to find NCE antennas with a (very) narrow clearance. The designs in [67] perform very well for the similar triple bands, although their clearances are in order of *10-plus* mm width. Smaller

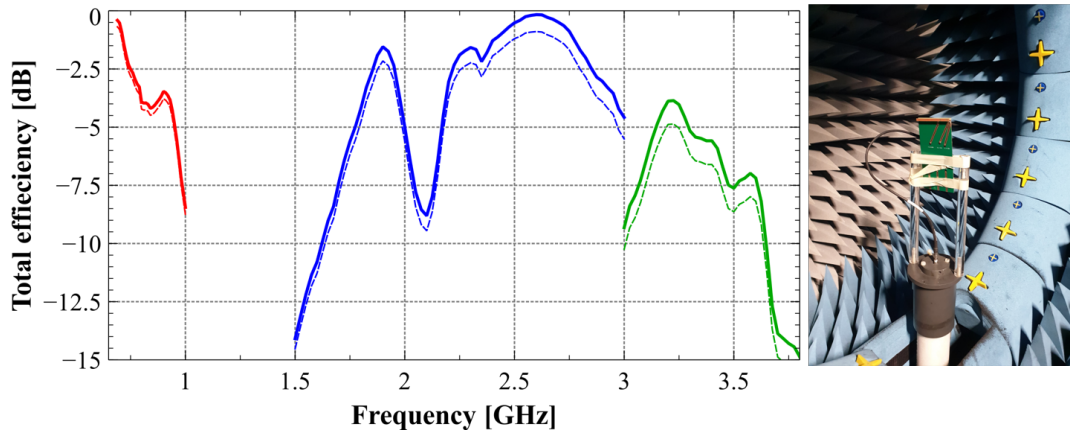


FIGURE 3.26: Field measurements with Satimo Starlab and the resulting antenna efficiency. The dash thin line and the solid lines are the results before and after correction, respectively.

TABLE 3.2: Comparison with state of the art designs. Dimensions are in millimeter.

Ref	Design strategy	Terminal dimen.	Clearance dimen.	Antenna dimen.	Lowband eff.	Midband eff.	Highband eff.
[49]	Reconfigurability	146.8x71.2			< 36%	< 55%	< 66%
[47]	Metal rim, reconfigurability	150x74	2		40 – 90%	40 – 90%	60 – 75%
[48]	Metal rim	130x70x5	70x10x5		65%-91%	> 65%	> 65%
[65]	Analysis of wavelength modes of monopole antenna, MN	140x80	8x80	8x80x5.8	64 – 95%	50 – 73%	
[45]	Multi-hand element with parasitic elements	70x128	8x70	8x70x5.8	51 – 87%	64 – 83%	
[66]	MN, loop antenna	75x145	75x10	10x5x75	> 30%	> 59%	> 59%
[67]	Capacitive coupling element, MN	50x115	15x50		50 – 76%	60 – 85%	56 – 89%
[68]	Multi-elements, capacitive coupling element	80x160	7mm short edge, 5mm long edge		> 80%	60 – 99%	
–	Proposed design	73x145	73x3	73x5x5	> 40%	16 – 90%	18 – 40%

clearances can be found in [45], [68], though the authors do not address the 3.3 – 3.7 GHz band. The tailoring of the metal frame is giving the best performance in terms of efficiency for small clearance. In [49], the efficiency is higher than 40% for the triple bands. Reconfigurable mechanisms work well also in [49] though the performance is relatively lower than the previous methods. In comparison, the proposed design uses NCEs and for a very

narrow clearance, 3 mm. It has shown its effectiveness in addressing the low-band with an efficiency higher than 40%. Unfortunately, the middle-band element has a big jump at around 2.1 GHz. Nevertheless, other frequencies within the band have higher than -3 dB efficiency which is comparable with most cited works. The high-band element is also problematic, though it is believed to be a technical problem from the manual task. Hopefully, it can be corrected.

When it comes to the PSO, the developments of different testing optimizations in this work, each being more complicated than the previous one, show the agility and the flexibility of the methodology. Its effectiveness is also demonstrated in every work to tackle the narrow-clearance problem in modern mobile phone. The prospect of the algorithm is conceivable. It can be further developed to optimize for a more complex system of the antenna at both top and bottom of the terminal. The *fitness* function can be altered to check also radiation properties to make sure the antennas have a low correlation. It is foreseen also being used to optimize the metal frame modifications as this part proves a superior radiator to NCEs.

Chapter 4

Antenna designs and measurements at mmWave

4.1 Design and measurement concerns

4.1.1 Generals

In the 5th generation of the mobile communication system (5G), things are updated to a higher level of complexity and integration. Especially in the RF front-end system, the quantity of antenna array elements are skyrocketed, giving the term Massive Multiple Input Multiple Output (Massive MIMO) [15]. Likewise, the disruptive data rate and latency are provided by the introduction of Millimeter-Wave (mmWave) communication. The connector-to-connector paradigm which led telecommunication development during the last 20 years, gradually becomes less applicable. Therefore, Antenna in Package (AiP) or Antenna on Chip (AoC) become an unavoidable design trends [69]. That means the integrated RF front-end architectures now should be linked permanently to the antenna instead of being removable with the connector-to-connector mechanism. Normally, the antenna is built on the top side of the Printed-Circuit-Board (PCB), meanwhile, phase-shifters, amplifiers together with matching and control networks are etched to the other side or in the middle layers of the PCB. Losses are expensive for multilayer

circuits, due to the surface-waves and the dielectric loss tangent. On one hand, return currents must be taken care of seriously. On the other hand, the substrates must be chosen with a low loss property, like PTFE, Fiber Glass, Ceramic, etc. FR4-Epoxy or PrePregs which are popular at lower frequency cause design obstacles at mmWave. An example of a PCB stackup in Figure 4.4 is taken from the manufacturer website. Included in the middle of the stackup is a PrePreg2116 layer with $\tan\delta = 0.025$ at 10 GHz, where $\tan\delta$ denotes loss tangent, and of 0.48 mm thickness. How to compromise this substrate loss is a real challenge for any antenna/RF circuit designer.

4.1.2 Antenna array architectures for 5G mmWave

Massive MIMO is a key feature in the 5G system. Array antenna will be designed and built in large quantities, from 64 to 256 elements for gNB. Multiple antenna theory or array antenna is developed to enhance the radiation gain of the system against propagation loss at high frequencies. It also provides special multiplexing and interference suppression.

$$P_r = P_t G_t \frac{1}{4\pi R^2} A_e p_i \quad (4.1)$$

where P_r and P_t are received and transmitted powers, respectively, G_t in transmitter's gain, R is the distance between transmitter and receiver, and p_i is the polarization factor.

From the equation, if antenna size is downscaled with wavelength while increasing frequency, there is an attenuation increase in the order of square. However, if one side of the communication chain keeps the same aperture size, A_e as at lower frequency, the performance is actually preserved. With both sides having the same aperture sizes, the performance is better compared with lower frequency.

In addition, the mutual coupling is another important parameter when implementing Massive MIMO. It is defined as

$$S_{ij} = \left. \frac{b_i}{a_j} \right|_{a_k=0 \text{ for } k \neq j} \quad (4.2)$$

where a_j and b_i are complex value of input voltage to port j and output voltage to port i . S_{ij} is calculated in the condition that all ports other than port j are matched. An array of N elements, the scattering parameters are presented as a matrix.

$$\begin{bmatrix} b_1 \\ b_2 \\ \dots \\ b_N \end{bmatrix} = \begin{bmatrix} S_{11} & S_{12} & \dots & S_{1N} \\ S_{21} & S_{22} & \dots & S_{2N} \\ \dots & \dots & \dots & \dots \\ S_{N1} & S_{N2} & \dots & S_{NN} \end{bmatrix} \begin{bmatrix} a_1 \\ a_2 \\ \dots \\ a_N \end{bmatrix} \quad (4.3)$$

Mutual coupling is expected very low, especially for a full-duplex system at gNB, it is required below -30 dB. At UE, however, it is hard to achieve such a level. A 20 dB in isolation among ports can be considered good. In those cases, S_{ij} are neglectful and the scattering matrix is a diagonal matrix.

5G NR transmission requires implementing precoding. It is manipulating the element's amplitude and phase to achieve the above-mentioned tasks: special multiplexing or interference suppression. For multi-users cases, beamforming helps to maximize the gain toward designated users while minimizing the signal transfer to any adjacent ones. For line-of-sight scenarios, the channel is fully correlated with no multipath propagation, beam-steering is applied to maximize the gain toward a single user, achieving an additional $G_{arr_{RX}} \times G_{arr_{TX}}$ where $G_{arr_{RX}}$ and $G_{arr_{TX}}$ are array gain for receiver and transmitter sides, respectively. However, the most common scenarios that happen in communications are NLoS with multipath. The fast fading effect in this case causes the superposition of multiple plane waves.

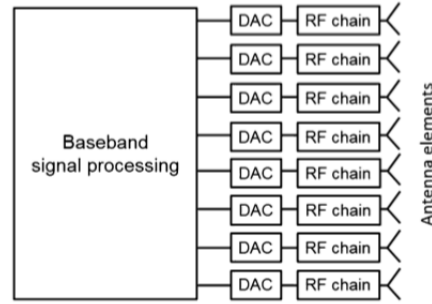


FIGURE 4.1: Full digital array architecture.

At the receiver, the decoder functions optimally when the channel properties, normally translated as a matrix, is well-known. Otherwise, the array gains at Tx and Rx contribute a maximum $(\sqrt{N_T} + \sqrt{N_R})^2$ gain, where N_T and N_R are numbers of elements in transmission and reception, respectively.

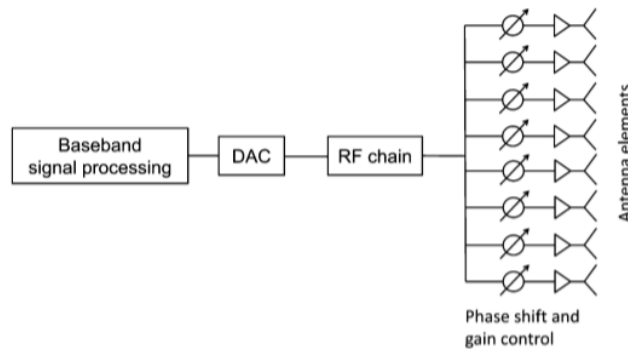


FIGURE 4.2: Full analog array architecture.

There are different antenna array architectures for Massive MIMO, each with its own pros and cons. In a fully digital architecture, each element is equipped with its own RF chain and analog-to-digital converter for Rx and digital-to-analog converter. This architecture achieves the best flexibility and performance. Former communication systems have relatively narrow bandwidths, which require a slow sampling rate for the converters. This simplicity allows low-frequency systems using only digital architecture. However, 5G NR, especially at FR2, will provide relatively large channel bandwidth up to 400MHz. Consequently, a high sampling rate is needed, leading to very high-power consumption. An analog or hybrid solution is reached to tackle the problem.

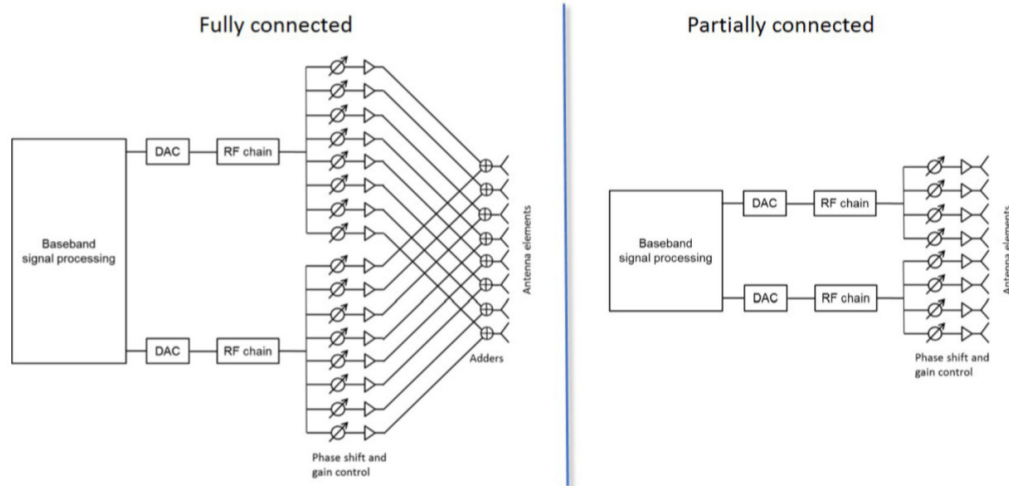


FIGURE 4.3: Fully connected hybrid array architecture (left) and partially connected hybrid array architecture (right).

A fully analog architecture is where all antenna elements are connected to the same converter and RF chain. An additional controllable phase-shifter before each element is used to beamforming. An amplifier/attenuator can also be added to achieve better interference suppression, for example, for the Zero-Forcing precoding scheme. Due to the single RF chain integrated, only TDD is allowed for a fully analog architecture. Although the performance is not comparable to a fully digital one, this architecture can be more useful when the small cells feature is applied in 5G.

Hybrid array architecture is mixing the feature of the previously described ones, hence mixing their advantages and disadvantages. The number of RF chains and ADC/DAC is reduced while all antenna elements can be connected to the same chains, as for a full hybrid system, or separated into sub-arrays, as for a partly hybrid system. The performance of digital architecture and the cost and low complexity of an analog architecture are to be optimized.

A fully hybrid architecture requires higher complexity than a partly one due to the introduction of adders. Therefore, more of the second case is studied in literature [70], [71].

Overall, Massive MIMO with any architecture will improve performances of 5G mmWave and distinguish it from the precedent cellular systems. In the scope of project MASS-START, we certainly aim also at similar objective performances. Toward this end, the utilized antenna array designs need to be well studied so that it can be customized adapting to the system as a whole.

4.2 Broadside antenna designs at mmWave

Considering the previous analysis, this section provides some insights into the antenna design process applied to achieve the following specifications.

- *Frequency band*: 5G NR n258
- *Bandwidth*: 24.25GHz - 27.5GHz (12.6% potential bandwidth)
- *Impedance matching*: $S_{ii} < -10dB$
- *Isolation among ports in array*: $S_{ij} < -20dB$
- *Radiation pattern type*: Directive, broadside
- *Half-power beamwidth*: $> 40^\circ$
- *Element gain*: $> 5dBi$
- *Number of elements in array*: 4-8-16
- *Gain total (element gain + array gain)*: depend on number of elements

The choice of the fabrication stack-up and the antenna geometry is presented in the first part. Then a complete analysis of how to take advantage of the technology and precedent studies to improve antenna performances are considered in a second step. Some food-for-thought is given showing the experiences that an antenna engineer/designer might meet during the design process.

4.2.1 Design properties and choices of feeding networks

As being discussed previously, the PCB technology is preferred because it is easily accessible and inexpensive nowadays. A PCB stack-up is taken from Eurocircuits [72], constituted by four copper layers and three substrate layers, as illustrated in Figure 4.4. All copper layers have $h = 18\mu\text{m}$ thick. The substrates' materials are RO4350 - PrePreg2116 - RO4350, with $\epsilon_r = 3.66 - 3.96 - 3.66$, respectively from either side to the other, where ϵ_r denotes the relative permittivity constant. The substrates are 0.254 mm - 0.48 mm - 0.254 mm high, respectively from either side to the other. It is noted that there is rarely a 3-layer PCB standard, stack-ups come with 1 – 2 – 4 – 6 and a higher even quantity of layers. Finally, the chosen stack-up is pool-able as the time the designs are made and its price is acceptable for the project's budget. Figure 4.4 also shows additional air and conductive layers that will be introduced shortly.

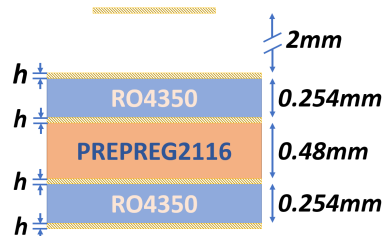


FIGURE 4.4: 4-layer PCB stack-up example.

Defined by Eurocircuits stack-up as in Figure 4.5, A and C are two types of a blind via, which can see from outside a PCB. It can be plated either before (like A) or after (like C) pressing the multilayer. The buried via, on the other hand, cannot be seen from outside. It needs to be plated before the pressing. One important point when one wants to integrate blind or buried vias is the pooling condition from the manufacturer. The price of the PCB can go triple or more simply because those addition vias and the demand of the same stack-up is scarce at the given moment.

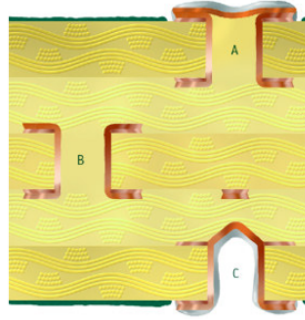


FIGURE 4.5: Blind via (A,C) and buried via (B) from Eurocircuits website.

A quick look at the research literature and the market shows that many academic studies and industrial products propose recently some compact integration gathering antenna and RF front-end circuitry [73]–[77]. In these designs, multiple-layer PCBs have been utilized for both the feeding network and control network. The antenna designs in most cases are planar patches, which are simple and fundamentally well-understood. This is a nice suggestion as the patch antenna gives a directive pattern.

A patch antenna is categorized as a microstrip antenna because of its close properties to the ones of the microstrip line. Using this type of antenna is advantageous in terms of low-profile, ease in fabrication and tuning for better frequency bands, bandwidth, and polarization (linear or circular). Some drawbacks of microstrip antennas, in general, are inherent narrow bandwidth, low power handling, and high ohmic loss.

To tune a rectangular patch antenna, for example (other patch shapes have similar properties), changing the patch resonance length L is the direct method, as the resonance frequency f_0 of a rectangular patch antenna can be approximated as the following function of L .

$$f_0 = \frac{c}{2(L+h)\sqrt{\epsilon_e}} \quad (4.4)$$

where c is the speed of light, h is the substrate height and ϵ_e is calculated by

$$f_0 = \frac{\epsilon_r + 1}{2} + \frac{\epsilon_r - 1}{2} \left(1 + \frac{12h}{w}\right)^{-1/2} \quad (4.5)$$

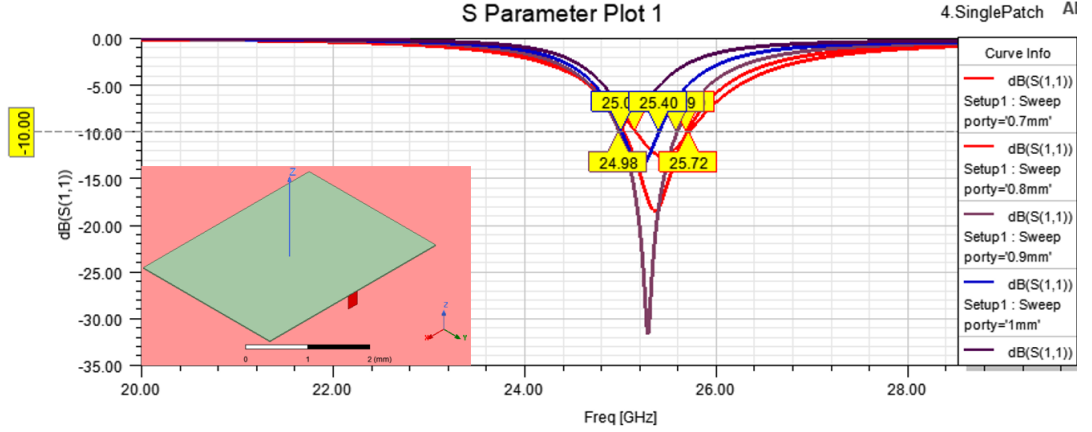


FIGURE 4.6: Reflection coefficient of single patch structure for different feeding position

where w is patch non-resonant width and ϵ_r the relative dielectric constant. It can be seen also that changing the height of the substrate helps in tuning the resonant frequency. However, one should be careful that a higher substrate means higher dielectric loss. In addition, there are only a handful of substrate's height standards. Using substrates with high relative dielectric constant ϵ_r is an easy approach to achieve certain compactness, i.e. a smaller size patch. Nevertheless, this property has discrete values regarding all available materials and they are not all accessible.

Derived from equation 4.5, we can approximate the half-wavelength length of the patch.

$$L = \frac{c}{2f_0\sqrt{\epsilon_e}} - 0.824h \frac{(\epsilon_e + 0.3)\left(\frac{w}{h} + 0.264\right)}{(\epsilon_e - 0.258)\left(\frac{w}{h} + 0.8\right)} \quad (4.6)$$

with

$$w = \frac{c}{2f_0\sqrt{\frac{\epsilon_r + 1}{2}}} \quad (4.7)$$

From this equation, the half-wavelength length and the non-resonance width of the patch are calculated 2.9 mm and 3.8mm, respectively, at 26 GHz. As a personal note, although one can use various numerical tools to get those values without knowing the mentioned equations, a good understanding of those helps engineers/designers better analyze the parameters of their designs. It should be noted, firstly, that only the parameters (height= 0.254 mm and $\epsilon_r = 3.66$) outer layer where the patch is etched are taken. The inner substrate or the last substrate on the other side is unlikely to have any effect on the resonance. Secondly, L and w are foreseen being tuned by simulations to have the same length so that a dual-polarization solution can be developed later.

The biggest concern when using a patch antenna is usually the narrow bandwidth. A patch antenna is simulated using the HFSS EM tool with the sizes calculated previously in Figure 4.6. The excitation position is being optimized to obtain the best impedance matching and largest bandwidth. Certainly, the best matching cannot cover more than 800MHz bandwidth with -10 dB reflection criteria, i.e. no more than 3.1% relative bandwidth. This problem, however, has been studied thoroughly in literature and several techniques to enhance the bandwidth have been proposed. The most common one is using parasitic elements to create some adjacent resonances to the first one. These elements can be added horizontally [78], [79] or vertically [80], [81] to the first patch. The latter is also called a stacked patch. Using the aperture-coupled patch antenna is another method [82], [83]. Overall, the principal to enhance the bandwidth is to trade the compactness off. In this work, stacked patch and aperture-coupled techniques are to be used to enhance the bandwidth.

When it comes to feeding techniques, there are basically four types for patch antennas, including microstrip line, proximity coupled feed, probe feeding, and aperture-coupled feed [84]. The first option requires the whole,

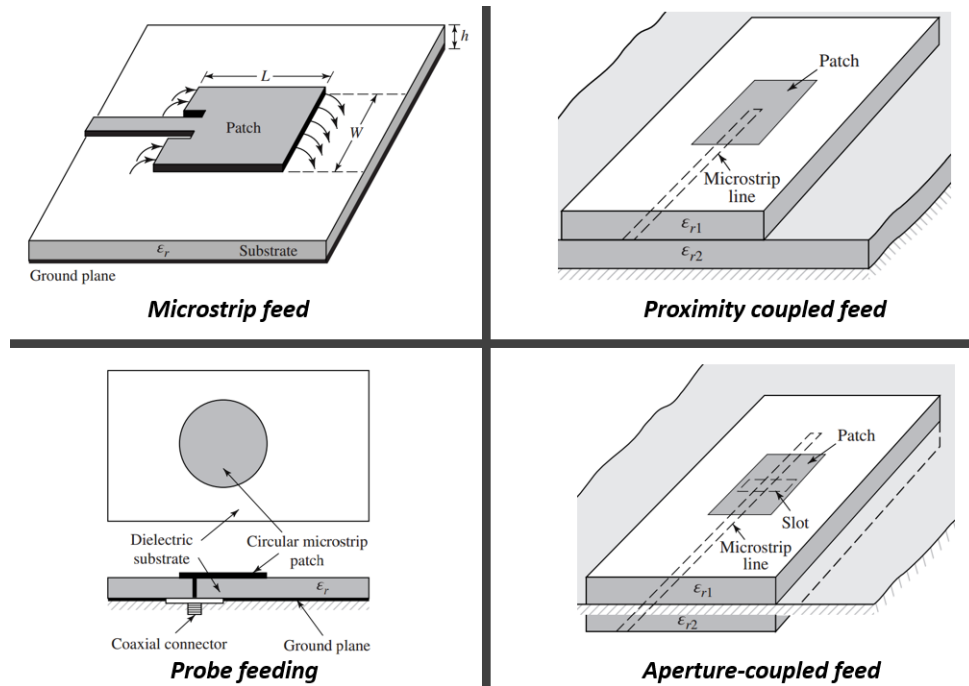


FIGURE 4.7: Different excitation types for patch antenna (courtesy of Balanis' book).

or at least a portion of, the TM line in the same plane as the patch. Tuning can be done easily with the cut at the TM line end. However, it is less preferable due to spatial constraints in a 2D array. The proximity coupled feed takes advantage of the coupling between a TM line and a patch on two sides of a substrate. To assure a high mutual coupling, the height of the intermediate substrate is limited. This second option might require blind/buried vias to connect the TM line to the closest conductive layer to the patch. Blind vias can be used, but the microstrip line will be on the PrePreg dielectric layer, and it would be inefficient. These two solutions to enhance bandwidth are, therefore, omitted for further studies.

Probe feeding in PCB, equally as direct excitation using via, is a straight forward method. Such a feeding mechanism has some advantages such as simplicity in implementing dual polarization. However, the structure of direct via connecting TM line and antenna in high substrate and multilayer introduces a high inductance to the impedance. In comparison with direct feed, aperture (slot) coupling is better in saving PCB real estate [85]. This

feature is really preferable for complex networks and especially needed for heat dissipating. The conventional designs of aperture coupling have a TM line in the second closest conductive layer to the patch, an aperture placed between that TM line and a patch. In that case, a blind via might still be required. With the chosen PCB stack-up, multiple slots are foreseen integrated into the design. Such design with TM line feeding a patch through multiple apertures has not been seen reported.

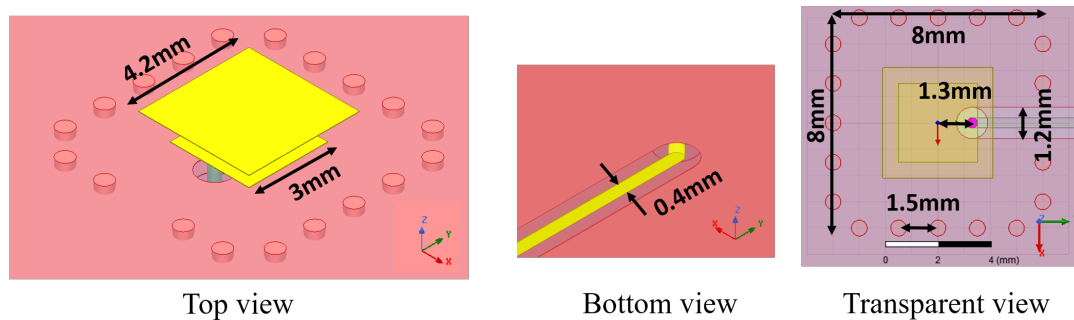


FIGURE 4.8: Parameters of via feeding design.

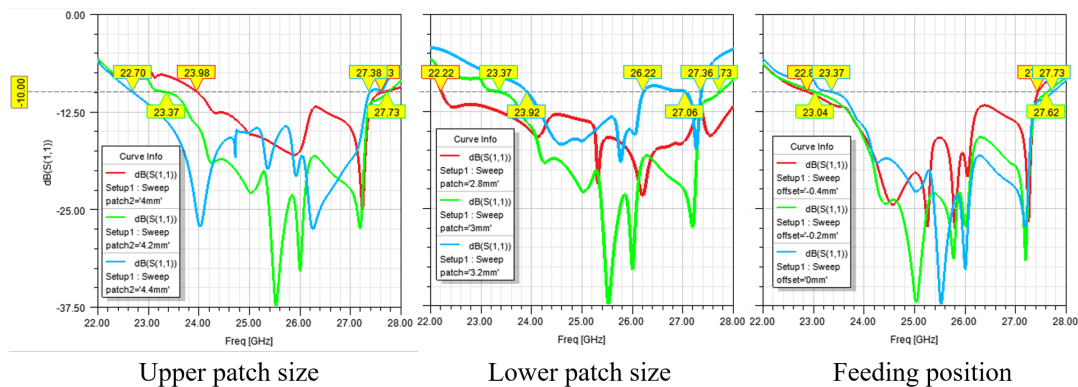


FIGURE 4.9: Parametric studies for via feeding design.

In this regard, the latter two feeding mechanisms need to be evaluated with a discussion on bandwidth enhancement techniques. In the via feeding design, a coplanar waveguide with the ground (CPWG) is designed with a 0.4mm line width and 0.4mm gap. It excites the RF signals from the bottom layer through a 0.4 mm diameter via. There are two 0.6mm-radius open circles in the two middle conductive layers to avoid the feeding via from

short-circuited problem. The main patch is $3.0 \times 3.0 \text{ mm}^2$ and etched to the top conductive layer. The feeding center is offsets 1.3mm to give the best matching. To enlarge the impedance bandwidth, a second stacked patch is added above the first patch, distancing 1.6 mm by air. The sizes of this second patch is $4.2 \times 4.2 \text{ mm}^2$. A cavity made of via is introduced to connect all ground layers (second to bottom layer), ensuring a good return current. The vias' diameter is 0.6 mm and the distance between every two neighbor vias is 1.5 mm. The cavity's size, from the center to center of the vias, is 8 mm, which equals $0.7\lambda_0$, where λ_0 denotes the wavelength in free-space at 26 GHz. The details of the antenna are shown in Figure 4.8. It is noted that the vias do not need to be that close to the antenna to achieve optimal performances. The size and the distance of vias in the cavity are optimized to block the surface currents that happen in array designs. Details of the effects will be illustrated in Chapter 5.

All of those mentioned parameters are optimized in HFSS simulations. In this design, the three most important parameters are the lower (small) patch's and upper (big) patch's sizes and the feeding position. A parametric study has been done to evaluate these parameters. From Figure 4.9, it can be seen that the big patch has high tolerance in terms of impedance matching within a range of 4 – 4.4 mm. The small patch is rather sensitive. It can be rectangular with its size in the range of 2.8 – 3.2 mm. Outside this ranges, the antenna risks not covering band n258. The optimal feeding position is very close to the edge of the first patch. Moving toward the center, the matching is gradually reduced. With these parameters taking values as mentioned, the impedance matching is optimal, $S_{11} < -15\text{dB}$.

The aperture-coupled structure is much more complex and requires more optimizations, as illustrated in Figure 4.10. Concretely, a CPWG is again designed to excite the slots from the bottom layer. In this design, it has a 0.5 mm line width and a 0.75 mm gap. The end of this CPWG and the open area

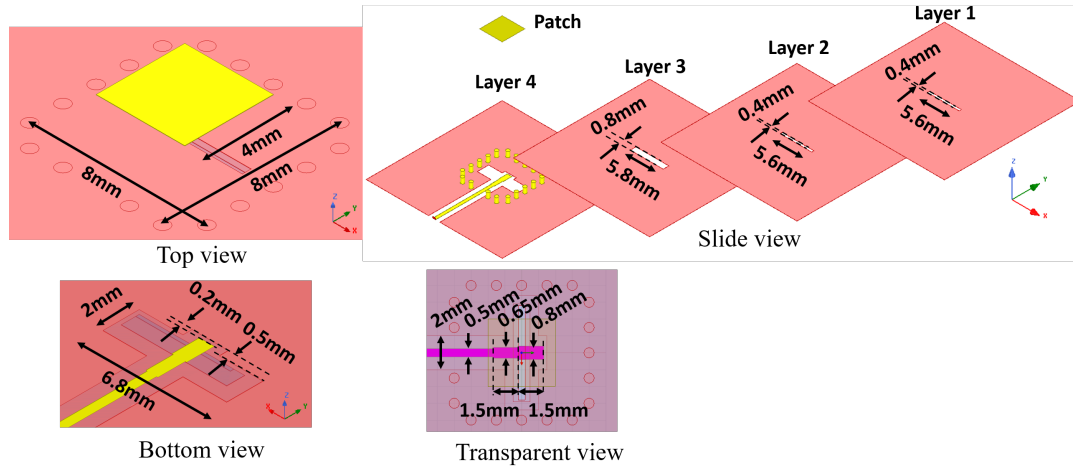


FIGURE 4.10: Parameters of aperture coupled design.

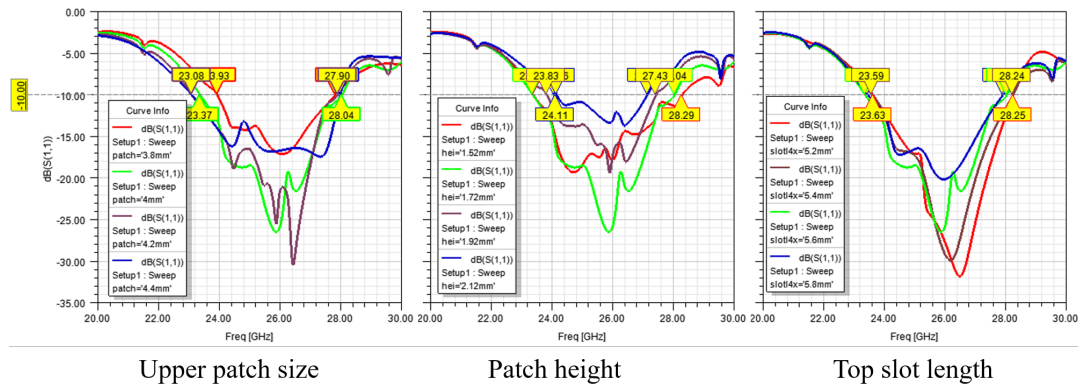


FIGURE 4.11: Parametric studies for aperture coupled design.

in layer 4 are carefully tailored to give the best impedance matching. The CPWG end-point has a step-like geometry constituted by 3 parts the sizes $0.8 \times 1.5 \text{ mm}^2$ - $0.65 \times 1.5 \text{ mm}^2$ - $0.5 \times \text{coplanar-length} \text{ mm}^2$, further away from the end of the line. The tapering of the opening on the bottom layer is shown in the figure leaving minimum copper loss in fabrication while matching is maintained. Three slots, i.e. apertures, along x -axis are then etched to the second-lowest copper layer to the top copper layer to couple the signal from the bottom layer to the top. Their corresponding sizes are $5.8 \times 1.0 \text{ mm}^2$ - $5.6 \times 0.4 \text{ mm}^2$ - $5.6 \times 0.4 \text{ mm}^2$, respectively. It is found that a hanging patch over the air coupling with a slot radiates better than a coupling patch in the top conductive layer. Therefore, a $4 \times 4 \text{ mm}^2$ coupling patch is placed over the top slot, distancing 1.6 mm by air. The slots center is 1.3mm offset from

the patch center in the Oy -axis. The same via cavity is also used in this design with also an isolation-enhancement purpose as the previous design.

Likewise, parametric studies are done also to optimize the design. In this case, the coupling patch should take value around 4 – 4.2 mm, outside this range the impedance matching worsens. The top slot in this design functions similarly to the lower patch via direct feeding design. It has a tuning effect on the working frequency, however, its tolerance is better as it can be within 5.2 – 6 mm. The height of the hanging patch is at best around 1.6 mm as mentioned. Being far from this value, the matching gradually decreases.

It is worth mentioning that those high tolerances in the two designs are extremely useful in the fabrication process. The tolerances will ease the fabrication uncertainties, should there be any.

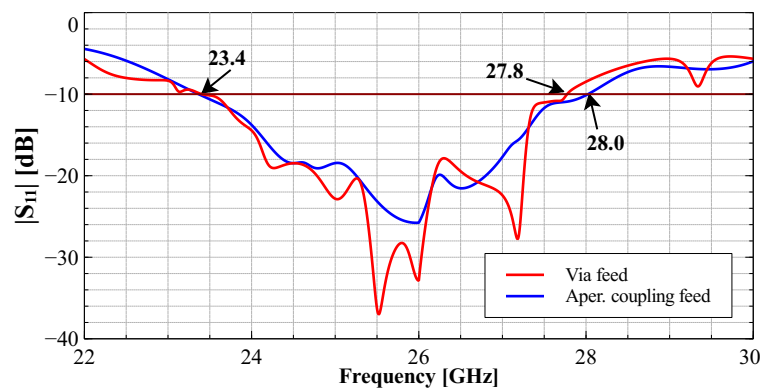


FIGURE 4.12: Reflection coefficients in two designs.

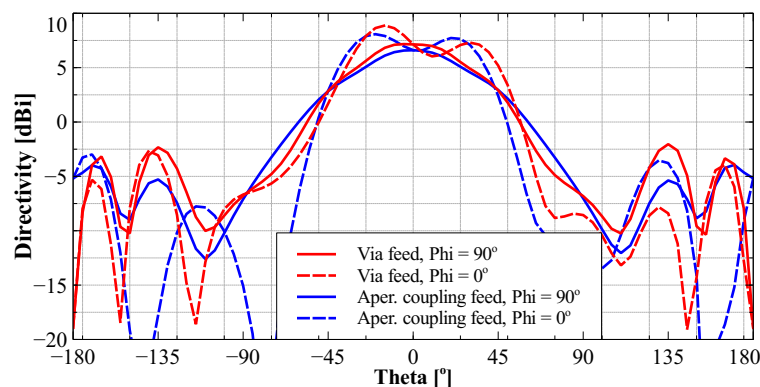


FIGURE 4.13: Directivity patterns of two designs in xOz (solid lines) and yOx (dash lines) planes.

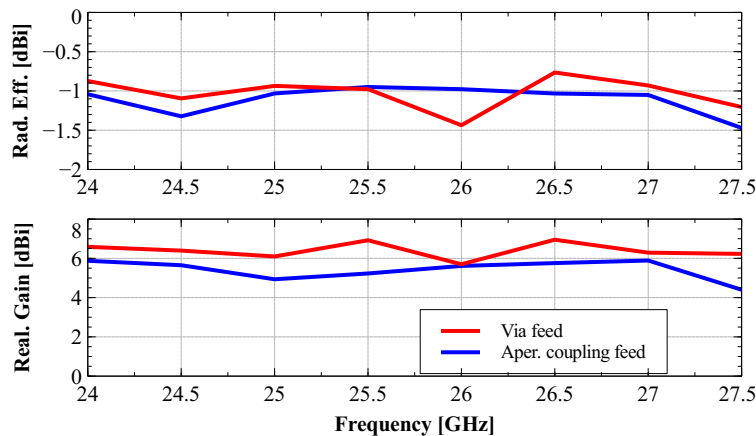


FIGURE 4.14: Simulated radiation efficiencies and realized gain at $\theta = 0^\circ, \phi = 0^\circ$ in two designs.

Overall, the optimal designs yield comparable performances. See Figure 4.12 shows that the two designs can cover from 23.4 GHz to around 28 GHz, hence covering n258. The impedance matching level via direct feeding antenna is slightly better within the band of interest. The patterns of those designs are shown similarly in Figure 4.13. The peak directivities are about 8 dBi and 7.5 dBi for aperture coupled and via feeding designs, respectively. Interestingly, the dual max directions in those directive patterns, at around $\pm 22.5^\circ$, accomplish an 80° HPBW in the yOx plane. Nevertheless, the aperture coupling design has a slightly lower side-lobe level. From Figure 4.14, it is shown that the via feeding antenna has stable 7dBi gain on average, higher than 6 dBi on average of aperture coupled design. Finally, it is worth noted that both of them yield around -1 dB radiation efficiency within the frequency band and it gradually decreases at the high end of the band.

4.2.2 Via direct feed array design

Via-direct feeding design has been realized numerically in HFSS simulations and later fabricated for experimental evaluation. An advantage over the former design is the flexibility in the implementation of the feeding network. A future deployment dual-polarization antenna will also likely be the second

type of design thanks to lower complexity. This sub-section studies different properties of via-direct feeding design in an array, including bandwidth, gain, stability over frequency. The advance in PCB technologies can allow complicated design, like with the mentioned blind/buried vias. The array design will take the advantage to give a boost to performances.

For the sake of fabrication simplification, the patches are turned 90° . The elemental design still has good characteristics. The insertion loss lower than 12.5 dB is assured over the n258 band. Again, the stacked patch really helps enlarge the bandwidth as the antenna gains some height. Directivity is around 8 dBi with an 80° of half-power-beamwidth.

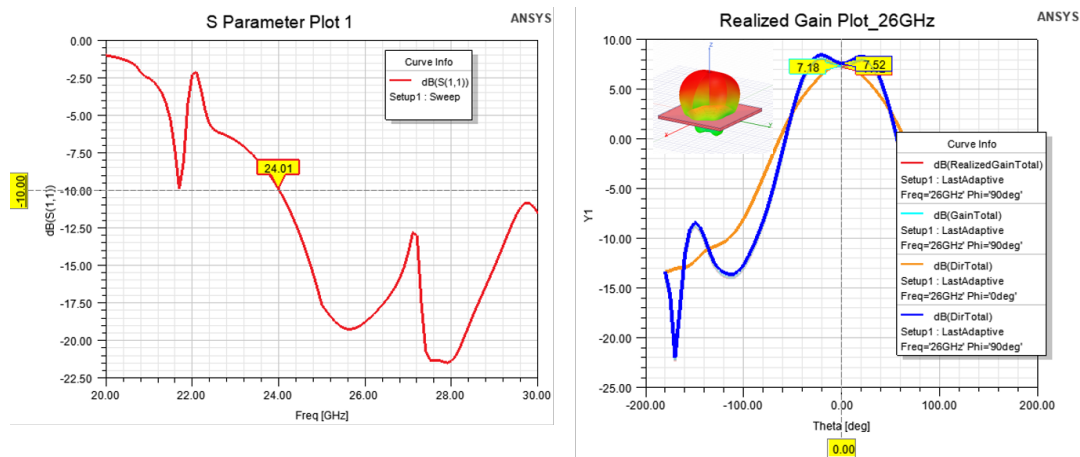


FIGURE 4.15: Matching and pattern of single design for via-direct feeding type.

A 1×4 array is designed. To excite the array gain, a feeding network is designed to implement Wilkinson dividers. Given the stack-up (in previous sections), the 50Ω -transmission line has a 0.5 mm width. The width is later optimized into 0.55 mm using ADS and verified again in HFSS. This network is designed with 1 common port and 8 antenna ports. It is shown that all ports have insertion loss lower than 12 dB. Transmission is -10.1 dB and -10.6 dB from common port to far ports (3, 5, 7, 9) and near ones (2, 4, 6, 8). Far and near is with respect to the distance toward the common port. Therefore, the total loss in transmission is around -5.8 dB.

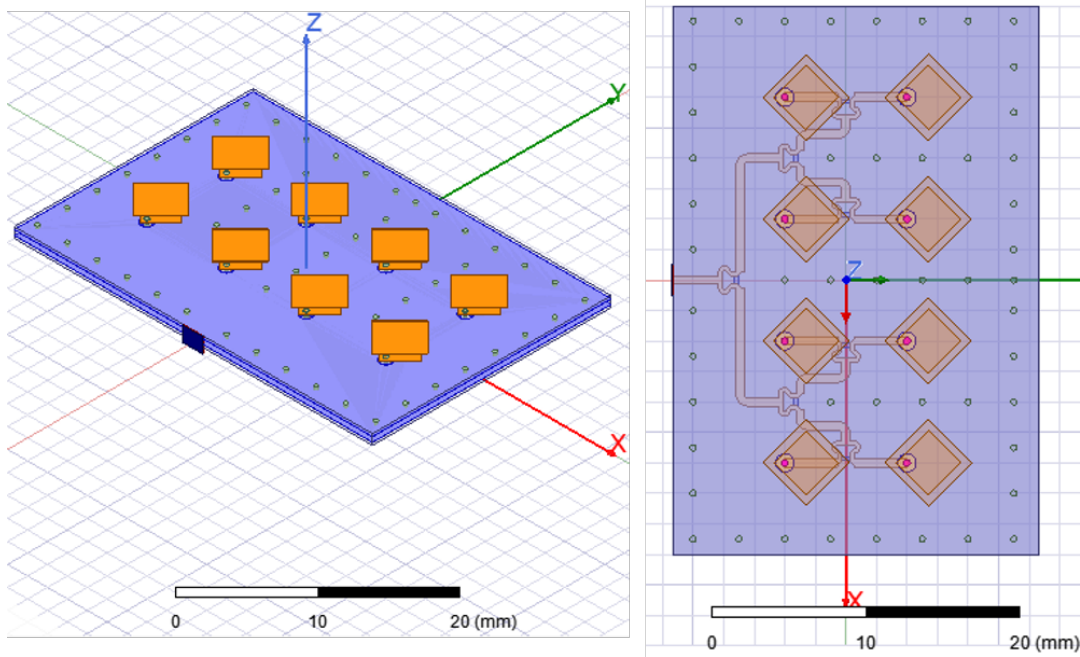


FIGURE 4.16: H-plane array.

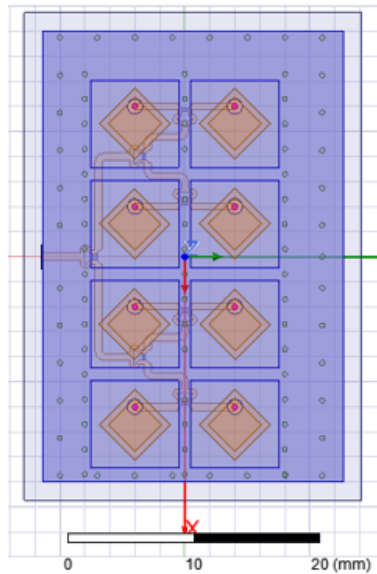


FIGURE 4.17: E-plane array.

The final design takes shape as in Figure 4.18 where the distance of elements and their orientation is to be studied. In Figure 4.16 the longer side of the array is in the H-plane of the patches, meanwhile, it is in E-plane in Figure 4.17. The cavity of the elemental design is kept, and it helps improve the antenna performance.

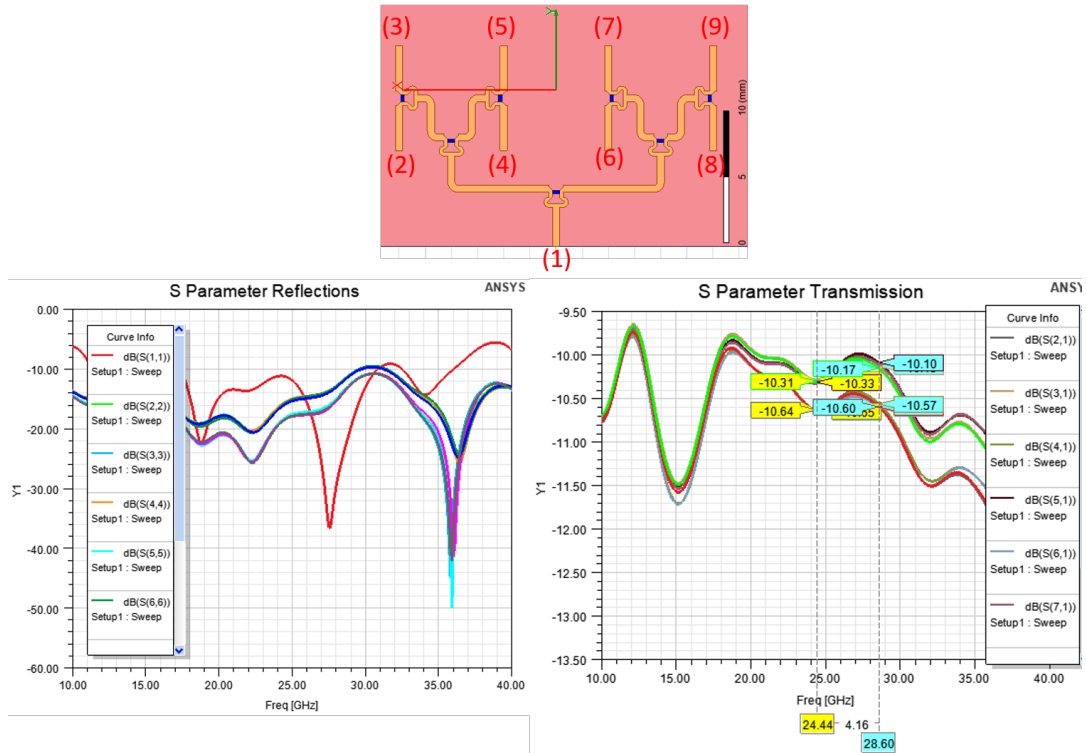


FIGURE 4.18: 1-to-8 Wilkinson feeding network.

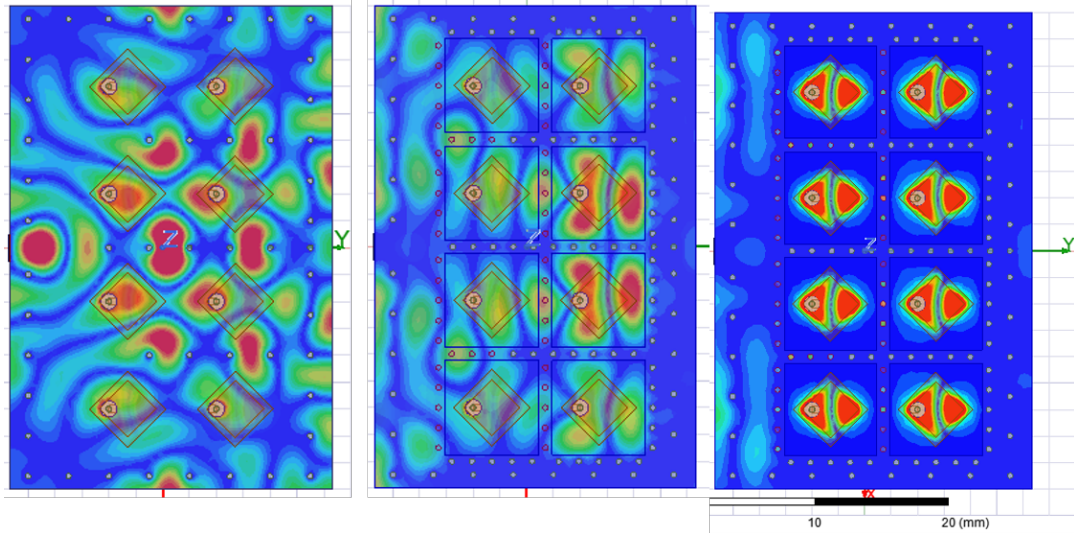


FIGURE 4.19: The effectiveness of vias in PCB, from left to right: with few vias, with additional vias and with additional blind/buried vias.

The via placement is critical for return current in high speed and RF design. One should know that multiple ground plane is likely to be used in RF PCB designs. Therefore, the number of vias must be sufficient to reduce the

impedance of the return current. Otherwise, there will be losses and unintended effects. A rule of thumb is that the longest distance between 2 vias is $\lambda/20$ to block a traverse wave, where λ is its wavelength. This rule is commonly applied for Surface Integration Waveguide (SIW) too. Figure 4.19 shows the surface wave on the second layer to the patch layer. There are remarks for designs from left to right as follow:

- Only a few vias to connect different ground planes. It can be seen that surface waves are chaotically moving toward the edges. Two main types of losses are caused by this. Firstly, the surface waves inside a lossy substrate result in dielectric loss. Secondly, the waves toward the edges eventually radiate, hence causing unwanted radiation losses and a distorted radiation pattern. The latter can contribute to interference in the system where the PCB is integrated too.
- More vias are added to form the cavities around the patch. However, as there is a feeding network on the other side of the PCB, normal vias that go through all layers cannot be fully placed on the left side. The surface waves can still travel to this side of the PCB resulting in losses as the previous design. The radiation is less significant and concentrated toward the common port.
- Some blind and buried vias are placed at the bottom (feeding network side) to have a full cavity and to enhance the transmission, as being illustrated in Figure 4.20. The waves are concentrated inside the cavities, forming a clear TM₀₁ mode. There are still small leakages toward the common port side, although it is much less significant. All in all, to avoid distort radiation pattern and high dielectric loss, vias need to be placed sufficiently and cleverly.

Table 4.1 shows the impedance matching bandwidth and radiation properties at 26 GHz of E-plane and H-plane designs with and without the vias.

TABLE 4.1: Comparison of different configurations of via direct feeding array antenna.

Configs	Matching	Directivity	Tot. loss	Side-lobe level
$0.7\lambda \times 0.7\lambda$, H-plane, without blind vias	23.23 28.9 GHz	– 15.73 dBi	3.08 dB	11.39 dB
$0.7\lambda \times 0.7\lambda$, H-plane, with blind vias	23.14 29.47 GHz	– 16.37 dBi	2.05 dB	12.4 dB
$0.7\lambda \times 0.7\lambda$, E-plane, without blind vias	23.2 – 28.9 GHz	15.73 dBi	2.48 dB	13.31 dB
$0.7\lambda \times 0.7\lambda$, E-plane, with blind vias	23.28 29.6 GHz	– 16.01 dBi	2.52 dB	15.27 dB
$0.5\lambda \times 0.5\lambda$, E-plane, with blind vias	24.93 26.91 GHz	– 10.71 dBi	2.81 dB	14.38 dB

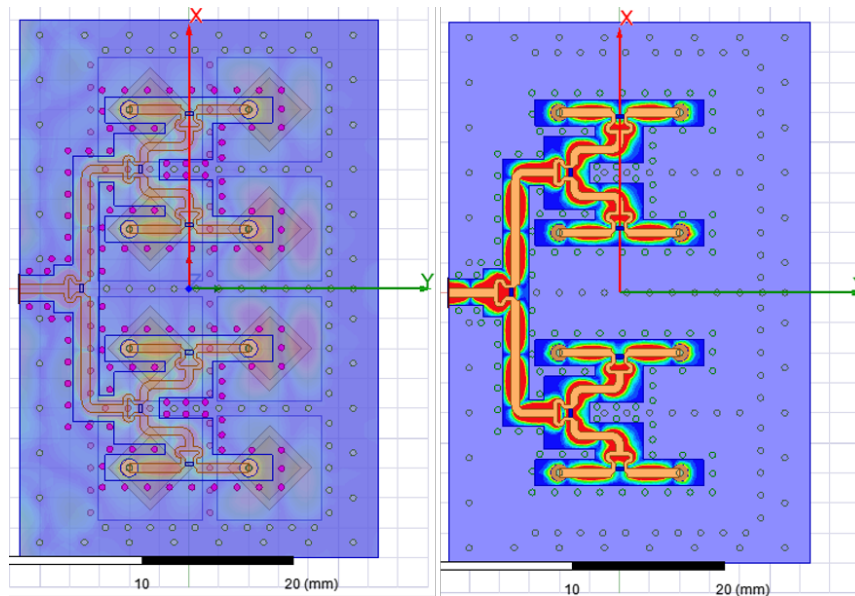


FIGURE 4.20: Blind vias (pink color in the transparent view on the left) at the bottom layer to enhance TM line transmission.

A design without the stacked patch is also checked as the final study case. It should be noted that the sidelobe level is the distance between the main lobe and the second-highest lobes. The sidelobe levels are lower than 10dB for all designs. Most radiation patterns resemble the one of E-plane array with the blind vias that are shown in Figure 4.20 By definition, radiation loss is the difference in dB between Directivity and Gain, and total loss takes insertion loss into account, thus the difference between Directivity and Realized gain.

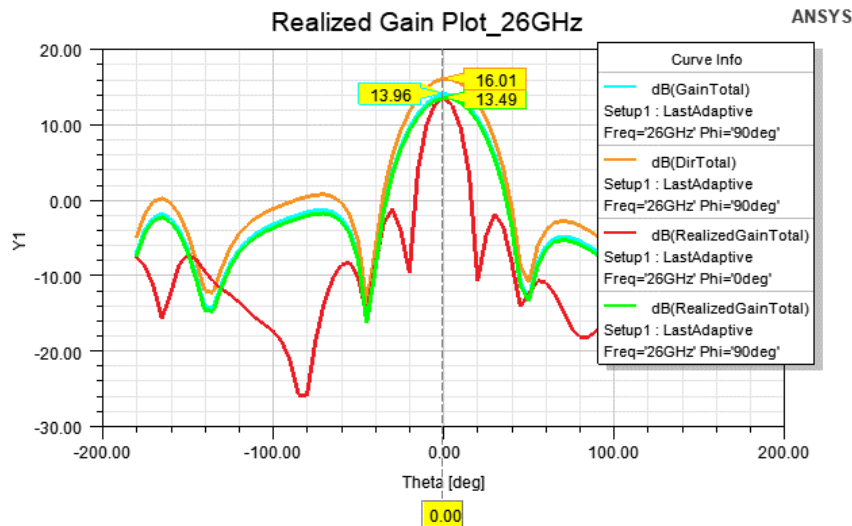


FIGURE 4.21: Directivity and Gains for E-plane design with blind vias.

The calculation is illustrated, for example, in Figure 4.21.

Let's consider the first four designs with a stacked patch. It can be seen from the table that E-plane designs and H-plane ones perform closely in terms of directivity. The highest directivity is around 16.4 dBi. The level corresponds to the 7.4 dBi elemental directivity plus 9 dB from array gain. The side-lobe level in E-plane designs is around 3 dB better in comparison with H-plane ones, regardless of via configuration.

It is also clear that the additional special vias improve the directivity by reducing the radiation toward the edges of the PCB. The side-lobes level is around 1 dB lower for E-plane design and 2 dB for H-plane one. In addition, it further reduces the dielectric loss, especially in H-plane designs. The best case for the side lobe is the E-plane design, reinforced by the vias, with a 15.3 dB difference in comparison with the main lobe. Likewise, the bandwidth is also improved by the blind/buried vias. For the cases without these vias, the frequency band is around 23.2 – 28.9 GHz. With the vias, the highest match frequency increases up to 29.6 GHz. Not only the band covers the n258 band, but now it can also cover the n257 band.

In addition to the stacked type antenna, a single-patch design is also studied. The bandwidth is about 7.6%, 24.9 – 26.9 GHz, narrower as the height of the antenna is lower. The directivity is around 6dB, which is lower than the previous case too. The coupling effect between the two patches is clearly pulling the waves to come out in the broadside direction. That also explains why the total loss is higher for this case as there are more surface waves inside the substrates. Although the whole n258 band is not covered, the single-patch design is advantageous in terms of fabrication. For both aperture-coupling design and via direct feeding, the hanging patches are done manually using Epoxy wall and flexible Kapton. As long as the stacked patch is not required, the fabrication procedure is only sending the PCB design to the manufacturer.

The variation of directivity over the working frequency band of the improved E-plane design is shown in Figure 4.22. The array is along the directivity increases with frequency from 15.7 dBi at 24 GHz to 17.3 dBi at 28 GHz. It then decreases to 16.9 dBi at 29 GHz. The matching is not as good at 23 GHz and the directivity at this frequency is also low, 15.7 dBi. Overall, the variation is insignificant within the band.

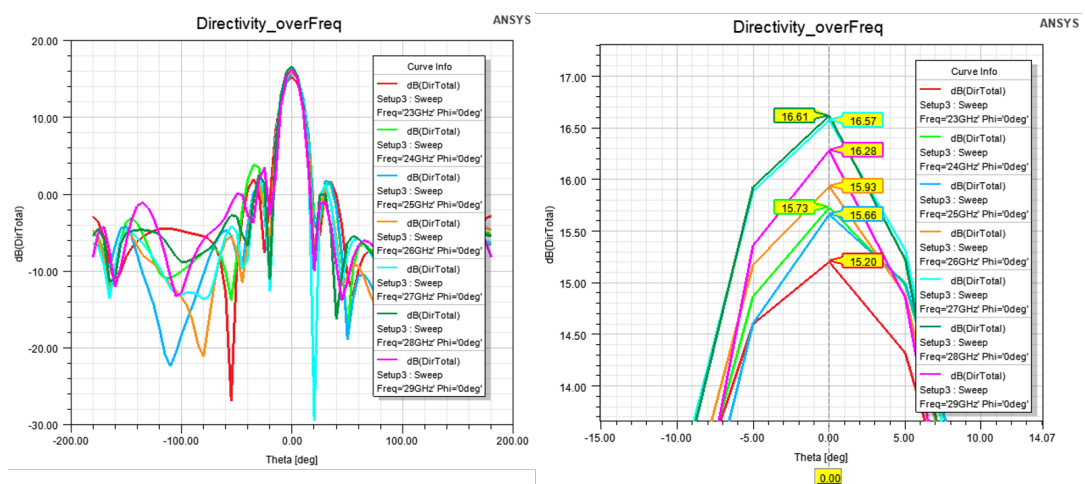


FIGURE 4.22: Directivity variation over frequency band, zoom out (left) and zoom in (right).

4.2.3 Aperture-coupled patch array design

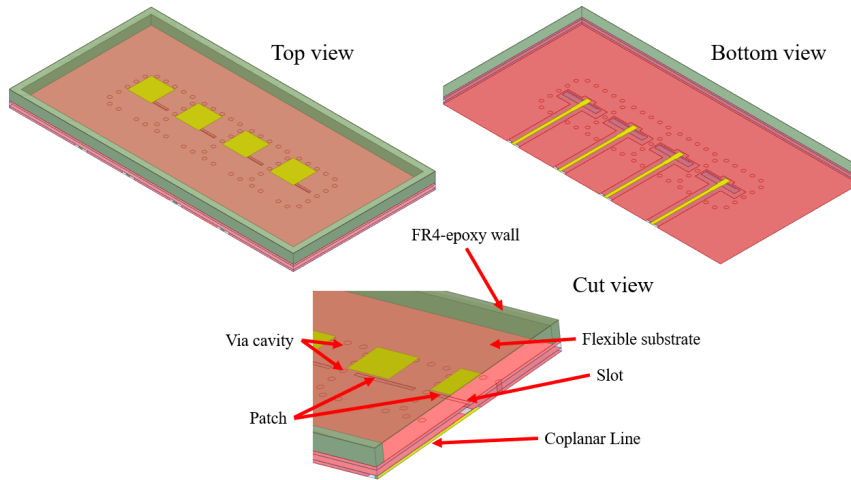


FIGURE 4.23: Top, bottom and cut views of the simulated array design with a substrate wall support.

Given the similar results between via feeding and aperture coupling feeding, the two designs are equally qualified for fabrication. However, the second type has an advantage in saving PCB real estate as aforementioned. Just as direct via feeding patch design, aperture coupled antenna is also developed into an array antenna. It is chosen as elementary to a 4-by-1 array. The finalization is illustrated in Figure 4.23. The four elements are placed $0.7\lambda_0$ to each other in a linear array in H-plane and electrically separated by the previously introduced cavity.

To provide a realistic model after prototyping, the hanging patch needs support to stay in the air. Therefore, a 1 mm width dielectric wall made of FR4-epoxy is added on the top layer. This wall is 1.6 mm high, as of the distance from the patch to PCB. Four patches are etched to a flexible substrate of $50\mu\text{m}$ high, whose relative permittivity is 3.6 and dielectric lost tangent is 0.02. The flexible is thin enough to cause negligible differences in the pattern, as can be seen in Figure 4.24. Finally, the substrate is pasted to the substrate wall, facing the patches toward $-Oz$ -direction.

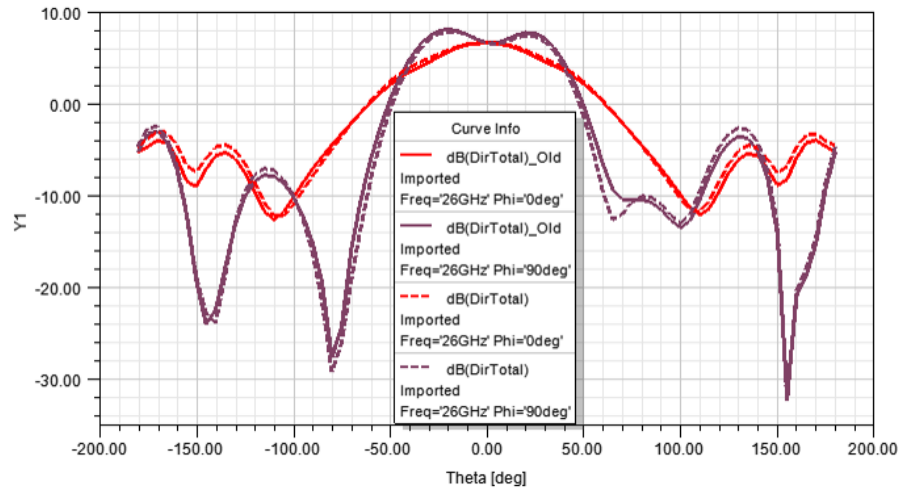


FIGURE 4.24: Minimal differences in radiation pattern between designs with (dash line) and without (solid line) a flexible substrate.

All the array elements are matched from 23 GHz to 28 GHz at -10dB criteria. The two middle elements have more fluctuations in its reflection coefficient curves. In addition, the array isolation is below 24 dB, satisfying the isolation criteria. The array isolation is initially reported as low as 13 dB without the cavity, showing its necessity. The array gain pattern in the broadside direction is shown in Figure 4.26. The array realized gain achieves 6 dB higher compared to the element's gain reported in Section. 4.2. Therefore, the structure is practical and efficient enough for prototyping.

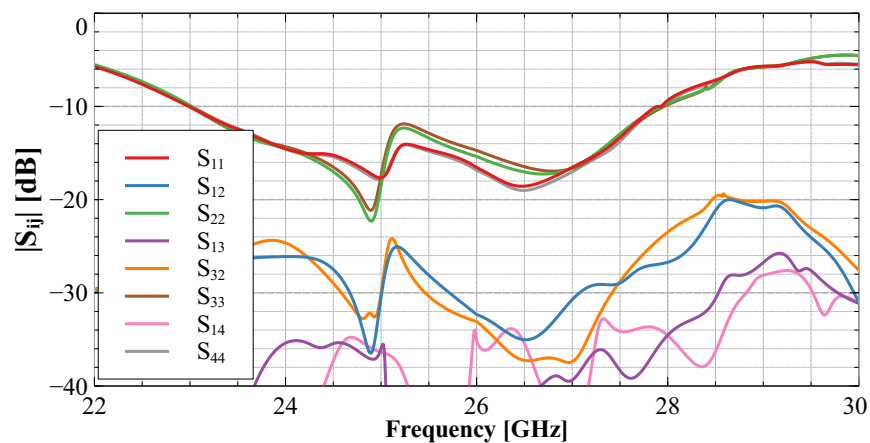


FIGURE 4.25: Numerical scattering parameters of the array.

In comparison with the via direct feeding design, the four elements are fed separately. Input phases and amplitudes can be altered to change the

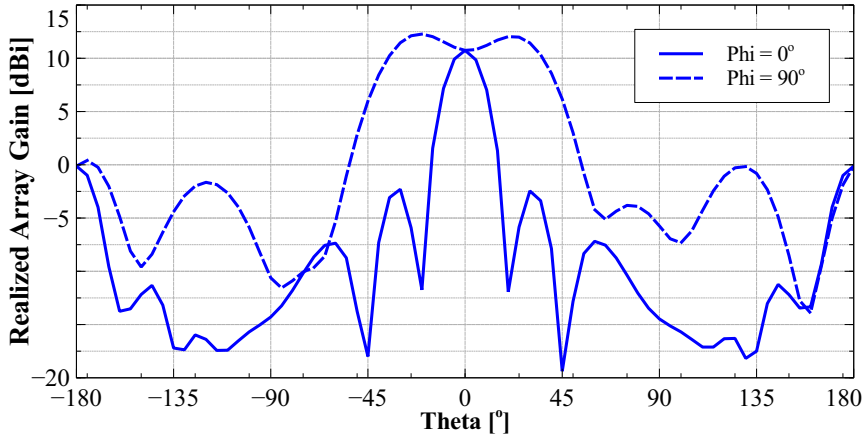


FIGURE 4.26: Demonstration of beam synthesizing at main direction.

radiation pattern. This allows evaluating the MIMO capability of the design, especially in the presence of blockages.

Assuming the center of the array is the reference point, the 4-element array factor is derived as follows.

$$AF = \text{real}\left(\sum_{n=1}^4 e^{j(n-1)\psi}\right) = \frac{\sin(2\psi)}{\sin(0.5\psi)} \quad (4.8)$$

where

$$\psi = kd \sin \theta \cos \phi + \beta \quad (4.9)$$

where n is the element index, k is the wavenumber and β is the input phase step. It is noted that the elements are arranged along x -axis so a complex term is used instead of just cosine, like in [84] (page 294). Replacing $\phi = 0^\circ$, $d = 0.7\lambda$, $\beta = \{120^\circ, 60^\circ, 0^\circ, -60^\circ, -120^\circ\}$ to the equations, we can plot the array factor in linear scale in xOz plane with different phase steps by Matlab, as illustrated in Figure 4.27. With those phase steps, the array factor is maximized at $\theta \approx \{-30^\circ, -15^\circ, 0^\circ, 15^\circ, 30^\circ\}$. It indicates beam steering capability in these directions. The maximum value 4 means that the gain at those directions the input phases of all elements are constructive and hence the array gets 6 dB more gain.

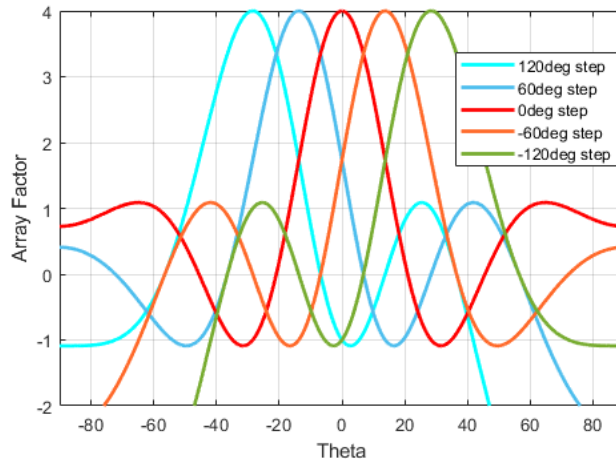


FIGURE 4.27: Array factor of the an 0.7λ array with four elements.

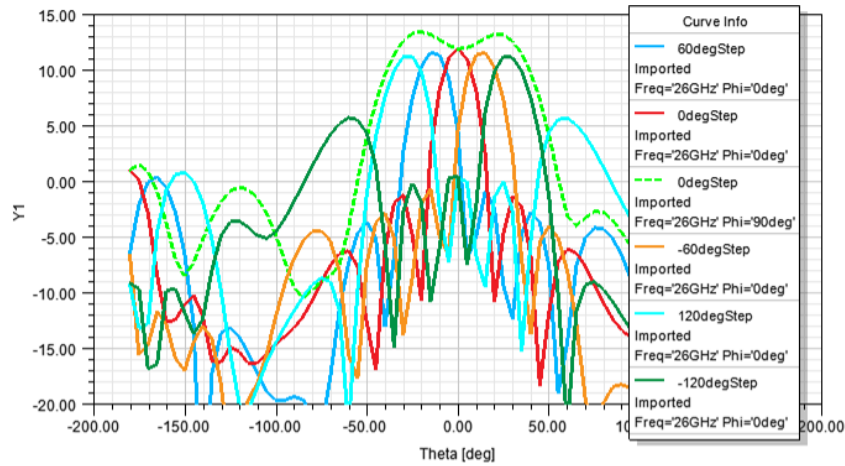


FIGURE 4.28: Beam steering by changing input phase step to the array.

$$E_{field_{total-linear}} = E_{field_{element-linear}} \times AF \quad (4.10)$$

Figure 4.28 shows the steering patterns when feeding the previous set of step phases. The peaks are at the same places as in the array factors' pattern. It should be noted that the array factor amplifies the element's gain when the array elements are uniform like in equation 4.10. That is the reason those peaks take the slope of the element pattern when going further from the center. In the 0° -phase step case, the pattern in yOz takes the same form as the element pattern and is amplified by 6 dB. With other input phase steps, 6dB

of array gain is unlikely.

Finally, with the absence of the feeding network, no blind/buried via is needed in consequence. Should the array be later developed with more integration, those vias are useful again.

4.3 Experimental evaluations of the designs

4.3.1 Via direct feed design

The design with the array elements arranged along E-plane and with 0.7λ distance has been selected for fabrication. In addition to the 1×4 array, a smaller 1×2 array, a single element antenna and a dual ports array 2×4 have also been sent for fabrication. The 2×4 array with two ports allows beam-steering functions in H-plane.

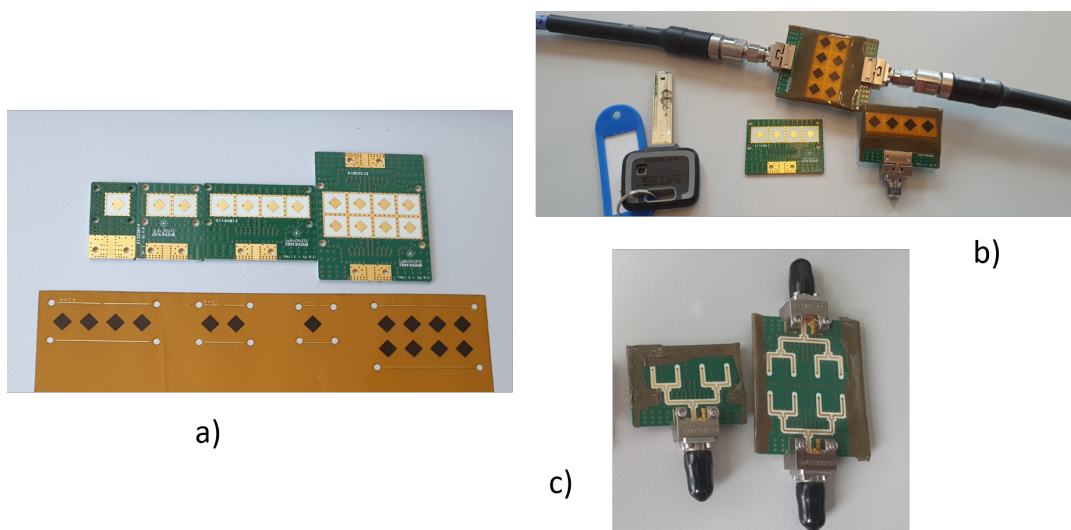


FIGURE 4.29: Via feeding prototypes before (a) and after (b) adding the stacked patch. The back of the prototypes is in (c).

Figure 4.30 a) shows the prototypes received from the PCB manufacturer. At the bottom of the picture a) is the flexible Kapton substrate that contains the second patches. The two big arrays 1×4 and 2×4 are then being proceeded to integrate the second patch as can be seen in picture b). The process

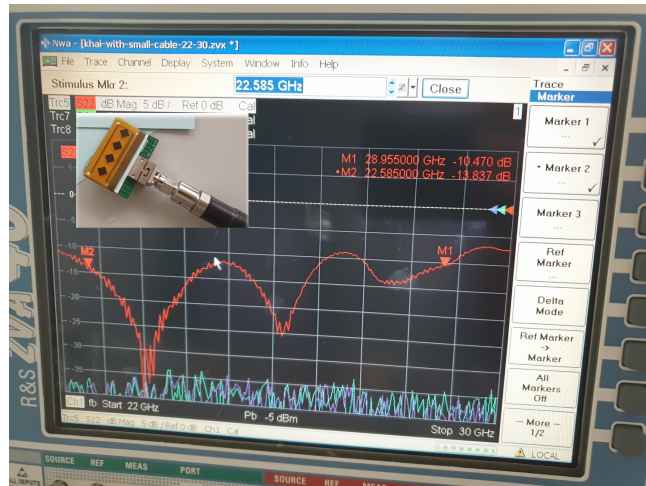


FIGURE 4.30: Impedance matching of the 1×4 via feeding array prototype.

to make the second patch is similar to the one using for the aperture coupled array prototype.

Apparently, the 1×4 array experiences a good impedance matching from 22.5 GHz to 29 GHz. It is rather unsurprising as the numerical studies have similar matching performance.

Unfortunately, other measurements for this array are not finished yet at the time this thesis is written. The experimental performances are expected to not too different. The results will eventually be added with analysis.

4.3.2 Aperture-coupled patch design

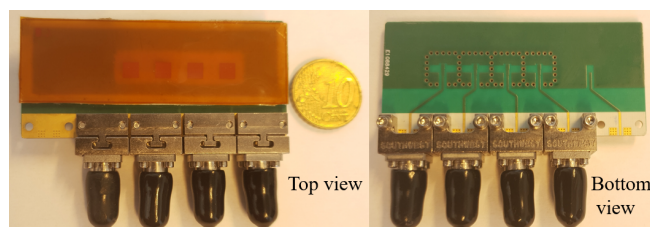


FIGURE 4.31: Top and bottom views of the prototype with connectors.

The array prototype is equipped with some more features, including the fifth open microstrip line for calibration and an extended PCB part toward $-O_y$ -direction for connectors' footprint. The final prototype is illustrated in

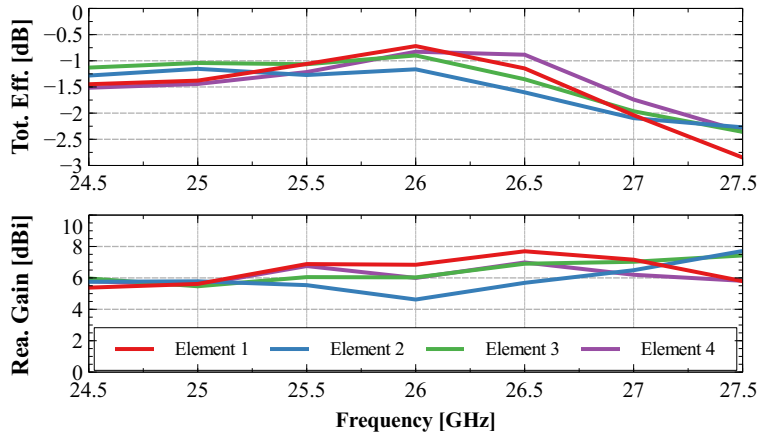


FIGURE 4.32: Measured total efficiencies and realized gain at $\theta = 0^\circ, \phi = 0^\circ$ of all array elements over frequency.

Figure 4.31. The fabrication of the substrate wall and the hanging patches over the air is done manually. This can be the main source of uncertainties. However, the work is calibrated based on the impedance matching level and shown working correctly. Measurements with a Vector Network Analyzer assure a minimum of 8 dB of return loss and a minimum of 25 dB of isolation of the prototype.

The far-field radiation measurements have been then done in the anechoic chamber in LEAT. Every element is fed separately in separate measurements. As discussed previously, this study will avoid confrontation with mutual coupling measurements. This can be done thanks to the high level in mentioned isolation. Therefore, while one antenna element is fed, the others are matched to a 50Ω load. There are observable variations in terms of total efficiencies and realized gain levels at $\theta = 0^\circ, \phi = 0^\circ$, in Figure 4.33. The total measured efficiency is average -1.2 dB from 24 GHz to 26.5 GHz. However, it drops to -2 dB at 27 GHz and to -3 dB at 27.5 GHz for the worse element. The realized gains at the broadside direction are stable, varying around 6 dBi. The two middle elements have their gains become higher at 27.5 GHz.

Figure 4.33 illustrates the four-element realized gain patterns in xOz -plane (H-plane) and yOx -plane (E-plane) at 26 GHz. In H-plane, an HPBW around

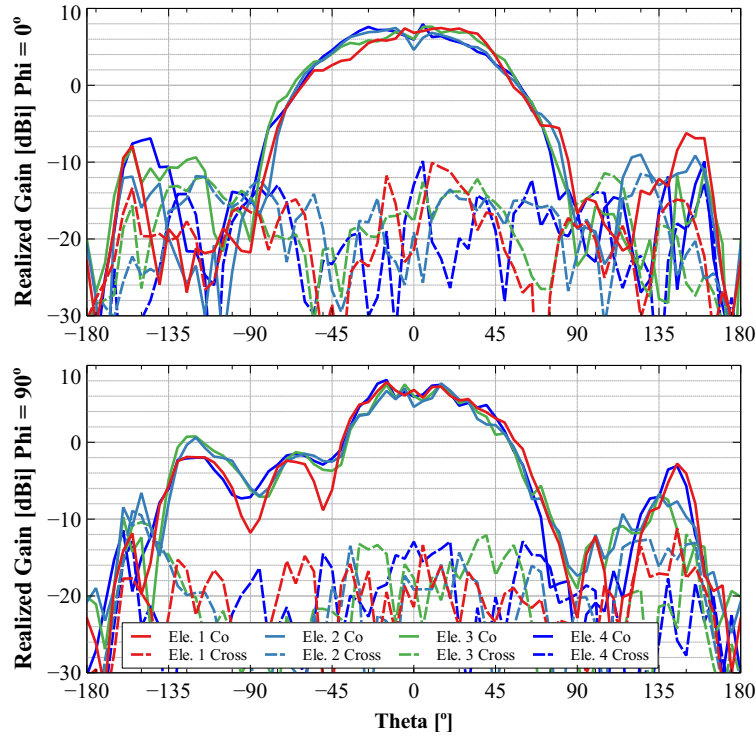


FIGURE 4.33: Realized gain patterns of all array element in xOz (top) and yOx (bottom) planes at 26 GHz.

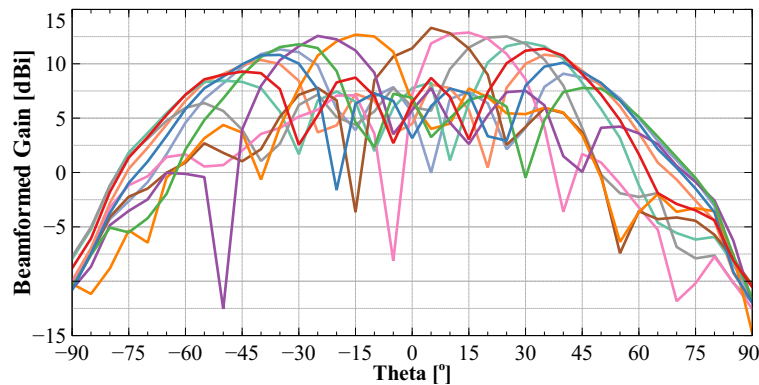


FIGURE 4.34: Scanning beams from $\theta = -50^\circ$ to $\theta = 50^\circ$ in xOz -plane at 26 GHz.

90° large is obtained, which is slightly larger than the numerical result. A flat gain of around 8 dB can be seen from $\theta = -30^\circ$ to 30° . However, a big distortion is observable in E-plane at the bottom angles from -90° to -45° , which differs from the numerical results. It can be explained due to the close vicinity of connectors.

With the single gain pattern in hand, the beamforming patterns are performed using four 5-bit phase-shifters to excite the array. Different from the

simulation where the pattern is more uniform, the beamforming in measurement is done using optimization, not using the array factor. The beams are optimized using the brute-force method to steer in directions from $\theta = -50^\circ$ to $\theta = 50^\circ$, with a 10° step. The synthesized beams show that the prototype is capable of achieving a maximum of 13 dBi gain and covering a 90° angle in H-plane.

4.4 An end-fire array antenna at mmWave

4.4.1 Array design and integration in mobile phone casing

A 24.0 – 28.0 GHz prototype was designed in the frame of mmMagic H2020 project by P. Ratajczak from Orange Lab. [86]. In the frame of this work, we used this design to assess beamforming capabilities in a mobile phone at mmWave. Backed dipole antenna structures were selected for the design because of their wide frequency band and beamwidth [87]. The proposed structure has a dimension of $3.8 \times 5.15 \text{ mm}^2$ as shown in Figure 4.35. In order to enable a beam scan up to 60° without grating lobes, the element array spacing has to be kept around $0.5\lambda_0$. Considering the size of the dipole which is very close to the array spacing, the $\pm 45^\circ$ polarization is more capable to maintain a low level of coupling between each element. Two sub-arrays are placed on the mobile phone as shown in Figure 4.35. In this study, only the top sub-array (antenna 1, 2, 3, and 4) is used for measurements.

The S-matrix of the handset breadboard has been measured. The first K connectors ($VSWR \approx 1.3$) have been extracted to the measurement by time-domain filtering. The 8 measured input impedances are presented in Figure 4.36. Figure 4.36 presents S_{1j} there we can observe identical compartments of the mutual couplings between the first element and the 7 others.

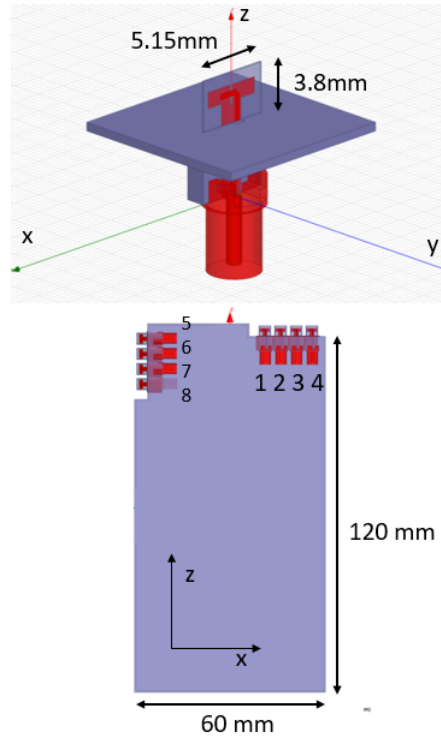


FIGURE 4.35: 3D model of the proposed antenna structure

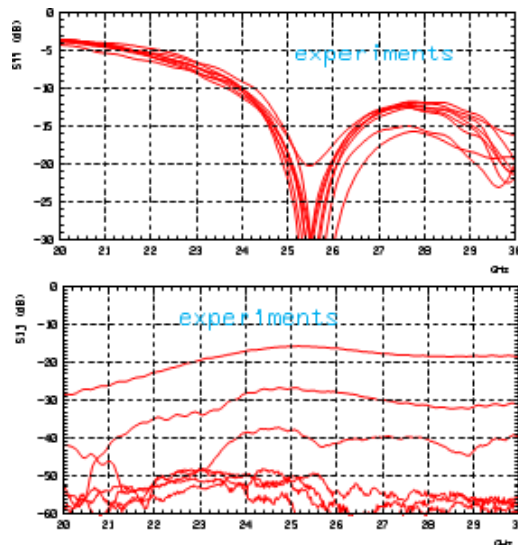


FIGURE 4.36: S-Parameters measurements of the 8 elements

4.4.2 Assessment of beamforming in mmWave

The objective of the study is to assess the influence of phase shift resolution on the beamforming capabilities of a 4-element array integrated into a smartphone.

Recently, most of the 5G works have been shifted to the 24 – 28 GHz



FIGURE 4.37: View of the prototype during measurements

bands [88]. The very high path loss at these millimeter-wave bands can only be compensated by the use of multiple antennae at the transmission and reception part.

Moreover, the concept of hybrid beamforming has been promoted to limit power consumption, especially on the UE side [89]. Hybrid beamforming is usually based on sub-arrays integrating digital phase shifters with a limited resolution [90]. In this work, a 4 element array of dipoles is integrated into a mobile phone. Amplitude and phase on the half hemisphere of the four single elements are measured. The beamforming performance is calculated in post-processing for different phase-shifter resolutions.

The fabricated prototype is measured in order to assess the beamforming capabilities of the antenna system. In the first part, the capability of the array to maximize the gain in one direction is studied. In the second part, the capability to minimize the gain in one direction is analyzed.

Measurement:

Measurements were performed using a 3-axis scanner with a fixed Antenna Under Test (AUT) designed by NSI [91]. This robotic positioning system consists of three rotational positioners. The first one, mounted on a large floor stand, defines the horizontal phi-axis of rotation. The second positioner is

attached to the rotation stage with a 90° angle to form the theta-axis. The last positioner is attached to the rotation stage forms the pol-axis and manages the polarization rotation stage. A specific antenna holder made of low-permittivity foam material has been designed and manufactured to limit as much as possible the interaction with the AUT and can be viewed in Figure 4.37. The 4 antennas of the frontal sub-array are measured in xOz -plane and the total gain is presented in Figure 4.38. It can be observed that the radiation pattern of the four antennas is quite similar.

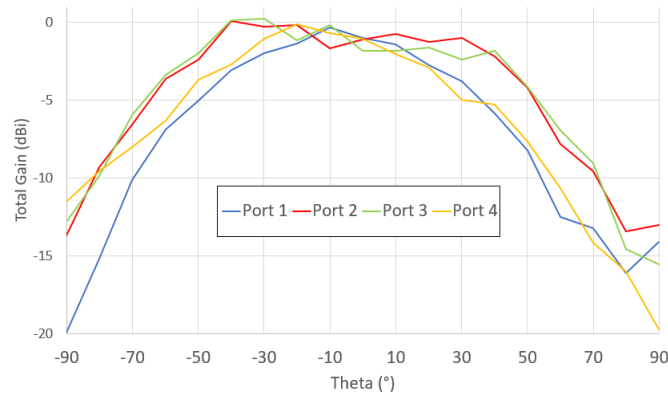


FIGURE 4.38: Total gain measurement of the 4 antennas in xOZ plane

Processing:

The terminal prototype is composed of 2 sub-arrays of 4 antennas radiating towards the z -axis (antennas 1, 2, 3 and 4) and towards the $-Ox$ -axis (antennas 5, 6, 7 and 8). Each array can be used in beamforming mode to increase the gain towards a specific direction. The beamforming gain (or array gain) G_{array} for each array is obtained by computing a linear combination of the single element gains, i.e., as

$$G_{array}(\phi, \theta) = \sum_{i=1}^n G_i(\theta, \phi) e^{j\gamma_i} \quad (4.11)$$

where G_i is the gain of the single elements, and γ_i is the phase offset that can be introduced between the elements of the array (we are assuming here that no amplitude difference can be introduced).

The beamforming gain can be maximized in each direction (ϕ, θ) by optimizing the phase difference γ . The result is the so-called Total Scan Pattern (TSP) gain, introduced in [92] and [77], and defined as

$$G_{TSP}(\theta, \phi) = \max_{\gamma_i} \{G_{array}(\theta, \phi)\}. \quad (4.12)$$

If digital phase shifters are considered, the phase resolution will affect the maximal gain. In this study, we considered the digital phase shift from 2 (90° resolution) to 5 bits (11.25°) of control. For each resolution, the TSP is computed for xOz -plane and presented in Figure 4.39. It can be clearly seen that a very coarse resolution (e.g 90°) is sufficient to reach the beamforming limit.

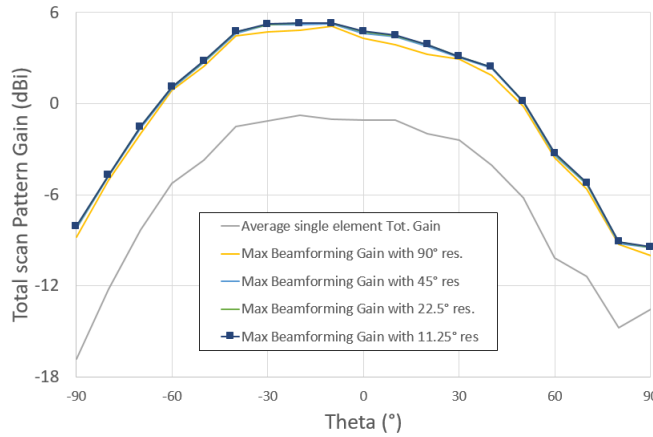


FIGURE 4.39: Processing of the maximal Beamforming gain for different phase resolutions

In the second part, we propose to study the capabilities of the sub-array to minimize the gain in each direction (ϕ, θ) by optimizing the phase difference. We propose to call this result the Null Scan Pattern (NSP) gain defined as:

$$G_{NSP}(\theta, \phi) = \min_{\gamma_i} \{G_{array}(\theta, \phi)\}. \quad (4.13)$$

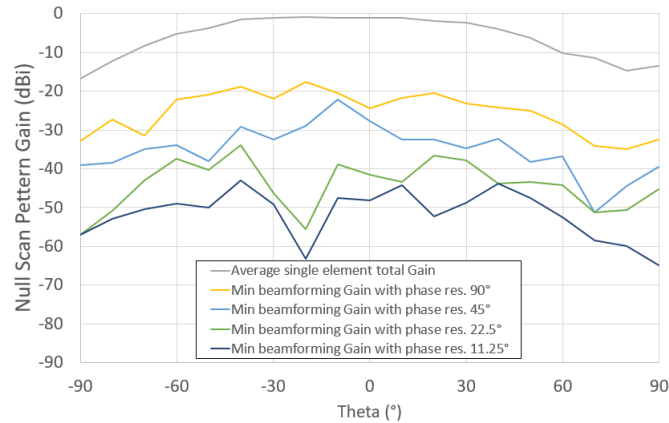


FIGURE 4.40: Processing of the minimal Beamforming gain for different phase resolutions

For the different phase resolutions, the NSP is computed in xOz -plane and presented in Figure 4.40. Differently from the TSP, the NSP benefits from the refinement of the resolution: the higher the resolution, the lower minimum of total gain value. In fact, for a communication system based on beamforming like 5G, minimizing signal power in one direction, that means interference in that direction can be better decreased. Therefore, for signal cancellation applications, it is recommended to use high-resolution phase shifters.

The results show that the maximal beamforming request only a very coarse resolution to reach the maximal gain limit. For nulling capabilities, a fine resolution is needed to achieve high cancellation performance.

4.5 Conclusion

In this Chapter, a comparison between two types of excitation for patch antennas on a multilayer PCB stack-up: direct via connecting and aperture coupling. It has been shown that the two designs can be optimized to yield similar performances, given the same antenna's size. The aperture coupling design was chosen to make a 1×4 array. The array isolation is enhanced

by the help of cavities. A prototype array has been fabricated. The experimental measurements confirm the agreement to the numerical results. The separated gain patterns have also been synthesized. It illustrates the beamforming performance of the design.

For further discussion, the array design need to be upgraded in terms of the number of elements and polarization diversity. With numerous elements, the aperture coupling provides better heat dissipation with a nearly intact top layer. Meanwhile, via feeding can be a better solution for dual-port and dual-polarization designs. Further studies are expected to show more interesting information.

In addition to the broadside arrays, an end-fire design provided by Orange is also used for the study of the influence of phase resolution on beamforming performance in a smartphone at 26GHz is proposed. The results show that the maximal beamforming requests only a very coarse resolution to reach the maximal gain limit. For nulling capabilities, a fine resolution is needed to achieve high cancellation performance.

With those good designs at hand, several measurements with the user's finger in close proximity of the mmWave antennas will proceed in the next Chapter. The results shed new light on different effects of the fingers on mmWave mobile antennas.

Chapter 5

Human finger's effects on array antenna at mmWave

5.1 Human's effect on mmWave radiation and measurement availability

Although a single resonator at mmWave has a very small size thanks to small electrical wavelength, antenna arrays are norm for both base station (BS) and User Equipment (UE) to achieve a sufficient signal-to-noise-ratio (SNR) to compensate for higher propagation loss at mmWave. A significant research effort has been conducted to characterize the propagation environment at mmWave as well as in the design of the BS antennas [15], [93]. However, the design and characterization of UE antennas at mmWave got considerably less attention compared to the studies of pathloss and BS antennas. There are many challenges involved in the design of mmWave terminal antennas that have to be addressed carefully [94]. More specifically, due to the limited size of the mobile phone, antennas will be in close proximity to nearby objects, such as the cover of the UE. As the cover will be in the near-field (NF) region of the antenna module, it will affect the antenna radiation performance [95], [96]. The effects of the casing on the radiation performance of the UE antennas' have been presented in [97], [98]. A gain reduction of 3.5 dB due to

metal casing is reported in [97] for high directivity antenna array at 39 GHz. The paper [98] studied the effect of casing in terms of radiation efficiency and reports a reduction ranging from 4.6% to 8.3% depending on different types of antennas at 28 GHz. Therefore, at mmWave, the cover effect should be included in the study of antenna radiation characteristics. For example, coverage efficiency is one of the important metrics to characterize antenna radiation performance, which is defined by the ratio of the solid angle that UE can cover the total 3D spherical coverage. Another important concern comes from the user's hand and body, which are also in the NF of the antenna and that can affect the antenna performance significantly. In addition, the measurement-based study of antenna-human interaction is very limited because of challenges in a measurement setup and lack of reliable human phantoms at mmWave. In most antenna measurement setups, Device Under Test (DUT) is mounted on a 2 axis of rotation platform in front of a reference probe [99]. A test with a real human requires otherwise a reference probe moving around a fixed DUT for the sake of high stability and repeatability.

The human's body effect on antenna radiation characteristics draws more attention recently and has been reported in [17]–[19], [97], [100]. Mostly, those effects are reported in terms of losses in spherical coverage or in gain. In [19], simulations show up to 20 dB of gain reduction when a finger is placed in the NF of a patch antenna array working at 28 GHz. The work in [17] shows that human shadowing can cause a 20 – 25 dB of reduction of the received power and a 30% decrease in spherical coverage at 15 GHz. Those effects could also hold at higher mmWave frequencies. Especially in [18], Strytsin et al. have statistically studied the human shadowing effects of the user on the performance of the UE antenna array at 28 GHz through far-field measurements. However, for an accurate measurement, the probe antenna has to be sufficiently separated from the DUT. The sufficient separation distance is significantly larger when user holds antennas than antennas

in free-space as the equivalent dimension of radiation source becomes larger due to scattering on a body. In contrast, near-field measurement provides better accuracy and reliability, such as in [17]. Nevertheless, in the mentioned works, only the whole body is experimentally considered. The finger effect has never been reported separately in measurements due to the discussed measurement setup limitation. In fact, depending on the UE antenna types, the blockage of the user's finger can be more severe than the shadowing by the whole body [19], [101].

5.2 Radiation measurements for 5G NR and figure of merit

5.2.1 Far-field and near-field measurements for 5G NR

The level of RF integration for 5G modules is unprecedented, especially at mmWave. Firstly, it is because the antenna designs at mmWave are scaled to be smaller than a tenth of those similar ones in a sub-6GHz system. Secondly, the losses in connectors need to be reduced as much as possible because there are many more elements to handle. In consequence, antennas are integrated directly within the RF front end module. In other words, the preferable designs in mmWave are AiP or AoC.

Furthermore, a hybrid antenna architecture is required with additional analog phase shifters and gain controllers. With this high level of integration, 3GPP's working groups added some more criteria to the test parameters pool. As mentioned in Section 5.1, OTA tests become an important aspect of 5G system verification. It introduces the space domain in addition to the previous time and frequency domains.

For a Sub-6GHz system, radiated performances can be evaluated as OTA types in terms of Total Radiated Power (TRP), Total Isotropic Sensitivity (TIS),

Intermediate Channel Degradation (ICD), and Desense. Those metrics are applied also at mmWave for different conformance test cases, as shown in the tables below.

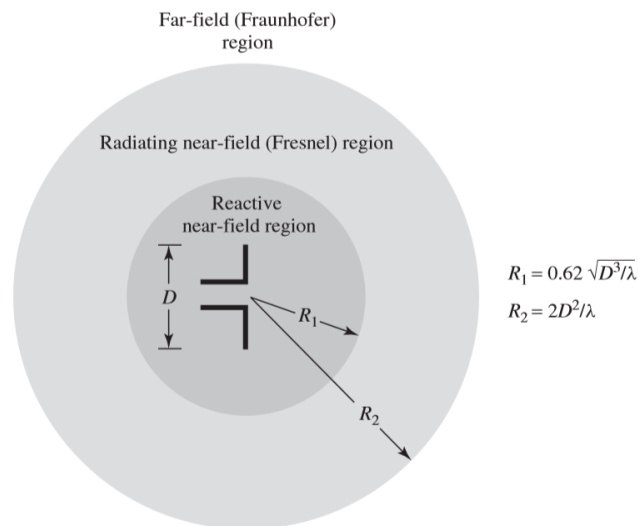


FIGURE 5.1: Far-field and near-field regions with respect to AUT's center.

The Spherical Coverage, first introduced since 3GPP Release 15 [102], gives statistical analysis for OTA measurements like Tx Max Output Power and Reference Sensitivity. The results are given as a CDF plot or table that indicates the percentages of angular coverage with respect to a certain gain/power threshold. The table below shows the required minimum EIRP higher than which 50 “percentile” of measurement data can achieve. The definition of “percentile” can be illustrated in the Figure. For a static measurement of radiation in chambers, the definition can be translated into the percentage of angular area. Meanwhile, for real case scenarios where the position of the terminal, e.g. a receiver, is totally random, it is the possibility gNB can see it regarding a certain clearness.

OTA measurement can be performed in both far-field and near-field. Far-field measurements are considered comparably easy and suitable for EIRP/TRP for Tx and EIS for Tx, etc. Far-field region of an Antenna-Under-Test (AUT) is outside the sphere centered at the center of the AUT and has a radius of

TABLE 5.1: Conformance test cases that require only 3D positioning for mmWave.

Test cases	Spatial requirement
Tx Max Output Power	EIRP on main beam
MPR and A-MPR	EIRP on main beam
Configured Tx Power	EIRP on main beam
Min Output Power	EIRP on main beam
ON/OFF time mask	EIRP on main beam
Power Control	EIRP on main beam
Freq Error	Main beam
EVM	Main beam
Carrier leakage	Main beam
In-band emissions	Main beam
Occupied Bandwidth	Main beam
Reference Sensitivity	EIS on main beam
Max Input level	EIS on main beam
Adjacent Channel Selectivity (ACS)	EIS + blocker on main beam
In-band blocking	EIS + blocker on main beam
Spurious response	TDB
Receiver Image	TDB

TABLE 5.2: Conformance test cases that require 3D pattern (or scan) for mmWave.

Test cases	Spatial requirement
Tx Max Output Power	TRP & Spherical Coverage
Tx OFF power	TRP
Spectrum Emission Mask	TRP
Adjacent Channel Leakage Ratio (ACLR)	TRP
Spurious emissions	TRP
Reference Sensitivity	Spherical Coverage
Rx Spurious Emissions	TRP
Beam correspondence	TBD

TABLE 5.3: UE spherical coverage for power class 3.

Operation band	Min EIRP at 50 th -tile CDF (dBm)
n257	11.5
n258	11.5
n260	8
n261	11.5

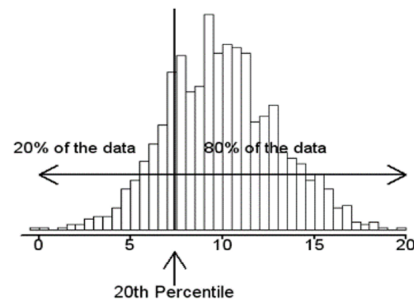


FIGURE 5.2: Spherical coverage specifications from 3GPP for different 5G mmWave bands.

$\frac{nD^2}{\lambda}$, where n commonly takes 2 to have a phase error lower than 22.5° , and D is the diameter of the smallest sphere that encloses the AUT. For better precision, n can be higher than 2. Nevertheless, the AUT's pattern is not very different from a pattern measured in an infinite far distance. In far-field, the probe receives signals from the AUT as EM planes with two components electric and magnetic vector field orthogonal to each other and orthogonal to the direction of the propagation vector. A challenge for this type of measurement might come from the path loss as the probe and the AUT are far from each other.

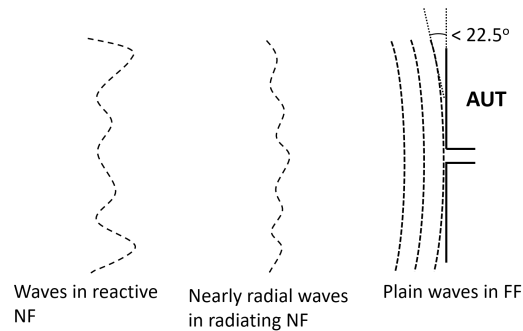


FIGURE 5.3: Waves in Near-field and Far-field, and phase error consideration in Far-field measurement in quiet zone.

Far-field measurements for large antennas require large distance between probe and antenna under test, thus large anechoic chamber. Although outdoor measurement can be done, a laboratory measurement environment is preferable for better precision and security. To this end, near field measurements can also be done and far-field pattern of an AUT can also be recovered

from that.

Reactive near-field is the sphere with $0.62\sqrt{\frac{D^3}{\lambda}}$ radius and it directly surrounds the AUT. The energy inside this region is predominantly reactive as the name suggested. Since any object in this region can couple with the AUT, hence affect the radiation pattern, not many RF measurements can perform. For instance, Special Absorption Rate (SAR) measurement is done in the reactive near-field. Radiating near field is the region between far-field and reactive near field. In this region, the waves gradually become radial. This is the region where near field measurements are conducted.

Transformations from near field to far-field can be done physically. The main idea is to transform the curvy waves in near-field to nearly planar ones at the AUT. This zone with the nearly planar waves is called a quiet zone. This can be done using a Fresnel lens, Plane-wave converter, or parabolic reflector. The finalization of the reflectors is extremely important in order to suppress the diffraction effect and to have a good quiet zone, like in Compact Antenna Test Range (CATR) set up by Rohde & Schwarz. On the other hand, near field to far-field transformation can also be done numerically. The measurements are performed in planar, cylindrical, or spherical scanning. Different from amplitude-only data of far-field one, data of near field measurement are complex, including amplitudes and phases. Multiple reflections effect between the AUT and the probe needs to be seriously taken care of for this type of measurement.

In LEAT, a spherical scanning set up has been developed in collaboration with Near-field Systems Inc. (NSI) for mmWave applications. This set up uses a stable robotic positioning mechanism to scan over the sphere enclosing the AUT in the center. Post-processing, like radial correction and Maximum Radial Extent (MRE), and Mathematical Absorber Reflection Suppression (MARS) filtering technique are extensively utilized to achieve far-field transformation from near-field measurement.

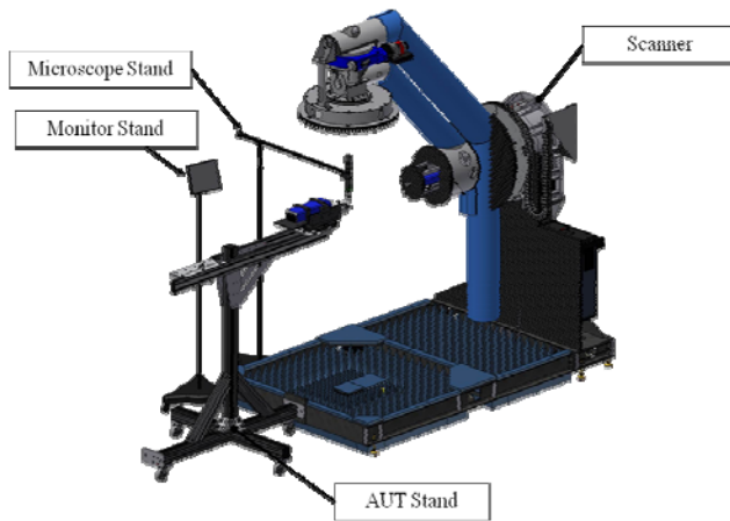


FIGURE 5.4: 3D spherical scanner in LEAT.

The previously discussed parts have shown the challenges of antenna design and measurement at mmWave. The objective of this work is to propose different array designs, that are suitable for hybrid architecture in both UE and gNB. The designs are highly integrate-able applying PCB-based technology and different concerns related to managing return currents, housing, and material are evaluated.

Different measurement campaigns have been done in this study in both far-field by using an anechoic chamber and in near-field using an NSI 3D scanner. The result shows comparable performances in terms of the radiation pattern. One campaign was to check the effect of a human finger on the UE antenna array at mmWave. A follow-up work studies the beamforming capabilities of a 4-element array in a smartphone at 26 GHz. The rest of this Chapter will go into details about those works.

5.2.2 Coverage efficiency - Figure of merit

As stated in [103], conventional parameters like total radiated power (TRP) or total isotropic sensitivity (TIS) are less effective in characterizing the beam steering capability of a UE. In this work, the coverage efficiency is evaluated

as a figure-of-merit measuring the power radiated toward a specific direction [95], [96]. The metric is calculated from a synthesized beam pattern, or total scan gain pattern, and can be presented as a cumulative distribution function (CDF) of the gain threshold (Figure 5.11, blue curves).

A previous Sub-section introduces the 3GPP spherical coverage parameter that is now being required in many conformance tests. The coverage efficiency is related to this by a shift with input power, as in equation 5.1.

$$\text{Spherical Coverage} = \text{Coverage Efficiency} \times \text{Input Transmitted Power.} \quad (5.1)$$

That explains why spherical coverage evaluating EIRP in dBm and coverage efficiency works on gains/directivity in dBi. The coverage efficiency is defined in [98] as following.

$$\eta_C = \frac{\text{Coverage Solid Angle}}{\text{Maximum Solid Angle}} = \frac{\Omega_C}{\Omega_0}. \quad (5.2)$$

in which

$$\Omega_C = \int_{\Omega_0} h(G_{TS}) d\Omega. \quad (5.3)$$

and

$$h(G_{TS}) = \begin{cases} 1 & \text{if } G_{TS} \geq G_{min} \\ 0 & \text{if } G_{TS} < G_{min} \end{cases}. \quad (5.4)$$

where Ω_C is the spherical coverage where the signal strength is better than a certain gain threshold. Ω_0 is the total spherical coverage, i.e. 4π steradians. The coverage efficiency graph is presented as a CDF with a gain sweep.

The antenna array is designed using HFSS and its prototype was measured using the NSI 3D scanner setup. Theoretically, beamforming is calculated by using field gain. The antenna power gain is a scalar parameter and it does not contain the phase. Due to the exported data differences, the

calculations are adapted for simulation and measurement. While the TSP is calculated from E-field gain for simulation, it can be directly calculated from power gain from the output of measurements.

The simulation TSP is calculated as follows.

$$G_{TS}^{sim}(\phi, \theta) = \frac{2\pi}{\eta \times \sum P_{kin}} \times \max_{\{X\}} \left(\sum |E_k(\phi, \theta)|^2 \times \exp(-i(\alpha_{kx} + \beta_k)) \right). \quad (5.5)$$

where α_{kx} is a phase-shift applied to the element k from vector X containing all possible phase-shift values, $\beta_k = \text{phase}(E_k(\phi, \theta))$, η is the impedance of the vacuum. $E_k(\phi, \theta)$ is exported from HFSS simulation, where k is the element index. A 3D matrix $E_k(\phi, \theta, f)$, where f is the frequency sweep, can also be used to check the variation of the coverage efficiency within a band of interest. In addition, G_{TS}^{sim} has to be normalized to the total input power of the array antenna, i.e. $\sum P_{kin}$ (Watt).

The measurement TSP can be calculated in (5.6). Different from the simulation output, the measured gain patterns are obtained as power value $G_k(\phi, \theta)$ (dBm). It contains the phases of E-field so that the TSP can be calculated directly without transformation. It still needs to be normalized by the measurement setup gain.

$$G_{TS}^{meas}(\phi, \theta) = \frac{1}{n \times G^{meas}} \times \max_{\{X\}} \left(\sum G_k(\phi, \theta) \times \exp(-i\alpha_{kx}) \right). \quad (5.6)$$

where G^{meas} is the gain of the measurement setup and n is the number of array elements.

Notice that the isolation term is omitted from the equations for arrays with high isolation, although the correctness of the calculations can be compromised. Function $\max_{\{X\}}(A)$ maximizes A over all possible phase-shift vectors X . For arrays with a small number of elements, this can be the exhaustive search function. Nevertheless, for larger number element arrays, an

optimization needs to be adopted to calculate the TSP.

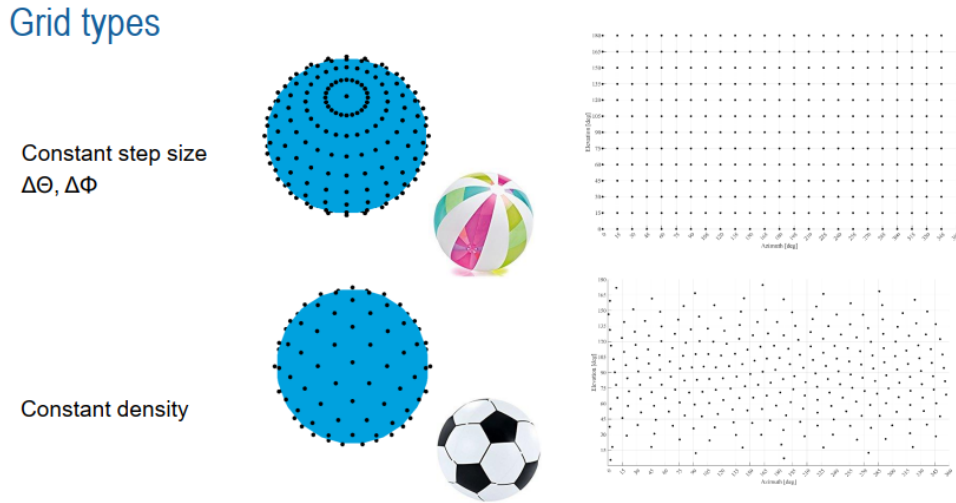


FIGURE 5.5: Grid types in pattern measurements, courtesy of Rohde & Schwarz [104].

Interestingly, to address the ratio in Equation 5.2, 3GPP has proposed two radiation pattern measurement grid types as in Figure 5.5. On one hand, the constant step size ($\Delta\phi, \Delta\theta$) is conventional, easy to realize, and for most polar calculations. When stretching the surface of the sphere to a 2D plot (the one on the top right of the Figure), the distance between every two adjacent neighbor points is constant in ϕ and θ . This case, $d\Omega = \sin\theta d\theta d\phi$

On the other hand, the constant density scheme has a constant distance between every two adjacent neighbor points on the sphere. The points on the sphere can be distributed by a different method, such as sampling using a charged particle system or spiral sampling. These points do not need coordination, an indexing can be sufficient. This configuration is unprecedented but useful for statistical measurements where exact positioning is not required. In this case, $d\Omega = \frac{4\pi}{N}$, where N is the number of distributed points.

An attempt has been done to quantify the differences in using different measurement schemes. Due to the lack of equipment in the laboratory which can produce constant density grid data, the measurement data in a constant step size grid is converted into constant density type. The conversion is done

by averaging out the values of four blue points in the first configuration to get the value of the red point being enclosed in the second configuration. A demonstration is shown in the Figure 5.6.

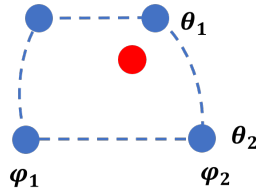


FIGURE 5.6: Constant step size to constant density grid types conversion.

A good agreement in coverage efficiency has been seen between data before and after converted. This can be a secondary approach to address coverage efficiency.

5.3 Human finger's effects on broadside array antenna

This part of the study resolves for the first time shed lights on radiation performance of antenna arrays for UE at mmWave *experimentally* in the presence of casing and finger. This is made possible by using the near-field three-axis spherical measurement setup of an antenna array [91]. Effects of real human's fingers on radiation characteristics of an antenna array are studied through spherical coverage where beamforming is incorporated.

5.3.1 Antenna, case and human's finger models

The previous antenna model using aperture coupled with is used in this study. For the sack of clearness (and for the length of this thesis), the antenna description is briefly given again as following. The antenna element constituting the array is based on the aperture-coupled structure first introduced in [85]. Taking into account the possibility of a later all-in integration,

this design is realized with multiple dielectric and conductive layers based on industrial PCB stack-up as illustrated in Figure 5.7a) and b). PCB technology gives antenna designers advances in the industrial automatic procedure with high precision and mass fabrication availability. From top to bottom layers of the PCB, the three substrate materials are RO4350 ($\epsilon_r = 3.66$), prepreg 2116 ($\epsilon_r = 3.96$) and RO4350 with 0.254 mm, 0.48 mm, and 0.254 mm thick, respectively, where ϵ_r denotes relative permittivity. All copper layers are 18 μm thick. The design consists of three slots S_1 , S_2 and S_3 cut in the three upper conductive layers of dimensions $5.4 \times 0.4 \text{ mm}^2$, $5.4 \times 0.4 \text{ mm}^2$ and $5.6 \times 1 \text{ mm}^2$. A 3-mm open-ended stepped-size stub is put in the lowest conductive layer below the slots to excite an electromagnetic wave through the dielectric layers. A $4 \times 4 \text{ mm}^2$ patch is placed 2 mm above the upper slot introducing an additional resonance. This allows the single element bandwidth and gain to be increased. The single-element $S_{11} \leq -10 \text{ dB}$ impedance bandwidth is from 24.25 to 27.5 GHz, thus covering the 5G NR FR2 band in Europe. A linear array with 4 elements is numerically modeled for optimization as depicted in Figure 5.7c) and d). The distance between every two neighboring elements is $0.7\lambda_0$, where λ_0 being the wavelength in free-space at 26 GHz. Antenna elements are isolated from each other by a rectangular cavity made of vias in each element as shown in Figure 5.7a), where the distance between two nearby vias is 1.5 mm.

In addition to the antenna array, the casing and the finger are also modeled. The casing is made of Acrylonitrile Butadiene Styrene (ABS), a commonly-used material for 3D printing with $\epsilon_r = 2.5$. Its volume covers $50 \times 100 \times 10 \text{ mm}^3$ and the thickness is 1 mm for all the surfaces. The surface of the casing towards the $-y$ direction is modeled as a finite conductivity sheet, representing the handheld terminal screen. A model of the finger is also added. Interestingly, the human skin at higher frequencies has higher conductivity and lower permittivity, which leads to a lower penetration depth of around 1 mm

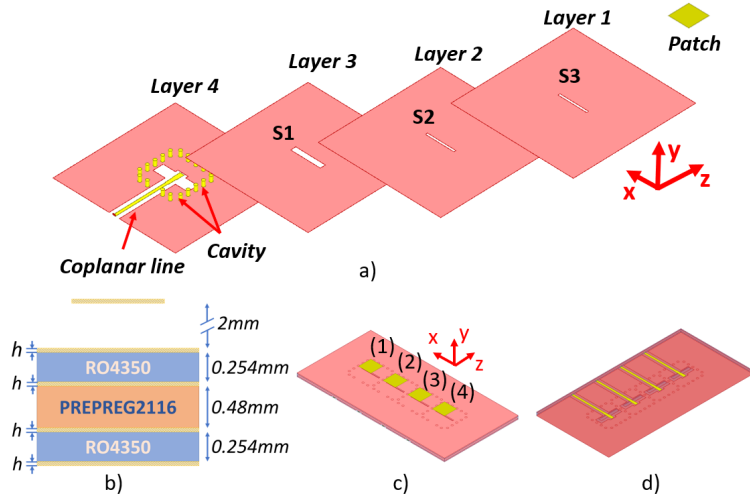


FIGURE 5.7: Single element antenna structure. a) Separated views of different layers of the design. b) Substrate specifications and patch. c) Top view with array element placements. d) Bottom view.

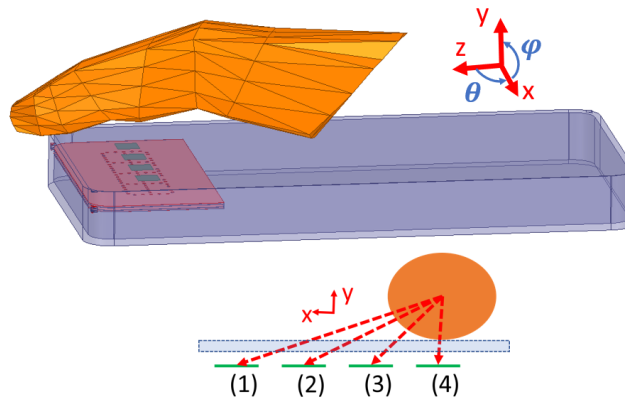


FIGURE 5.8: The simulation of array antenna with casing and finger (top) and the illustration of distances and angular positions of coverage of the finger to array elements (bottom).

[105]. Thanks to this feature, it is sufficient to consider an electrically homogeneous simulation model of a human body at mmWave representing only the skin. The finger is created with homogeneous properties with $\epsilon_r = 17.71$ and conductivity $\sigma = 24.41$ S/m which are extracted from Gabriel model of dry skin at 26 GHz [106]. The antenna array is positioned with respect to the casing and the finger as shown in Figure 5.8. The minimum distance between the antennas and the casing is 0.6 mm. The finger is outside the casing tilted by 12° with respect to the z -axis on xOz plane and being centered above the fourth element.

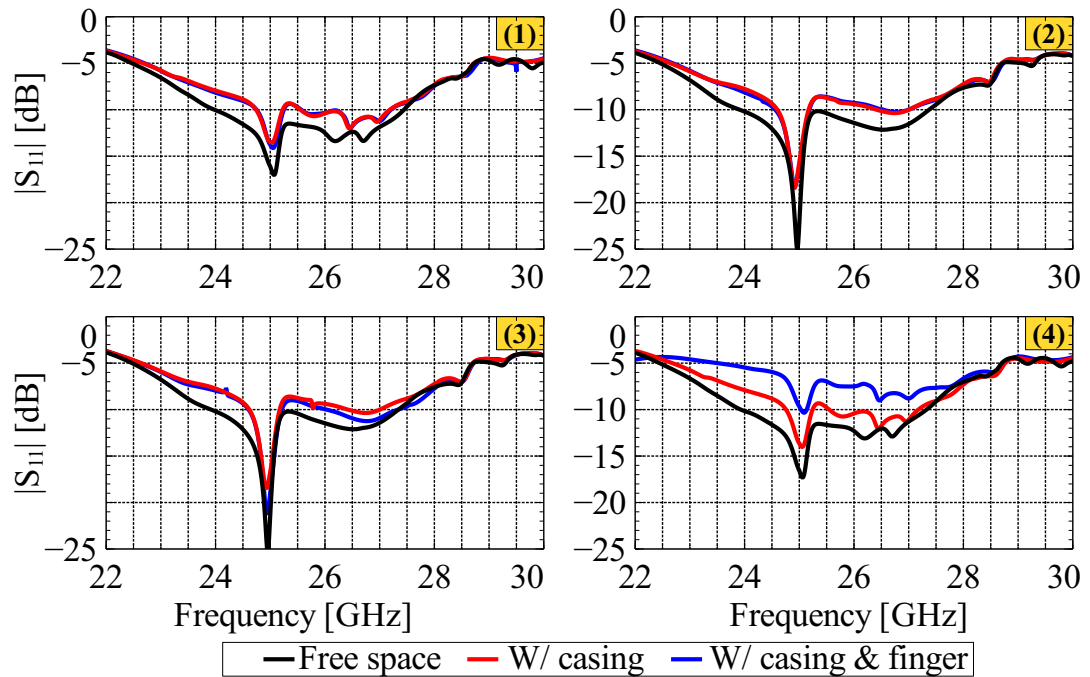


FIGURE 5.9: Reflection coefficients of single-antenna elements.

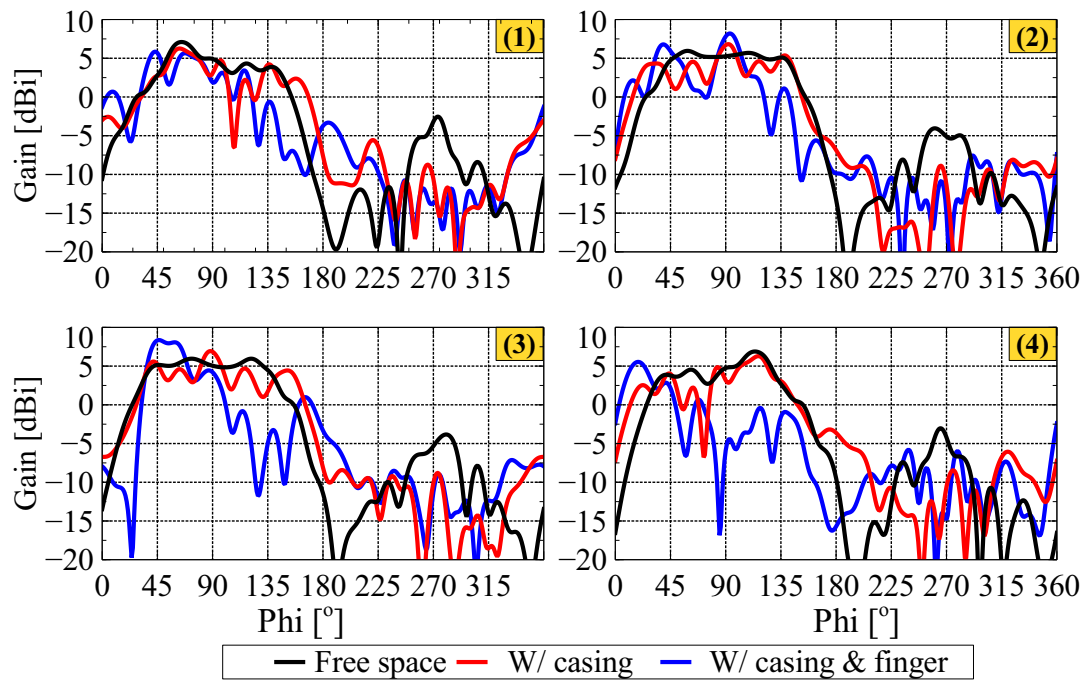


FIGURE 5.10: Simulated realized gains of single-antenna elements at 26 GHz on azimuth plane.

5.3.2 Effects on matching and realized gains in simulations

Figure 5.9 illustrates the impedance matching of all the array elements with the presence and absence of a finger and casing. All the elements achieve $|S_{11}| \leq -10$ dB reflection coefficient over the band of interest in free-space.

The casing causes a worse matching, with the maximum $|S_{11}|$ increased up to -7.5 dB in the same band, as shown in the red curve. All the array elements equally suffer from this effect. The presence of the finger, on the contrary, causes the worsening of the impedance matching only on the fourth element, i.e., the one closer to the finger. However, the $|S_{11}|$ is still lower than -6 dB, which is acceptable for UE antennas. Besides, the isolation between elements is also impacted, where the worst isolation is 23 dB in free space, 18 dB with the casing, and 15 dB with the casing and finger.

As mentioned in sub-Section 5.2.1, any object inside the near-field region will impact not only the impedance matching but also the gains of the antenna elements. As shown in Figure 5.10, all the elements have a simulated realized gain higher than 5 dB and a half-gain beamwidth wider than 70° , centered at $\phi = 90^\circ$. By adding the casing, the gain patterns of all the elements fluctuate. There are even some blind angles at around $\phi = 102^\circ$ and $\phi = 78^\circ$, where 8 dB of attenuation is observable, for the first and fourth elements, respectively, probably caused by the scattering of the waves on the casing. The effect of the presence of the finger in terms of antenna gains can be clearly seen in Figure 5.10 on the blue curves. The constructive and destructive interference due to the scattering from the finger surface can be observed on the radiation pattern as a lower main lobe and higher sidelobe levels. For example, there is attenuation in the best/worst case of 7/20 dB within $120^\circ \leq \phi \leq 150^\circ$ for the gain of the third element, while 4 dB is added up at $\phi = 50^\circ$. The same effects are reported by simulations in [19] at both 28 GHz and 60 GHz. At 28 GHz, the levels of attenuation and increase in radiation to side and back angles agree well with this work.

Each antenna element is assumed to be fed with a 5-bit phase-shifter, which supports 11.25° phase step. Starting from the gain patterns of antenna elements in the array, beam patterns of the array are synthesized by applying all the possible phase shifts to the element gain patterns and successively

summing up all the resulting vector pattern configurations, as reported in [7].

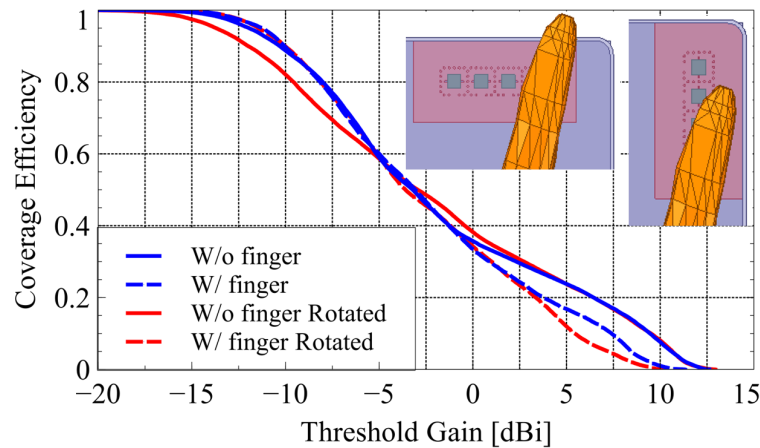


FIGURE 5.11: Simulated coverage efficiencies for two different orientations of the patch array (to study the impact of the finger in two orthogonal polarization cases).

In order to analyze the effect of the finger also in the orthogonal polarization case, the model in which the patch array is rotated to be perpendicular to the shorter edge of the mobile terminal has been simulated. The results are added to Figure 5.11 in red. As it can be noticed, the finger gives almost similar losses at gain thresholds higher than 0 dBi for both polarization, though there are some small differences in term of gain level. These losses can be as high as 3 dB in the first-mentioned case and 5 dB in the rotated case.

5.3.3 Experimental evaluation of the effects on single elements

The prototype has been realized as in Figure 5.12 with the casing designed in HFSS and printed by a 3D printer. A metal plate is placed on one face of the casing to replicate the screen. The array is at the top of the casing, facing toward the non-metaleed face. Finally, the connectors direct their output toward the bottom of the casing where there are some open holes.

The effects of the user's finger on the antenna gain have been experimentally evaluated. The gain measurements have been performed for a single frequency at 26 GHz where the measured $|S_{11}|$ is lower than -9 dB for all



FIGURE 5.12: The simplified mobile phone prototype with antenna array and casing.

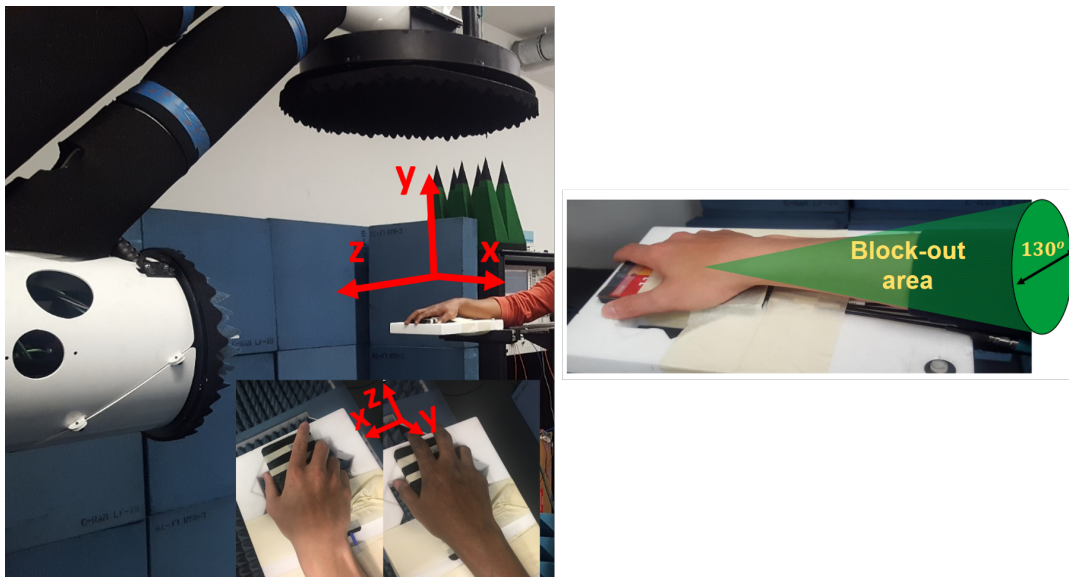


FIGURE 5.13: Left figure: Radiation measurement with real human's hand using spherical scanner. 1-finger (left) and 2-finger (right) configurations are represented in the small figure at the bottom. Right figure: Block-out area in measurements.

the elements. A three-axis spherical near field scanner is used to enable measurements with a human being. In this setup, a robot arm moves the probe over the surface of a sphere centered on a fixed DUT. This mechanism allows a person to place his/her hand over the DUT during the measurement, as shown in Figure 5.13 and previously reported in [107], [108].

The antenna gain is first measured in free space with casing for $-135^\circ \leq \theta \leq 135^\circ$ due to DUT holder blockage like in Figure 5.13 on the right. Two typical finger placements on the casing have been chosen for the measurements. In the first one, the finger mimics the position of the finger used in

simulations. The index finger is covering the fourth element. The second case is chosen to illustrate a user covering the antenna array with two fingers. In this case, the index finger is placed between the first and the second element, while the middle finger covers the fourth element.

Figure 5.14 shows the realized gains of each antenna element, where the i^{th} row corresponds to element i . The first, second, and third columns in the figure correspond to cases without the hand, with one finger, and with two fingers, respectively. Because the maximum radiation of each element is in the direction at $\theta = 90^\circ, \phi = 90^\circ$, the polar angular range is limited to $60^\circ \leq \theta \leq 120^\circ$ in the plot. Take a closer look at the xOy plane cut, i.e. $\theta = 90^\circ$, the effect of the finger in the one-finger case is clearly observable on the fourth antenna element. The realized gain suffers from stronger distortion while the remaining elements of this case are less affected by the presence of the finger, confirming the numerical results. In the two-fingers case, the appearance of reflected and diffracted fields from the fingers can be seen in side and back angles. The radiation from elements 1, 2, and 4 is reduced and the third element still maintains gain levels as in free-space.

5.3.4 Beamforming and coverage efficiency of the array

The design is simulated and fabricated as illustrated in Figure 4.23 of the previous Chapter. A brief remind is the mmWave array antenna works at the 5G n258 band. It is constituted by four patch elements on a four-layer substrate PCB. The prototype has been measured with different finger configurations using the NSI 3D spherical scanner, as in Figure 5.13.

Figure 5.16 shows the CDFs of all simulation and measurement finger configurations. It can be seen that the coverage efficiency CDF is a simpler and better illustration of the beam scanning pattern when it comes to statistical characterization. The figure shows the similarities between simulations

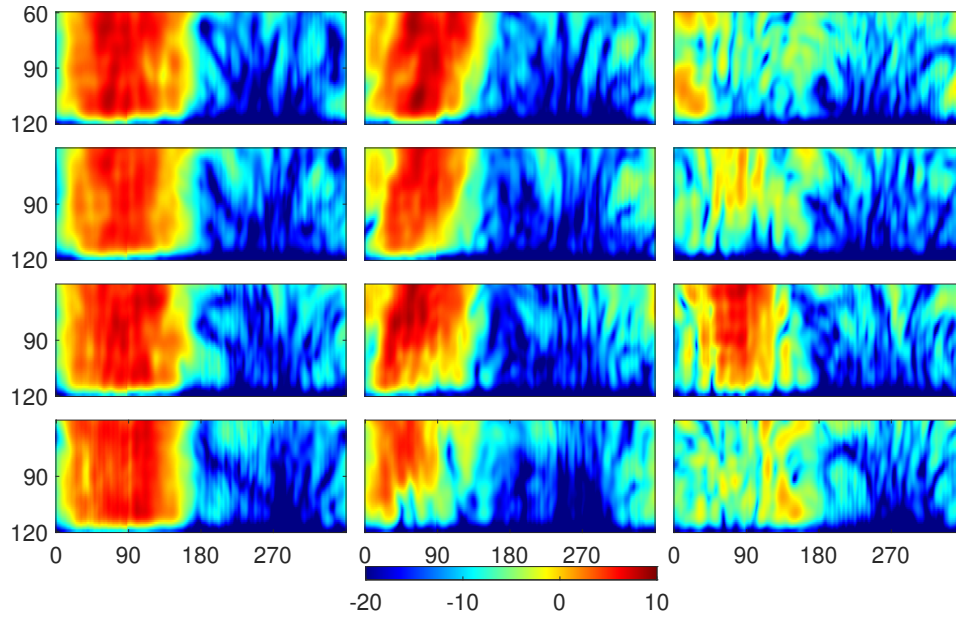


FIGURE 5.14: Realized gains of each antenna element in the array for three cases of finger intervention. In each sub-figure, θ and ϕ [°] are shown in vertical and horizontal directions, respectively.

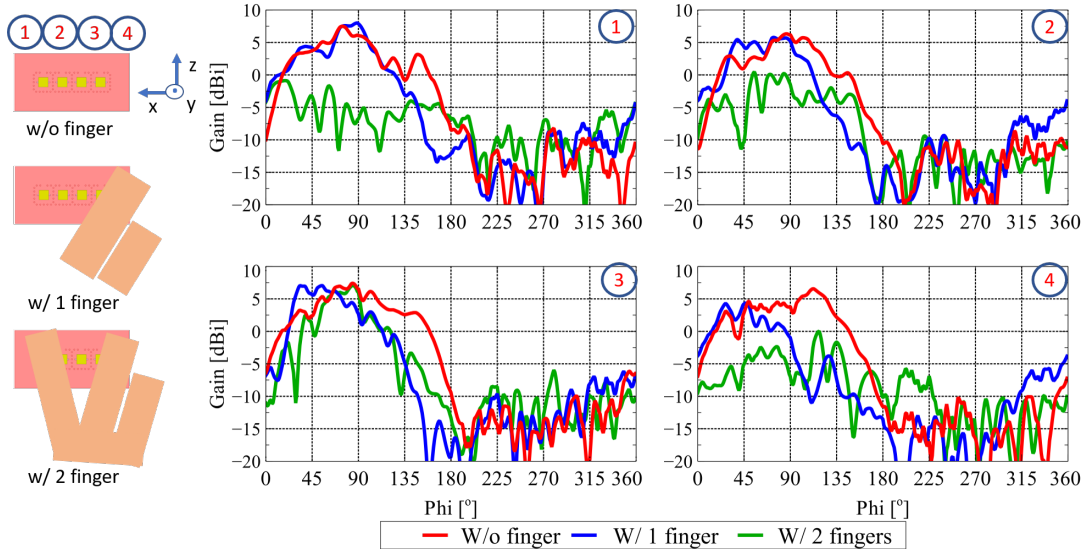


FIGURE 5.15: Measured gains of single elements in azimuth plane in different cases. Elements' order is from left to right, top to bottom.

and measurements for high gain thresholds until $CDF = 50\%$ or for an array gain higher than -5 dBi threshold gain. Below this level, however, there is a difference.

This difference can be explained by the block-out area in measurement. To evaluate this, the effective angle of the blockage angle is calculated as

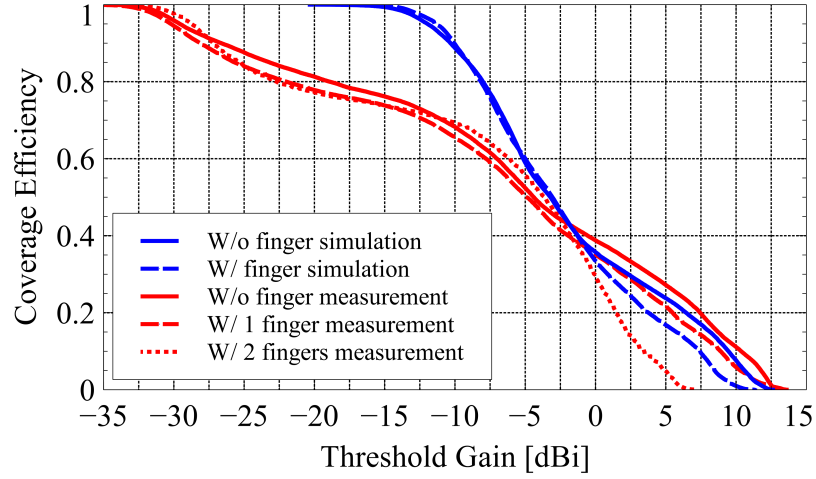


FIGURE 5.16: Coverage efficiencies in simulations and measurements.

follows.

$$\Omega_{blockout} = \int_0^{2\pi} \int_{\alpha}^{\pi} \sin \theta d\theta d\phi. \quad (5.7)$$

where α is the angle where the blockage starts to affect the pattern. For example, if $\alpha = 65^\circ$ like in the Figure 5.17. The blockage angle covers 28.87% of the sphere. This does not seem to account for the whole difference where $CDF = 0.5$, or 50% area of difference. It can be explained that this 28.87% low angle gain takes place of another 28.87% place of other higher gain, so it accounts for 57.74% area of difference. For the best correctness, the block-out region from simulation can be replaced by the same region in a simulation like in Figure 5.17 top. The block-out area is replaced partially with $\alpha = (35^\circ, 50^\circ, 60^\circ, 80^\circ)$. The top-left figure is where $\alpha = 80^\circ$, meaning total replacement of the block-out. It can be seen clearly from Figure 5.17 bottom the low gain area gradually disappears. Moreover, there are not many differences between 60° and 80° replacements. The CDF starts to be stable with big replacement because the results from measurement are close to simulation.

However, the closeness with the presence of a finger might not be worth trying and can affect the analysis. To evaluate the effectiveness in terms of

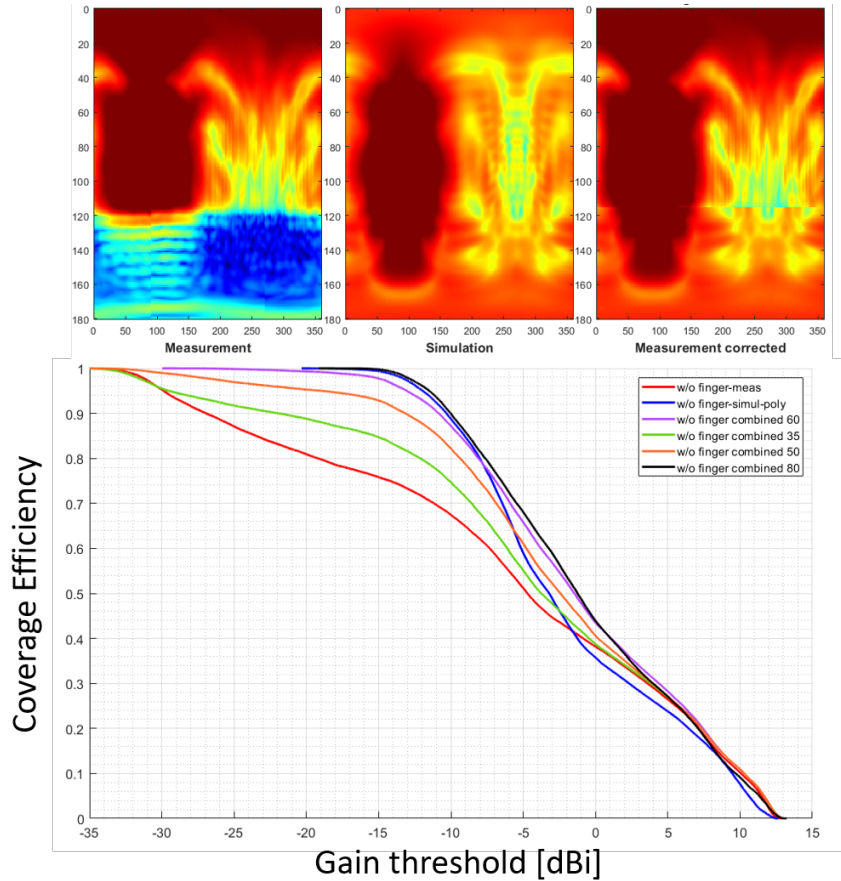


FIGURE 5.17: Replacing block-out area in measurement with simulation data in no-hand case.

power, I propose using the effective radiation power to evaluate the effectiveness of the spherical regions where the simulation CDF differs from the measurement CDF. This is the cumulative power radiating in the angles where the beamforming gain is higher than a certain threshold.

$$P_C = \int_{\Omega_0} G_{TS}(\Omega) \times h(G_{TS}) d\Omega. \quad (5.8)$$

where $h(G_{TS})$ is a step function defined in the previous section. The P_0 is the total radiated power, i.e. $G_{min} = \min(G_{TS})$. The ratio P_C/P_0 shows that more than 95% of radiated power radiates with a gain higher than -5 dB. Consequently, the reliability of the measurement is still affirmed, regardless of the difference in lower gain angles. Other concerns of the measurement have been discussed previously and in [1].

Figure 5.18 (left) illustrates the maximum gain of synthesized beam patterns over azimuth angles for the aforementioned three cases of finger intervention to the antenna array. The differences in the synthesized beam pattern in the azimuth plane are clearly observable.

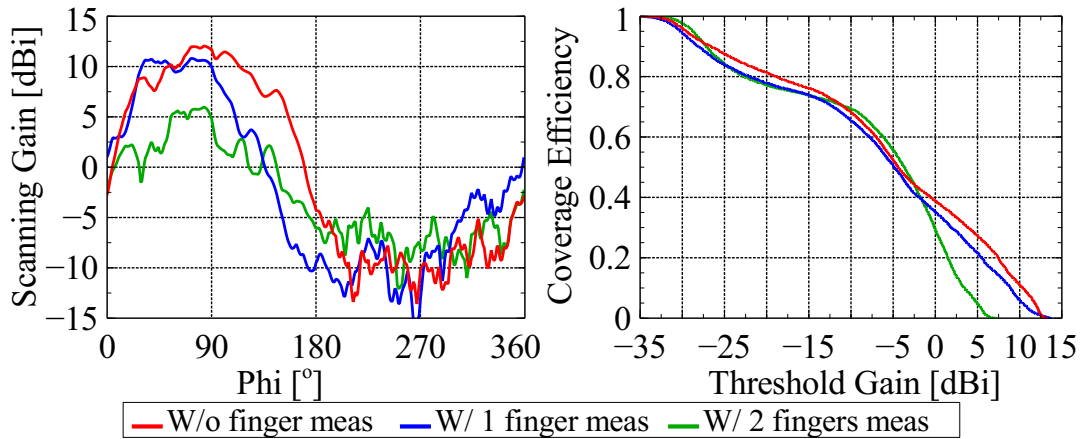


FIGURE 5.18: Maximum gain across azimuth angles (left) and coverage efficiency (right) of array antenna in different cases.

The estimated coverage efficiency at 26 GHz in Figure 5.18 (right) shows that the realized gain of the array in the one-finger case has a constant loss of up to 5 dB of gain compared to the case without the finger. Nevertheless, the achieved maximum gain is about 13 dBi in both cases. The measured gains of our antenna array with casing are in agreement with those reported in [77] using a similar antenna structure. The antenna array in this work, however, differs for the ABS material of the casing and the thickness of the structure.

In the two-finger case, the maximum gain reduces to about 6 dBi, similarly to the gain when only one element is activated, indicating that almost no beamforming gain is obtained. Only the third element, i.e., the one not being covered by the fingers, is effectively contributing to the radiation.

Additional studies have also been done to evaluate different effects from some main parameters of the design as shown in Figure 5.19. Very similar results are obtained at different frequencies within the 24 – 28 GHz band. The maximum variation of the threshold gain over the entire band is ± 1.5 dBi. Furthermore, since glass is widely used as a smartphone cover material,

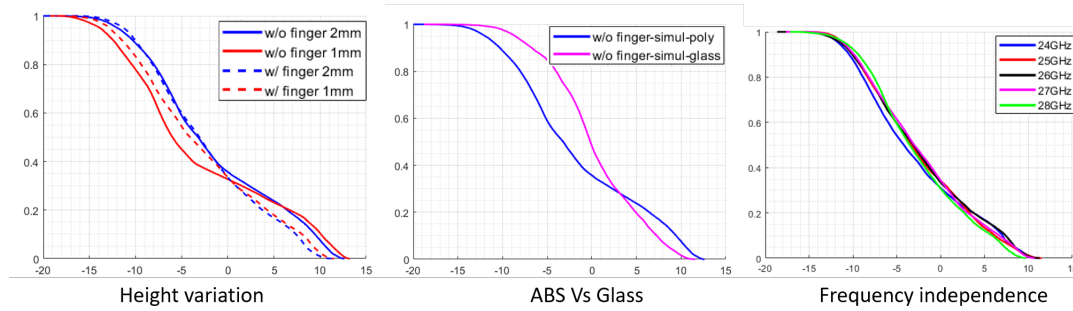


FIGURE 5.19: Studying the effects of changing patch height (left), material (middle) and frequency (right) on coverage efficiency.

the spherical coverage efficiency with finger effect using an industrial glass casing with $\epsilon_r = 6.84$ [109] at 26 GHz and 1 mm thickness has been simulated. The higher permittivity of glass is inducing more scattering. Coverage efficiency for gain threshold higher than 5 dBi is reduced by 67% compared to ABS.

5.4 Human finger's effects on end-fire array antenna

The same measures of the human finger's effect are performed on the presented end-fire array. The prototype of the casing is built with the same process using a 3D printer as ABS material. Nevertheless, in this measurement, there are two arrays at different corners of the casing as in Figure 5.22. This configuration allows checking MIMO performance against the blockage by switching between the arrays.

The hand is placed in screen mode with the index finger touch the surface of the top array (array 2) and covers a portion of the main direction. The human thumb covers a bigger portion in the main direction of array 1. The block-out area still exists in the pattern, resulting in a low-gain spherical zone. This zone is noticeable in Figure 5.21 as blue areas. Finally, the analysis of this measurement is on normalized gain for the sack of simplicity.

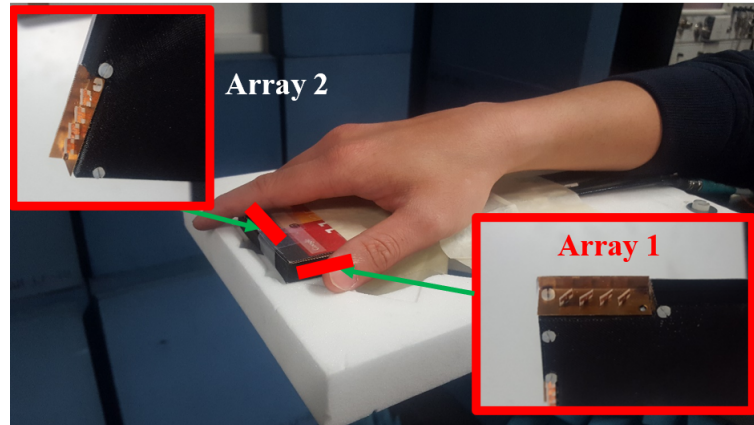
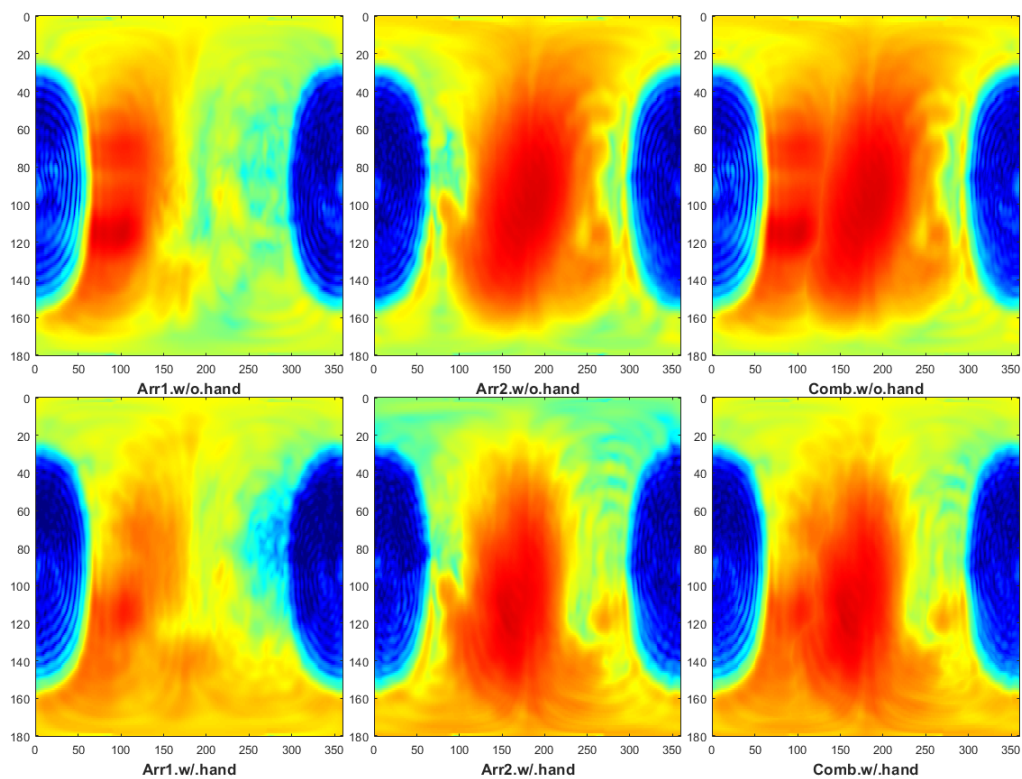


FIGURE 5.20: Measurement of finger effect on end-fire array

FIGURE 5.21: Blockage effect on end-fire array, vertical axis is ϕ and horizontal axis is θ .

From Figure 5.21, array 1 is apparently affected more severely because the human thumb almost covers 2 elements to the bottom. Meanwhile, the waves are reflected in different directions, giving again an average-out effect that causes a higher coverage at the low gain region. The pattern of array 2 is not as altered. The radiation at the main end-fire direction is almost unscathed. However, the radiation to $\theta = 0^\circ$ is blocked. It is reflected in the

$\theta = 180^\circ$ direction. It is worth noted also that the shape of the block-out area in this measurement results is not the same as the one in broadside antenna measurement. It is because the orientation of the antenna is changed, the coordinate is also changed from (ϕ, θ) to $(azimuth, elevation)$. Concretely, the coordinate experiences a rotation -90° along $x - axis$, where the transformation matrix is as follows.

$$R = \begin{bmatrix} 1 & 0 & 0 \\ 0 & 0 & 1 \\ 0 & -1 & 0 \end{bmatrix} \quad (5.9)$$

This feature of the NSI setup helps to keep the main beam being on the equator of the sphere where $\theta = 90^\circ$ as the broadside array, hence matching better the comparisons.

The same results in terms of coverage efficiency have been obtained with the presented end-fire array, as illustrated in Figure 5.22. The coverage of the two arrays is slightly different since array 1 radiates more effectively than array 2. The CDF of array 1 is shifted to the right of the CDF of array 2. It can be explained by the block-out area where a portion of the radiation of array 1 is loosed. In the presence of the user's hand, there is a big drop in coverage at -10 dB to 0 dB threshold range for array 1. Its coverage efficiency has a similar pattern to the one with 2 fingers case in the broadside array study. Meanwhile, from -20 dBi to -11 dBi range, the gain seems to be improved. On the other hand, array 2 experiences a constant loss of $2 - 5$ dB for every coverage level up to 70%. This well resembles the case with one finger in the broadside array measurement, where no severe damage has been affected to the array's radiation. This demonstrates that the position of the hand on the terminal, and consequently the number of array elements that are covered by the fingers, are more important than the geometry of the array element itself.

The MIMO capability is demonstrated in the combined CDF. Simply put,

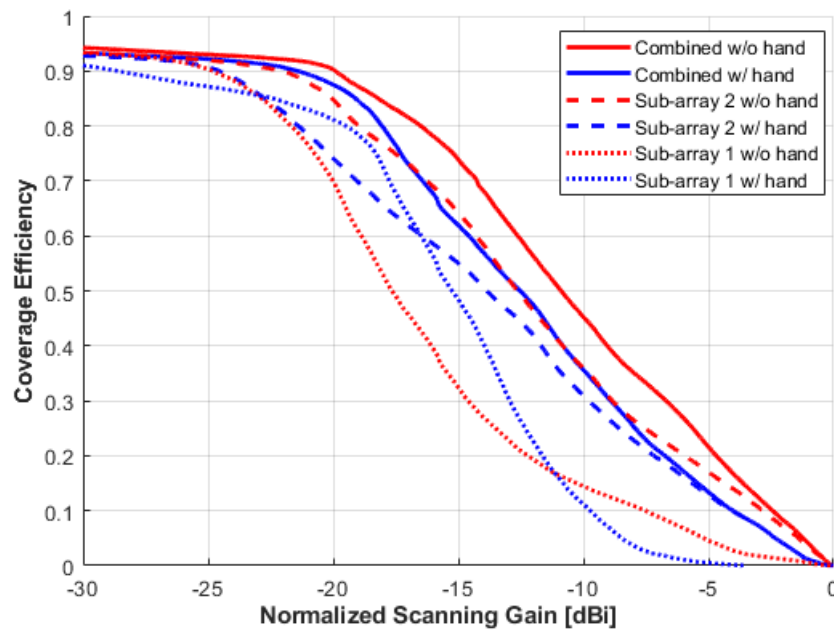


FIGURE 5.22: Coverage efficiency CDF of array 1, array 2 and the combined patterns from the left to the right; the top figures are without user's hand and the bottom ones are with hand.

with two arrays at two different positions pointing its patterns to different directions, there is a greater chance that not all radiation from all sub-arrays are blocked. The transceiver can switch on-off among them in order to maximize the received/ transmitted signal. It can be seen that there is much better coverage of the combined with/without hand patterns at the far-right sub-figures in Figure 5.21. The CDF of the gain pattern without hand translates that into a shift around 2 – 3 dB to the right of the CDF of array 2. In the presence of blockage, the CDF of the combined pattern looks closely like the CDF of array 2 as it contributes the main radiation whereas the radiation from array 1 compromises the low gain area of the pattern of array 2.

5.5 Conclusion

In this chapter, the near-field effects of the user's finger on the performance of a 5G mobile terminal antenna working in the European 5G NR band at 26

GHz (band n258) have been experimentally evaluated. Measurements have shown that the single-element antenna gain can be reduced up to 20 dB in certain directions because of the shadowing from the user's finger. However, the array is still able to maintain the spherical coverage efficiency using beamforming in the one-finger case. In the two-finger case, the realized gains are severely reduced even with beamforming, thus causing a strong reduction of the radio link performance. The same results have been obtained by substituting the broadside antenna array considered in this paper with the end-fire array presented in [7]. This demonstrates that the position of the hand on the terminal, and consequently the number of array elements that are covered by the fingers, are more important than the geometry of the array element itself. Implementing sub-arrays at different positions as in Section 5.4 is a necessary solution to mitigate finger shadowing effects and to increase the coverage.

Chapter 6

Conclusion

Since 3GPP started to work on 5G properties, there have been several successes. The world is moving to a deployment phase of 5G. The novel technology promises many new services with its awesome performances in terms of data rate, latency, reliability, etc. This thesis aims at solving some of the problems in antenna systems at both 5G FR1 and FR2. This includes designing multi-band antennas at the sub-6GHz and human blockage in mmWave.

In Chapter 2, Q-Factor is adopted as a figure of merit to evaluate the bandwidth limitation in different situations of antenna size constrain. The realization of the calculation is based on the close resemblance of stored energies to the EFIE in MoM. The polarizability nature of miniature antennas is verified for a $30 \times 50 \text{ mm}^2$ terminal by maximizing its directivity in different directions with respect to different polarizations. Interestingly, different kinds of radiation patterns can be obtained. This chapter later concentrates on studying the limitation of bandwidth of mobile antenna on a terminal that leaves relatively narrow ground clearance for the antenna's placement. It is shown that the antenna can lose up to 50% bandwidth if the clearance is to be reduced from 6 mm width to zero.

The reasoning of Chapter 3 bases on the previous analysis of bandwidth

limitation on narrow clearance mobile phone antennas. The Chapter proposes a methodology using the PSO algorithm to optimize NCE antenna geometries and its associated matching networks. The proposal solution undergoes different tests. In the first and second designs, the clearance is still 0mm wide. While the first one is to optimize a simple 2-element single band design for sub-GHz bands, the second design adds the band 1.7 – 2.7 GHz for the optimization. The result shows that both are achievable. The 2 elements of the second design can be merged or separate, hence providing different options strategy for designers.

The final test in this Chapter to design 3-elements triple bands antennas that can cover most of the 5G sub-6GHz bands with a 3 mm clearance width. The constraints are relaxed so that the PSO algorithm can converge. The design proves effective numerically. In experimental results, the filtering of each band is clear though there is still a 3 dB drop at 2.1 GHz of a middle band and around 3 dB lower than expected of high band.

Chapter 4 moves to mmWave and analyzes the array designs at this frequency band. In this Chapter, two feeding methods are analyzed and adopted for patch antenna design. Each has its own pros and cons. In general, if the designs using the 2 feeding methods take the same volume and be sufficiently optimized, they have similar performances in terms of matching and radiating properties. Elemental designs easily cover band n258 5G. They have approximately 7 dBi gain and around –1 dB radiation loss.

An end-fire array at mmWave is also analyzed. This array is integrated in a mobile phone model to measure the radiations of separate elements. This is later synthesized as arrays to show that the total scanning pattern is less affected by a resolution higher than 90° of the phase-shifter. Instead, a coarse resolution, like 45° or 90° , can affect more on the nullification of the pattern. This should be noted if the array is to be used for a zero-forcing scheme.

The measurement campaign described in Chapter 5 utilizes the aperture

array of the previous Chapter. The array is integrated inside an ABS-material phone model. The measurements are conducted using the 3D spherical scanning robotic system available in LEAT. The system allows measuring in near-field and then numerically transforms the results to far-field. The main objective of this study is to quantify the loss of radiated energy if the user's finger is introduced in the proximity of the antenna. The advantage of using this near-field system is the ability to place a human hand without measuring the whole body effect, which distinguishes this study from others in literature and gives its scientific significance. Coverage efficiency in form of a CDF plot is adopted as a figure of merit for the evaluations.

This study demonstrates that placing a single finger over the array, considering the element distance of mmWave array, many of the radiators are still able to function with an insignificant loss around 7/20 dB loss in best/worst case for some elements. It is worth noting that there is up to 4 dB improvement thanks to reflections in some directions. In the presence of multiple fingers, on the other hand, multiple elements can be affected, and the radiation performance deteriorates severely. Different study cases with alternative finger positions, antenna orientations, antenna height are also verified showing similar effects.

A suggestive solution for this blockage problem is using multiple arrays placing at different places in the terminal. Two identical end-fire arrays are integrated orthogonally in a terminal. A substantial improvement of around 10% coverage efficiency is seen by enabling MIMO capability, even with one array is severely affected by the user's finger. All in all, intelligence in placement plays a pivotal role in obtaining a high-performance design.

In summary, this thesis covers a wide range of subjects from applications of theoretical limitations to antenna optimization methodology, from antenna design analysis to experimental measurements, then to evaluation of antenna

performance in real-life applications. It is also a continuation of previous scientific researches. For instance, the calculation of Q-factor in Chapter 2 is based on well-developed studies of KTH and Lund universities [32], [41], [42]. The methodology using the PSO algorithm in Chapter 3 is inspired by [59]. The works in Chapter 4 and Chapter 5 follow [91], [107]. In consequence, the works in this thesis can surely be developed further. Following are some interesting perspectives:

- The PSO algorithm can be developed further to be able to handle all types of optimization of antenna and associated matching circuits. It can be also user-friendly packaged, i.e. using GUI of Matlab, so that it is easier to be used by anyone.
- Design of antennas in 5G mmWave is rather simple in my opinion. However, it should be highly integrated-able with circuitry. One can find many works in literature for this, though I believe it still be an open subject to study knowing that there are various of applications for 5G and for IoT.
- The measurements in Chapter 5 provides a good base to analysis the effect of the user's fingers. Thus, a strategy for smart-placement of mmWave array antennas on mobile terminals is certainly necessary and can be helped by this. It can also be developed together with the PSO methodology when a total complicated antenna system with sub-6GHz and mmWave is to be built.

Finally, 5G roll-out is delayed by different reasons from the COVID-19 to the burning of 5G stations in the UK. I do still believe in the prosperity of the technology given its promising disruptive performances and the impressive collaborations of industry companies and scientific institutions worldwide. In Europe, many countries have already planned their 5G deployments in



FIGURE 6.1: OOKLA 5G roll-out map of Europe, accessed October 2nd 2020.

few years ahead as in Figure 6.1 [110]. The booming of technologies is undeniable and having positive impacts on human society for a long time to come. It is therefore always interesting to follow, and hopefully there will soon be some "dots" in France territory in the above Figure!

Bibliography

- [1] T. Q. K. Nguyen, M. S. Miah, L. Lizzi, K. Haneda, and F. Ferrero, "Experimental Evaluation of User's Finger Effects on a 5G Terminal Antenna Array at 26 GHz," *IEEE Antennas and Wireless Propagation Letters*, vol. 19, no. 6, pp. 892–896, 2020.
- [2] T. Q. K. Nguyen, I. Santamaria, L. Lizzi, and F. Ferrero, "Measurement of Finger Effects on Coverage Efficiency for User Equipment Mm-Wave Antenna," in *2020 IEEE International Symposium on Antennas and Propagation and North American Radio Science Meeting*, IEEE, Montreal, Canada, Jul. 2020, pp. 1–2. [Online]. Available: <https://hal.archives-ouvertes.fr/hal-02511917>.
- [3] K. Nguyen, F. Ferrero, and L. Lizzi, "Feeding Techniques for Multilayer PCB Mmwave Array Antenna for UE," in *2020 International Workshop on Antenna Technology (iWAT)*, 2020, pp. 1–4.
- [4] I. Santamaria, T. Q. K. Nguyen, L. Lizzi, F. Ferrero, and R. Staraj, "2-Port Antenna with Matching Network for Dual-band IoT Terminal," in *IEEE International Symposium on Antennas and Propagation and USNC-URSI Radio Science Meeting - AP-S/URSI 2019*, IEEE, Ed., Atlanta, Georgia, Jul. 2019. [Online]. Available: <https://hal.archives-ouvertes.fr/hal-02085949>.

- [5] L. Santamaria, T. Q. Khai Nguyen, F. Ferrero, R. Staraj, and L. Lizzi, "Flexible reconfigurable antenna robust to folding in wearable applications," in *2019 IEEE International Symposium on Antennas and Propagation and USNC-URSI Radio Science Meeting*, 2019, pp. 1–2.
- [6] T. Q. K. Nguyen, F. Ferrero, and L. Lizzi, "PSO-based Combined Antenna and Matching Network Optimization for Mobile Terminals," in *EuCAP 2019*, Krakow, Poland, Mar. 2019. [Online]. Available: <https://hal.archives-ouvertes.fr/hal-01963416>.
- [7] F. Ferrero, P. Ratajkzack, and T. Q. K. Nguyen, "Assessment of beamforming capabilities of a 4-element array in a smartphone at 26 GHz," in *12th European Conference on Antennas and Propagation (EuCAP 2018)*, 2018, pp. 1–3.
- [8] T. Q. Khai Nguyen, L. Lizzi, and F. Ferrero, "Dual-Matching for Single Resonance Miniaturized Antenna for IoT applications," in *2018 IEEE International Symposium on Antennas and Propagation USNC/URSI National Radio Science Meeting*, 2018, pp. 793–794.
- [9] L. H. Trinh, V. X. Bui, F. Ferrero, T. Q. K. Nguyen, and M. H. Le, "Signal propagation of LoRa technology using for smart building applications," in *2017 IEEE Conference on Antenna Measurements Applications (CAMA)*, 2017, pp. 381–384.
- [10] F. Ferrero, T. Q. K. Nguyen, and L. Lizzi, "Co-Optimisation antenne et circuit d'adaptation pour terminaux mobiles de nouvelle génération," in *JNM 2019 - 21èmes journées Nationales Micro-Ondes*, Caen, France, May 2019, pp. 1,4. [Online]. Available: <https://hal.archives-ouvertes.fr/hal-02070845>.
- [11] B. J. Hunt, "The Maxwellians," in. Cornell University Press, 1994, ISBN: 0801482348.

- [12] A. Schmid, *4G : Orange annonce une couverture de 99% de la population, comme SFR et Bouygues*, 2019 (accessed January, 2020). [Online]. Available: <https://www.phonandroid.com/4g-orange-annonce-une-couverture-de-99-de-la-population-comme-sfr-et-bouygues.html>.
- [13] 5G PPP, *5G Vision*. [Online]. Available: <https://5g-ppp.eu/wp-content/uploads/2015/02/5G-Vision-Brochure-v1.pdf>.
- [14] Nokia white paper, *5G Releases 16 and 17 in 3GPP*. [Online]. Available: <https://www.nokia.com>.
- [15] T. S. Rappaport, S. Sun, R. Mayzus, H. Zhao, Y. Azar, K. Wang, G. N. Wong, J. K. Schulz, M. Samimi, and F. Gutierrez, "Millimeter Wave Mobile Communications for 5G Cellular: It Will Work!" *IEEE Access*, vol. 1, pp. 335–349, 2013, ISSN: 2169-3536. DOI: [10.1109/ACCESS.2013.2260813](https://doi.org/10.1109/ACCESS.2013.2260813).
- [16] E. Björnson, L. Sanguinetti, H. Wymeersch, J. Hoydis, and T. L. Marzetta, *Massive MIMO is a Reality – What is Next? Five Promising Research Directions for Antenna Arrays*, 2019. arXiv: [1902.07678](https://arxiv.org/abs/1902.07678) [eess.SP].
- [17] K. Zhao, J. Helander, D. Sjöberg, S. He, T. Bolin, and Z. Ying, "User Body Effect on Phased Array in User Equipment for 5G mm Wave Communication System," *IEEE Antennas and Wireless Propagation Letters*, vol. PP, pp. 1–1, Sep. 2016. DOI: [10.1109/LAWP.2016.2611674](https://doi.org/10.1109/LAWP.2016.2611674).
- [18] I. Syrytsin, S. Zhang, G. F. Pedersen, K. Zhao, T. Bolin, and Z. Ying, "Statistical Investigation of the User Effects on Mobile Terminal Antennas for 5G Applications," *IEEE Transactions on Antennas and Propagation*, vol. 65, no. 12, pp. 6596–6605, 2017.
- [19] M. Heino, C. Icheln, and K. Haneda, "Self-user shadowing effects of millimeter-wave mobile phone antennas in a browsing mode," in *2019*

- 13th European Conference on Antennas and Propagation (EuCAP), 2019, pp. 1–5.
- [20] D. B. Davidson, *Computational Electromagnetics for RF and Microwave Engineering*, 2nd ed. Cambridge University Press, 2010. DOI: [10.1017/CB09780511778117](https://doi.org/10.1017/CB09780511778117).
- [21] S. N. Makarov, *Antenna and EM Modeling with MATLAB*, 1st ed. Wiley, 2002. DOI: [978-0-471-21876-0](https://doi.org/10.1002/978-0-471-21876-0).
- [22] *European School of Antenna - Antennas and Rectennas for IoT Applications*, 2019. [Online]. Available: <http://web.univ-cotedazur.fr/events/aria2019>.
- [23] L. Gürel, K. Sertel, and K. Şendur, “On the choice of basis functions to model surface electric current densities in computational electromagnetics,” *Radio Science*, vol. 34, no. 6, pp. 1373–1387, 1999.
- [24] M. F. Catedra, J. G. Cuevas, and L. Nuno, “A scheme to analyze conducting plates of resonant size using the conjugate-gradient method and the fast Fourier transform,” *IEEE Transactions on Antennas and Propagation*, vol. 36, no. 12, pp. 1744–1752, 1988.
- [25] O. Brune, “Synthesis of a finite two-terminal network whose driving-point impedance is a prescribed function of frequency,” *Journal of Mathematics and Physics*, vol. 10, no. 1-4, pp. 191–236, DOI: [10.1002/sapm1931101191](https://doi.org/10.1002/sapm1931101191).
- [26] R. F. Harrington, *Field Computation by Moment Methods*. Wiley-IEEE Press, 1993, ISBN: 0780310144.
- [27] B. L. G. Jonsson, S. Shi, L. Wang, F. Ferrero, and L. Lizzi, “On Methods to Determine Bounds on the Q -Factor for a Given Directivity,” *IEEE Transactions on Antennas and Propagation*, vol. 65, no. 11, pp. 5686–5696, 2017.

- [28] M. Capek, M. Gustafsson, and K. Schab, "Minimization of Antenna Quality Factor," *IEEE Transactions on Antennas and Propagation*, vol. 65, no. 8, pp. 4115–4123, 2017.
- [29] G. A. E. Vandenbosch, "Reactive Energies, Impedance, and Q Factor of Radiating Structures," *IEEE Transactions on Antennas and Propagation*, vol. 58, no. 4, pp. 1112–1127, 2010.
- [30] A. D. Yaghjian and S. R. Best, "Impedance, bandwidth, and Q of antennas," *IEEE Transactions on Antennas and Propagation*, vol. 53, no. 4, pp. 1298–1324, 2005.
- [31] A. Ludvig-Osipov and B. L. G. Jonsson, "Stored Energies and Q-Factor of Two-Dimensionally Periodic Antenna Arrays," *IEEE Transactions on Antennas and Propagation*, vol. 68, no. 8, pp. 5989–6002, 2020.
- [32] M. Gustafsson and B. L. G. Jonsson, "Antenna Q and Stored Energy Expressed in the Fields, Currents, and Input Impedance," *IEEE Transactions on Antennas and Propagation*, vol. 63, no. 1, pp. 240–249, 2015.
- [33] L. J. Chu, "Physical Limitations of Omni-Directional Antennas," *Journal of Applied Physics*, vol. 19, no. 12, pp. 1163–1175, 1948. DOI: [10.1063/1.1715038](https://doi.org/10.1063/1.1715038). eprint: <https://doi.org/10.1063/1.1715038>. [Online]. Available: <https://doi.org/10.1063/1.1715038>.
- [34] H. L. Thal, "New Radiation Q Limits for Spherical Wire Antennas," *IEEE Transactions on Antennas and Propagation*, vol. 54, no. 10, pp. 2757–2763, 2006.
- [35] M. Gustafsson, D. Tayli, C. Ehrenborg, M. Cismasu, and S. Nordebo, "Antenna Current Optimization using MATLAB and CVX," *Forum for Electromagnetic Research Methods and Application Technologies (FERMAT)*, Apr. 2016.

- [36] M. Gustafsson and S. Nordebo, "Optimal Antenna Currents for Q, Superdirectivity, and Radiation Patterns Using Convex Optimization," *IEEE Transactions on Antennas and Propagation*, vol. 61, no. 3, pp. 1109–1118, 2013.
- [37] S. Boyd and L. Vandenberghe, *Convex Optimization*. Cambridge University Press, 2004. DOI: [10.1017/CB09780511804441](https://doi.org/10.1017/CB09780511804441).
- [38] F. Adelantado, X. Vilajosana, P. Tuset-Peiro, B. Martinez, J. Melia-Segui, and T. Watteyne, "Understanding the Limits of LoRaWAN," *IEEE Communications Magazine*, vol. 55, no. 9, pp. 34–40, 2017.
- [39] A. Andújar, J. Anguera, and C. Puente, "A systematic method to design broadband matching networks," in *Proceedings of the Fourth European Conference on Antennas and Propagation*, 2010, pp. 1–5.
- [40] B. L. G. Jonsson and F. Ferrero, "On Q-factor Bounds for Lossy Embedded Antennas in Electrically Small Devices," in *2019 13th European Conference on Antennas and Propagation (EuCAP)*, 2019, pp. 1–4.
- [41] B. Jonsson, S. Shi, L. Wang, F. Ferrero, and L. Lizzi, "On Methods to Determine Bounds on the Q -Factor for a Given Directivity," *IEEE Transactions on Antennas and Propagation*, vol. 65, no. 11, 5686–5696, 2017, ISSN: 1558-2221. DOI: [10.1109/TAP.2017.2748383](https://doi.org/10.1109/TAP.2017.2748383). [Online]. Available: <http://dx.doi.org/10.1109/TAP.2017.2748383>.
- [42] F. Ferrero, B. L. G. Jonsson, and P. Ratajczak, "Experimental Assessment of Q-factor Bounds for Miniature Embedded Antenna," in *14th European Conference of Antennas and Propagation (EuCAP 2020)*, Copenhagen, Denmark, Mar. 2020, p. 4. [Online]. Available: <https://hal.archives-ouvertes.fr/hal-02431630>.

- [43] K. Rasilainen, R. Luomaniemi, A. Lehtovuori, J. Hannula, and V. Viikari, "Ground Clearance in Smartphone Antennas," in *2019 13th European Conference on Antennas and Propagation (EuCAP)*, 2019, pp. 1–5.
- [44] J. Villanen, J. Ollikainen, O. Kivekas, and P. Vainikainen, "Coupling element based mobile terminal antenna structures," *IEEE Transactions on Antennas and Propagation*, vol. 54, no. 7, pp. 2142–2153, 2006.
- [45] R. Tang and Z. Du, "Wideband Monopole Without Lumped Elements for Octa-Band Narrow-Frame LTE Smartphone," *IEEE Antennas and Wireless Propagation Letters*, vol. 16, pp. 720–723, 2017.
- [46] D. Huang, Z. Du, and Y. Wang, "A Quad-Antenna System for 4G/5G/GPS Metal Frame Mobile Phones," *IEEE Antennas and Wireless Propagation Letters*, vol. 18, no. 8, pp. 1586–1590, 2019.
- [47] Q. Chen, H. Lin, J. Wang, L. Ge, Y. Li, T. Pei, and C. Sim, "Single Ring Slot-Based Antennas for Metal-Rimmed 4G/5G Smartphones," *IEEE Transactions on Antennas and Propagation*, vol. 67, no. 3, pp. 1476–1487, 2019.
- [48] R. S. Aziz, A. K. Arya, and S. Park, "Multiband Full-Metal-Rimmed Antenna Design for Smartphones," *IEEE Antennas and Wireless Propagation Letters*, vol. 15, pp. 1987–1990, 2016.
- [49] J. Lu, S. Syu, and Y. Zhang, "A Band Reconfigurable Antenna for a Mobile Phone with the Metal Cover," in *2018 International Symposium on Antennas and Propagation (ISAP)*, 2018, pp. 1–2.
- [50] F. A. Asadallah, J. Costantine, and Y. Tawk, "A Multiband Compact Reconfigurable PIFA Based on Nested Slots," *IEEE Antennas and Wireless Propagation Letters*, vol. 17, no. 2, pp. 331–334, 2018.

- [51] J. Hannula, T. Saarinen, J. Holopainen, and V. Viikari, "Frequency Reconfigurable Multiband Handset Antenna Based on a Multichannel Transceiver," *IEEE Transactions on Antennas and Propagation*, vol. 65, no. 9, pp. 4452–4460, 2017.
- [52] M. Gustafsson and S. Nordebo, "Bandwidth, Q Factor, and Resonance Models of Antennas," *Progress in Electromagnetics Research-pier - PROG ELECTROMAGN RES*, vol. 62, pp. 1–20, Jan. 2006. DOI: [10.2528/PIER06033003](https://doi.org/10.2528/PIER06033003).
- [53] R. Fano, "Theoretical limitations on the broadband matching of arbitrary impedances," *Journal of the Franklin Institute*, vol. 249, no. 1, pp. 57–83, 1950, ISSN: 0016-0032. DOI: [https://doi.org/10.1016/0016-0032\(50\)90006-8](https://doi.org/10.1016/0016-0032(50)90006-8). [Online]. Available: <http://www.sciencedirect.com/science/article/pii/0016003250900068>.
- [54] F. Bergh, "An Analysis of Particle Swarm Optimizers," Jan. 2002.
- [55] Y. Zhang, S. Wang, and G. Ji, "A Comprehensive Survey on Particle Swarm Optimization Algorithm and Its Applications," *Mathematical Problems in Engineering*, vol. 2015, pp. 1–38, 2015.
- [56] D. Gies and Y. Rahmat-Samii, "Particle swarm optimization for reconfigurable phase-differentiated array design," *Microwave and Optical Technology Letters*, vol. 38, no. 3, pp. 168–175, 2003. DOI: [10.1002/mop.11005](https://doi.org/10.1002/mop.11005). eprint: <https://onlinelibrary.wiley.com/doi/pdf/10.1002/mop.11005>. [Online]. Available: <https://onlinelibrary.wiley.com/doi/abs/10.1002/mop.11005>.
- [57] R. L. Haupt, "Thinned arrays using genetic algorithms," *IEEE Transactions on Antennas and Propagation*, vol. 42, no. 7, pp. 993–999, 1994.
- [58] I. Santamaria, L. Lizzi, F. Ferrero, and R. Staraj, "An Optimization Driven Method for the Synthesis of Reconfigurable Parasitic Antenna

- Arrays," in *2020 IEEE International Symposium on Antennas and Propagation and North American Radio Science Meeting*, IEEE, Montreal, Canada, Jul. 2020, pp. 1–2. [Online]. Available: <https://hal.archives-ouvertes.fr/hal-02515636>.
- [59] L. Lizzi, F. Viani, R. Azaro, and A. Massa, "A PSO-Driven Spline-Based Shaping Approach for Ultrawideband (UWB) Antenna Synthesis," *IEEE Transactions on Antennas and Propagation*, vol. 56, no. 8, pp. 2613–2621, 2008.
- [60] N. Jin and Y. Rahmat-Samii, "Parallel particle swarm optimization and finite-difference time-domain (PSO/FDTD) algorithm for multi-band and wide-band patch antenna designs," *IEEE Transactions on Antennas and Propagation*, vol. 53, no. 11, pp. 3459–3468, 2005.
- [61] OptenniLab, *Optenni Lab website*. [Online]. Available: <https://www.optenni.com/>.
- [62] B. L. Dhevi, K. S. Vishvaksenan, and K. Rajakani, "Isolation Enhancement in Dual-Band Microstrip Antenna Array Using Asymmetric Loop Resonator," *IEEE Antennas and Wireless Propagation Letters*, vol. 17, no. 2, pp. 238–241, 2018.
- [63] Z. Niu, H. Zhang, Q. Chen, and T. Zhong, "Isolation Enhancement in Closely Coupled Dual-Band MIMO Patch Antennas," *IEEE Antennas and Wireless Propagation Letters*, vol. 18, no. 8, pp. 1686–1690, 2019.
- [64] J. Hwang and S. Chung, "Isolation Enhancement Between Two Packed Antennas With Coupling Element," *IEEE Antennas and Wireless Propagation Letters*, vol. 10, pp. 1263–1266, 2011.
- [65] Y. Wang and Z. Du, "Wideband Monopole Antenna With Less Non-ground Portion For Octa-Band WWAN/LTE Mobile Phones," *IEEE Transactions on Antennas and Propagation*, vol. 64, no. 1, pp. 383–388, 2016.

- [66] H. Xu, H. Wang, S. Gao, H. Zhou, Y. Huang, Q. Xu, and Y. Cheng, "A Compact and Low-Profile Loop Antenna With Six Resonant Modes for LTE Smartphone," *IEEE Transactions on Antennas and Propagation*, vol. 64, no. 9, pp. 3743–3751, 2016.
- [67] J. Ilvonen, R. Valkonen, J. Holopainen, and V. Viikari, "Design Strategy for 4G Handset Antennas and a Multiband Hybrid Antenna," *IEEE Transactions on Antennas and Propagation*, vol. 62, no. 4, pp. 1918–1927, 2014.
- [68] K. Rasilainen, A. Lehtovuori, and V. Viikari, "LTE handset antenna with closely-located radiators, low-band MIMO, and high efficiency," in *2017 11th European Conference on Antennas and Propagation (EUCAP)*, 2017, pp. 3074–3078.
- [69] Y. P. Zhang and D. Liu, "Antenna-on-Chip and Antenna-in-Package Solutions to Highly Integrated Millimeter-Wave Devices for Wireless Communications," *IEEE Transactions on Antennas and Propagation*, vol. 57, no. 10, pp. 2830–2841, 2009.
- [70] L. Zhu, J. Zhang, Z. Xiao, X. Cao, D. O. Wu, and X. Xia, "Millimeter-Wave NOMA With User Grouping, Power Allocation and Hybrid Beamforming," *IEEE Transactions on Wireless Communications*, vol. 18, no. 11, pp. 5065–5079, 2019.
- [71] S. Han, C. I. Z. Xu, and S. Wang, "Reference Signals Design for Hybrid Analog and Digital Beamforming," *IEEE Communications Letters*, vol. 18, no. 7, pp. 1191–1193, 2014.
- [72] *PCB Design Guidelines*, 2020. [Online]. Available: <https://www.eurocircuits.com/pcb-design-guidelines/>.

- [73] IBM and Ericsson, *IBM and Ericsson Announce 5G mmWave Phased Array Antenna Module*, 2017 (accessed August 20, 2020). [Online]. Available: <https://www.microwavejournal.com/articles/27830-ibm-and-ericsson-announce-5g-mmwave-phase-array-antenna-module>.
- [74] Anokiwave, *Anokiwave-0129*, accessed January, 2020. [Online]. Available: https://www.anokiwave.com/company/company-news/releases/awmf_0129.html.
- [75] Keysight, *Keysight 28 GHz 5G-band phased array link*, accessed January, 2020. [Online]. Available: <https://about.keysight.com/en/newsroom/images/5G28GHz/Keysight-ucsd-28-GHz-5G-band-phased-array-link-high.jpg>.
- [76] R. Zhang, X. Sun, J. Fernández-González, and M. Sierra-Pérez, "Planar antenna array on LTCC and rogers substrates for 5G applications," in *2017 International Symposium on Antennas and Propagation (ISAP)*, 2017, pp. 1–2.
- [77] J. Helander, K. Zhao, Z. Ying, and D. Sjöberg, "Performance Analysis of Millimeter-Wave Phased Array Antennas in Cellular Handsets," *IEEE Antennas and Wireless Propagation Letters*, vol. 15, pp. 504–507, 2016.
- [78] S. Wi, Y. Lee, and J. Yook, "Wideband Microstrip Patch Antenna With U-Shaped Parasitic Elements," *IEEE Transactions on Antennas and Propagation*, vol. 55, no. 4, pp. 1196–1199, 2007.
- [79] S. Asif, A. Iftikhar, M. N. Rafiq, B. D. Braaten, M. S. Khan, D. E. Anagnostou, and T. S. Teeslink, "A compact multiband microstrip patch antenna with U-shaped parasitic elements," in *2015 IEEE International Symposium on Antennas and Propagation USNC/URSI National Radio Science Meeting*, 2015, pp. 617–618.

- [80] A. A. Serra, P. Nepa, G. Manara, G. Tribellini, and S. Cioci, "A Wide-Band Dual-Polarized Stacked Patch Antenna," *IEEE Antennas and Wireless Propagation Letters*, vol. 6, pp. 141–143, 2007.
- [81] D. Yang, H. Zeng, Y. Wen, and M. Chen, "Analysis of dual-polarized stacked patch antenna based on theory of characteristic modes," in *2016 IEEE 5th Asia-Pacific Conference on Antennas and Propagation (APCAP)*, 2016, pp. 269–270.
- [82] A. Foudazi, M. T. Ghasr, and K. M. Donnell, "Mutual coupling in aperture-coupled patch antennas fed by orthogonal SIW line," in *2016 IEEE International Symposium on Antennas and Propagation (APSURSI)*, 2016, pp. 1587–1588.
- [83] Y. Wu, C. Wu, D. Lai, and F. Chen, "A Reconfigurable Quadri-Polarization Diversity Aperture-Coupled Patch Antenna," *IEEE Transactions on Antennas and Propagation*, vol. 55, no. 3, pp. 1009–1012, 2007.
- [84] C. A. Balanis, "Aperture antenna," in *Antenna Theory: Analysis and Design*. John Wiley Sons, Ltd, February 2016, pp. 639–709, ISBN: 978-1-118-64206-1. [Online]. Available: <https://www.wiley.com/en-us/Antenna+Theory+%3A+Analysis+and+Design+%2C+4th+Edition-p-9781118642061>.
- [85] D. M. Pozar, "Microstrip antenna aperture-coupled to a microstrip line," *Electronics Letters*, vol. 21, no. 2, pp. 49–50, 1985.
- [86] mmMagic, *mmMAGIC project*. [Online]. Available: <https://5g-mmmagic.eu/>.
- [87] C. Sabatier, P. Brachat, A. Calderone, E. Seguenot, and F. Devillers, "Compact linear array at 810 MHz," in *IEEE Antennas and Propagation Society International Symposium 1997. Digest*, vol. 4, 1997, 2119–2122 vol.4.

- [88] Qualcomm, *Mobilizing 5G NR Millimeter Wave: Network Coverage Simulation Studies for Global Cities*, 5775 Morehouse Drive San Diego, CA 92121, U.S.A., 2017.
- [89] S. Mondal, R. Singh, A. I. Hussein, and J. Paramesh, "A 25-30 GHz 8-antenna 2-stream hybrid beamforming receiver for MIMO communication," in *2017 IEEE Radio Frequency Integrated Circuits Symposium (RFIC)*, 2017, pp. 112–115.
- [90] J. Chen, "Hybrid Beamforming With Discrete Phase Shifters for Millimeter-Wave Massive MIMO Systems," *IEEE Transactions on Vehicular Technology*, vol. 66, no. 8, pp. 7604–7608, 2017.
- [91] F. Ferrero, Y. Benoit, L. Brochier, J.-Y. Dauvignac, C. Migliaccio, and S. Gregson, "Spherical Scanning Measurement Challenge for Future Millimeter Wave Applications," in *AMTA Conference*, ser. AMTA Conference (Antenna Measurement Techniques Association), Long Beach, United States, Oct. 2015. [Online]. Available: <https://hal.archives-ouvertes.fr/hal-01256554>.
- [92] J. Helander, D. Sjöberg, M. Gustafsson, K. Zhao, and Z. Ying, "Characterization of millimeter wave phased array antennas in mobile terminal for 5G mobile system," in *2015 IEEE International Symposium on Antennas and Propagation USNC/URSI National Radio Science Meeting*, 2015, pp. 7–8.
- [93] K. R. Mahmoud and A. M. Montaser, "Performance of Tri-Band Multi-Polarized Array Antenna for 5G Mobile Base Station Adopting Polarization and Directivity Control," *IEEE Access*, vol. 6, pp. 8682–8694, 2018.
- [94] Y. Huo, X. Dong, and W. Xu, "5G Cellular User Equipment: From Theory to Practical Hardware Design," *IEEE Access*, vol. 5, pp. 13 992–14 010, 2017.

- [95] I. Syrytsin, S. Zhang, and G. F. Pedersen, "User Impact on Phased and Switch Diversity Arrays in 5G Mobile Terminals," *IEEE Access*, vol. 6, pp. 1616–1623, 2018.
- [96] I. Syrytsin, S. Zhang, G. F. Pedersen, and Z. Ying, "User Effects on the Circular Polarization of 5G Mobile Terminal Antennas," *IEEE Transactions on Antennas and Propagation*, vol. 66, no. 9, pp. 4906–4911, 2018.
- [97] I. Syrytsin, S. Zhang, and G. F. Pedersen, "Effects of Phone Case and User Effects on Switched-Beam High Gain Antenna System for 5G Mobile Terminals," in *2018 International Conference on Electromagnetics in Advanced Applications (ICEAA)*, 2018, pp. 110–113.
- [98] B. Xu, Z. Ying, L. Scialacqua, A. Scannavini, L. J. Foged, T. Bolin, K. Zhao, S. He, and M. Gustafsson, "Radiation Performance Analysis of 28 GHz Antennas Integrated in 5G Mobile Terminal Housing," *IEEE Access*, vol. 6, pp. 48 088–48 101, 2018.
- [99] C. A. Balanis, "Fundamental Parameters and Definitions for Antennas," in *Modern Antenna Handbook*. John Wiley Sons, Ltd, 2007, ch. 1, pp. 1–56, ISBN: 9780470294154. DOI: [10.1002/9780470294154.ch1](https://doi.org/10.1002/9780470294154.ch1). eprint: <https://onlinelibrary.wiley.com/doi/pdf/10.1002/9780470294154.ch1>. [Online]. Available: <https://onlinelibrary.wiley.com/doi/abs/10.1002/9780470294154.ch1>.
- [100] B. Yu, K. Yang, C. Sim, and G. Yang, "A Novel 28 GHz Beam Steering Array for 5G Mobile Device With Metallic Casing Application," *IEEE Transactions on Antennas and Propagation*, vol. 66, no. 1, pp. 462–466, 2018.
- [101] M. Heino, C. Icheln, and K. Haneda, "Finger effect on 60 GHz user device antennas," in *2016 10th European Conference on Antennas and Propagation (EuCAP)*, 2016, pp. 1–5.

- [102] K. Zhao, S. Zhang, Z. Ho, O. Zander, T. Bolin, Z. Ying, and G. F. Pedersen, "Spherical Coverage Characterization of 5G Millimeter Wave User Equipment With 3GPP Specifications," *IEEE Access*, vol. 7, pp. 4442–4452, 2019.
- [103] —, "Spherical Coverage Characterization of 5G Millimeter Wave User Equipment With 3GPP Specifications," *IEEE Access*, vol. 7, pp. 4442–4452, 2019.
- [104] RohdeSchwarz, *5G NR –OTA test measurement aspects standards regulations*. [Online]. Available: <https://www.rohde-schwarz.com>.
- [105] T. Wu, T. S. Rappaport, and C. M. Collins, "The human body and millimeter-wave wireless communication systems: Interactions and implications," in *2015 IEEE International Conference on Communications (ICC)*, 2015, pp. 2423–2429.
- [106] S Gabriel, R. W. Lau, and C Gabriel, "The dielectric properties of biological tissues: III. Parametric models for the dielectric spectrum of tissues," *Physics in Medicine and Biology*, vol. 41, no. 11, pp. 2271–2293, 1996. DOI: [10.1088/0031-9155/41/11/003](https://doi.org/10.1088/0031-9155/41/11/003). [Online]. Available: <https://doi.org/10.1088/0031-9155/41/11/003>.
- [107] C. Buey, F. Ferrero, L. Lizzi, and P. Ratajczak, "Measurement set-up for the assessment of user impact on handheld terminal beyond 10 GHz," in *2017 IEEE Conference on Antenna Measurements Applications (CAMA)*, 2017, pp. 327–329.
- [108] C. Buey, F. Ferrero, L. Lizzi, P. Ratajczak, Y. Benoit, and L. Brochier, "Investigation of hand effect on a handheld terminal at 11 GHz," in *2016 10th European Conference on Antennas and Propagation (EuCAP)*, 2016, pp. 1–5.
- [109] Corning, *Corning Gorilla Glass 6*, Product Information Sheet, Apr. 2018 (rev. C).

- [110] OOKLA, *5G roll-out map in Europe*. [Online]. Available: <https://www.speedtest.net/ookla-5g-map>.